九州大学学術情報リポジトリ
Kyushu University Institutional Repository

Development of high performance MgB2 superconducting wires

葉, 術軍

https://doi.org/10.15017/1441201

出版情報：九州大学, 2013, 博士（工学）, 課程博士
バージョン：
権利関係：全文ファイル公表済

KYUSHU UNIVERSITY

博 士 論 文

Development of high performance MgB_2 superconducting wires
(高性能MgB_2超伝導線材に関する研究)

平成 26 年 1 月

九州大学工学府

YE SHUJUN

Acknowledgement

Firstly, I would like to thank my supervisor Prof. Takahito OHMURA for his warmhearted support and invaluable guidance. I learned a lot from him. I also want to thank Prof. Tsukasa KIYOSHI, who accepted me as his Ph.D student and gave me invaluable guidance. Unfortunately, he left us forever in January 2013. I think not only me, but also many people remember him because he was so nice a person.

Specially, I would like to thank Prof. Hiroaki KUMAKURA, who kindly gave me the chance to study in National Institute for Material Science (NIMS). I greatly appreciated the chance because it changed my life. In the past years, he always helped me, he gave me the direct guidance, and he allowed me to discuss with him almost any time even he is quite busy.

I want to give my deeply thanks to Prof. Kazumasa TOGANO. He is so kind. He not only taught me many details in the experiment, but also gave me much important help in my study and life.

I would like to thank Dr. Akiyoshi MATSUMOTO. He helped me many times in my experiment, which is very important for my study. I greatly appreciate Dr. Minghui SONG. He also gave me important help in the microstructural analysis.

I received too many kind help for my study and life from the people in the superconducting wire unit, NIMS. I would like to thank them here: Prof. Hitoshi KITAGUCHI, Prof. Yoshihiko TAKANO, Dr. Takao TAKEUCHI, Dr. Tsuneo KURODA, Dr. Toshihisa ASANO, Dr. Hiroki FUJII, Dr. Gen NISHIJIMA, Dr. Yoshinori TSUCHIYA, Dr. Takashi MOCHIKU, Dr. Takayuki NAKANE, Dr. Akihiro KIKUCHI, Dr. Nobuya BANNO, Dr. Shinji MATSUMOTO, Dr. Zhiyu ZHANG, Dr. Hiroyuki TAKEYA, Dr. Takahide YAMAGUCHI, Dr. Masaya FUJIOKA, Mr. Hiroyuki TAKIGAWA, Ms. Yunchao ZHANG, and all other members.

Prof. Hiroaki NAKANO, Prof. Takanobu KISS, Associate Prof. Ryo TERANISHI of Kyushu University gave the invaluable suggestion and comments to my study, especially to my Ph.D thesis. I deeply appreciate them.

I would like to thank Ms. Naomi TERASHIMA, Ms. Yukiko SUKEGAWA, Ms. Yukari OGASAWARA, Ms. Akiko SOMEYA, and Ms. Yoko UCHIDA in NIMS and Ms. Reiko INOUE in Kyushu University for their kind help in office affaires.

NIMS and Kyushu University support me by Kyushu-NIMS Graduate Program. I appreciate the financial support from this program during my Ph.D course. I thank all the professors, researchers, and staff in graduate program section of NIMS and Faculty of Engineering of Kyushu University. There are also many people in NIMS and Kyushu University who gave me direct and indirect help in my study or my life, I really appreciated them.

I thank all the staff of Strength Design Group and Tsukuba Magnet Laboratory in NIMS. I also thank Dr. Masaki TAKEGUCHI, Ms. Yuki NISHIMIYA, Ms. Noriko ISAKA, Ms. Kanako NAKAYASHIKI and all other staff of Transmission Electron Microscopy station in NIMS. I appreciated Prof. Kozo OSAMURA of Research institute for applied sciences, Dr. Yoshitaka MATSUSHITA of NIMS, Dr. Syutaro MACHIYA of Daido University, Dr. Takahisa SHOBU and Dr. Shuoyuan ZHANG of Japan atomic energy agency (JAEA) helped me too much for the experiments in Spring-8. I also appreciated for all the people related with following experiments in Spring-8: proposal No. 2013B1573, 2012B1435, 2013A3789 and 2013B3782 of Japan Synchrotron Radiation Research Institute (JASRI), and proposal No. 2013A-E22 2013B-E20 of JAEA.

I appreciate Advanced Low Carbon Technology Research and Development Program (ALCA) of Japan Science and Technology Agency (JST) for the fund support. I also appreciated associate Prof. Kohei HIGASHIKAWA in KISS lab of Kyushu University and all other collaborators and staff of ALCA.

I thank all the people, who cared/cares me, and who I cared/care.

Finally, I want to thank my family: my father, mother, elder sister, young sister, especially my wife Zhuang ZhOU; you are my all!

Abstract

MgB_2 is expected to be used in no-helium conditions to replace metallic superconductors that are operating in a liquid helium environment. Low cost is the most important advantage of MgB_2 to be used as a practical superconducting wire. Currently, there have already been products using MgB_2 superconductor, but the cost per unit length and unit superconducting current density of these products are not so low because the critical current properties of these MgB_2 wires are not high enough to operate in the expected condition. The expected condition for MgB_2 wire operation is at ~20 K using a cryocooler or liquid hydrogen. The main work of this thesis is to enhance the critical current properties for MgB_2 wires at 20 K and 5 T.

Internal-Mg-diffusion (IMD) process produces higher density MgB_2 layer than that of Powder-in-tube (PIT) process, thus IMD MgB_2 wires have higher critical current properties. However, un-reacted B particles were observed in the MgB_2 layer of IMD-processed wires fabricated with low quality B powder (325-mesh, 99%). In chapter 2, I found that some Mg powder addition is effective to decrease the un-reacted B particles and enhance the critical current density (J_c) values. On the other hand, Mg powder addition also formed voids in MgB_2 layer and these voids decreased the J_c values. If the amount of Mg powder in the B layer is increased, the Mg rod diameter should be decreased simultaneously in order to maintain a Mg:B ratio of 1:2, corresponding to stoichiometric MgB_2. Consequently I developed a new hybrid method for fabricating MgB_2 wires by a combination of IMD and PIT processes. The MgB_2 layer thickness is larger and the diameter of the central hole is smaller than those of a conventional IMD processed wire, thus MgB_2 area fraction is higher. The proposed method also achieves a much higher MgB_2 layer density, and thus a much higher J_c, than those obtained by the PIT method. The combination of these factors leads to the enhanced engineering critical current density (J_e) value. The new method introduced in chapter 2 is developed for the low quality B powder, but it is also effective for nano-sized B high quality powders used in chapter 5 and in chapter 6 because it could be effectively used to decrease the B-rich region caused by these nano-sized powders.

The multi-filamentary superconducting wires are important for practical applications. In chapter 3, we succeeded in fabricating IMD-processed 37-filamentary MgB_2 wires. SiC-added 37-filamentary MgB_2 wires show the highest J_c value (7.6×10^4 A/cm^2 at 4.2 K and 10 T) among all of the IMD-processed MgB_2 wires fabricated under the same conditions (mono-filamentary and 7-filamentary). The short Mg diffusion distance of 37-filamentary IMD-processed MgB_2 wires decreases un-reacted B particles. This is the main factor to raise the J_c values. The successful fabrication of 37-filamentay wires indicates that the IMD process can be used to fabricate MgB_2 wires for large-scale applications.

It was reported that the co-addition of SiC and ethyltoluene is effective in the PIT-processed MgB_2 wires. Accordingly, it may be also effective in the IMD-processed MgB_2 wires. In chapter 4, I

have carried out the SiC and ethyltoluene, toluene, or dimethylbenzene co-addition to IMD-processed MgB_2 wires. The J_c properties are enhanced by the toluene and dimethylbenzene, but not so good for ethyltoluene.

The researchers in Ohio State University and Hyper Tech Company used a special plasma-synthesized 2% carbon-coated B powder (Special Materials Inc., SMI powder) to fabricate thin IMD-processed MgB_2 wires (diameter: 0.55 mm). They obtained high J_c and J_e for different samples. The small diameter of the wire is considered to decrease the Mg diffusion distance, which leads to an improved reaction between Mg and B, thus a high J_c is obtained. I also tried this B powder, however, I could not obtain good results as theirs. After investigating the B powder, I found that many BCl_3 (source material for this B powder) exists in the B powder. Since dimethylbenzene dissolve BCl_3, and our experiments in chapter 2 also showed dimethylbenzene enhanced the J_c of IMD-processed MgB_2 wires, I used the dimethylbenzene to remove BCl_3 from the B powder. The dimethylbenzene decreased the BCl_3 in B powder and then I obtained J_c values higher than Ohio state university in chapter 5. For both Ta- and Fe-sheathed wires, the highest J_c value was about 1.2×10^5 A/cm^2 at 4.2 K and 10 T, and the J_e value was about 1×10^4 A/cm^2. Furthermore, the Fe-sheathed wire exhibited a J_c of 7.6×10^4 A/cm^2 and a J_e of 5.3×10^3 A/cm^2 at 20 K and 5 T, which are the highest values reported for MgB_2 wires to date.

The carbon-coated nano-sized B powder is responsible to obtain the high J_c and J_e for IMD-processed MgB_2 wires. However, the C-coating process using plasma method is not easy, thus it is expensive. Furthermore, this B powder is unstable because BCl_3 exists. Therefore, I tried a new B powder added with an aromatic hydrocarbon (coronene, $C_{24}H_{12}$) as a carbon source, which is described in chapter 6. The similar level of high J_c and J_e values to the carbon-coated B powders in chapter 5 were obtained. The J_c properties are expected to be further enhanced by optimizing the coronene-coating and heat treatment conditions. It is easy to obtain this coronene-coated B powder and the powder is stable. And the amount of carbon addition is also easily controlled. Using the new B powder with $C_{24}H_{12}$ coating we can expect to fabricate high performance MgB_2 wires for large-scale practical applications with low cost.

Figure captions

Chapter 1

Fig. 1-1 Brief history of discovery of superconductors 3

Fig. 1-2 The properties of a superconducting material 4

Fig. 1-3 Crystal structure of MgB_2 7

Fig. 1-4 Fabrication of MgB_2 wires with PIT process 8

Fig. 1-5 Fabrication of MgB_2 wires by IMD process 9

Fig. 1-6 Typical optical microscopy of cross sectional images of IMD-processed MgB_2 wire with diameter of 1.2 mm by optical microscopy, (a) transverse and (b) longitudinal cross section before heat treatment, (c) transverse and (d) longitudinal cross section after heat treatment 10

Fig. 1-7 The uniformity in longitudinal direction of the several IMD-processed MgB_2 wires 11

Fig. 1-8 Typical SEM image of MgB_2 wires (a) IMD processed MgB_2 wires, (b) PIT processed MgB_2 wires 11

Chapter 2

Fig. 2-1 Schematic maps of the transverse cross sections for MgB_2 wires fabricated with (a) IMD, (b) PIT, and (c) a new method combining IMD and PIT 20

Fig. 2-2 (a) J_c-B curves and (b) J_e-B curves of IMD undoped and Mg-added MgB_2 wires 23

Fig. 2-3 Magnified optical microscope images of transverse cross-section of IMD-processed (a) undoped and (b) 6 mol% Mg-added MgB_2 wires 24

Fig. 2-4 SEM images of longitudinal cross-section of IMD-processed (a) undoped and (b) 6 mol% Mg-added MgB_2 wires 25

Fig. 2-5 (a) STEM dark field (DF) image of the reacted layer in undoped MgB_2 wire. (b) Magnified STEM-DF image of the red frame in Fig 4(a). (c) High resolution image of region (A) in Fig 4(b). (d) High resolution image of region (B) in Fig 4(b) 26

Fig. 2-6 STEM-DF image of 6 mol% Mg-added IMD-processed MgB_2 wires 27

Fig. 2-7 J_c value at 4.2 K and 10 T as a function of Mg concentration of IMD MgB_2 wires 27

Fig. 2-8 (a) J_c-B and (b) J_e-B curves of the IMD-processed MgB_2 wires with 10 mol% SiC addition and 10 mol% SiC and Mg powder (3, 6, and 9 mol%) co-addition …… 28

Fig. 2-9 STEM-DF images of (a) 10 mol% SiC-added (b) 10 mol% SiC and 6 mol% Mg powder co-added IMD-processed MgB_2 wires …… 29

Fig. 2-10 OM images on the transverse cross sections of (a) IMD-processed wire (M0), (b) PIT-processed wire (P0), and (c) the wire fabricated with new method combining IMD and PIT (M2)(Specification of the samples M0 to P0 are listed in table 2-2) …… 31

Fig. 2-11 SEM images of the (a) transverse and (b) longitudinal cross sections of the M2 MgB_2 wires (Specification of the samples M0 to P0 are listed in table 2-2) …… 32

Fig. 2-12 SEM images of the longitudinal cross sections of the MgB_2 wires, (a) M0, (b) M1, (c) M2, (d) M3, and (e) P0. All images were obtained after heat treatment (Specification of the samples M0 to P0 are listed in table 2-2) …… 33

Fig. 2-13 (a) J_c–B and (b) J_e–B curves at 4.2 K for the MgB_2 wires fabricated in this study (Specification of the samples M0 to P0 are listed in table 2-2) …… 34

Fig. 2-14 J_c and J_e values at 4.2 K and 10 T as a function of added Mg concentration, i.e. IMD, M1-M3, PIT (Specification of the samples M0 to P0 are listed in table 2-2) …… 35

Chapter 3

Fig. 3-1 Fabrication process of 37-filamentary IMD-processed MgB_2 wires …… 39

Fig. 3-2 Heat treatment processes for IMD-processed 37-filament MgB_2 wires …… 39

Fig. 3-3 (a) SEM images of IMD-processed 37-filament MgB_2 wires and its filaments, and (b) the elements mapping for one filament of (a) …… 41

Fig. 3-4 (a) J_e values at 4.2 K and 10 T, and (b) J_c-B curves at 4.2 K for several heat treatment conditions of the IMD-processed 37-filament MgB_2 wires …… 42

Fig. 3-5 J_c-B curves of the IMD-processed MgB_2 wires with different filaments at 4.2 K …… 44

Fig. 3-6 SEM images in transverse cross-section of Ta-mono (a) near Ta sheath and (b) near hole (spectrum are observed for spots 1, 2 and 3), (c) Ta-37 filament 1, and (d) Ta-37 filament 2 …… .45

Fig. 3-7 Temperature dependence of the J_c-B curve for (a) SiC-added, (b) both undoped and SiC-added IMD-processed 37-filament MgB_2 wires, and (c) temperature dependence of I_c on the

temperature (higher than 30 K) at the self-field for both undoped and SiC-added IMD-processed 37-filament MgB_2 wires 48

Chapter 4

Fig. 4-1 J_e–B curves (at 4.2 K) of various IMD-processed MgB_2 wires heat treated at (a) 640℃, (b) 670℃ and (c) 700℃ for 3 hours, and (d) J_c–B curves (at 4.2 K) of various IMD processed MgB_2 wires: optimized heat treatment temperature was chosen for each wire 54

Fig. 4-2 (a) the J_c–B curves and (b) the J_e–B curves of SiC+dimethylbenzene co-added IMD-processed MgB_2 wires, respectively. (c) the J_c–B curves of pure IMD-processed MgB_2 wires 56

Fig. 4-3 J_c -B curves of IMD-processed MgB_2 wires with different additives 57

Fig. 4-4 XRD patterns of IMD-processed MgB_2 wires with different additives 58

Fig. 4-5 SEM images of IMD-processed MgB_2 wires (a) with no addition, (b) with toluene-addition , (c) with SiC-addition, (d) with both SiC and toluene co-addition 59

Fig. 4-6 Representative SEM image(a), EDX element mapping images of B, O, Mg, Si and C elements (b - f), on the longitudinal cross sections of SiC-added IMD-processed MgB_2 wires 60

Fig. 4-7 (a) TEM image of IMD-processed mono-core MgB_2 wires with SiC addition, (b) high resolution image of region B in (a), (c) diffraction pattern of (b), (d) high resolution image of region C in (a), (e) diffraction pattern of (d) 61

Fig. 4-8 Elemental maps by EDS and EFI of (a) pure wires and (b) SiC-added wires; the schematic illustrations of the elemental distributions of (c) pure wires and (d) SiC-added wires 63

Chapter 5

Fig. 5-1 The pretreating process for SMI B powder by dimethylbenzene 67

Fig. 5-2 XRD pattern of IMD-processed MgB_2 wires (before heat treatment) fabricated with SMI powder (left), and the images of IMD-processed MgB_2 wires fabricated with SMI and SMI+D powders (right) 68

Fig. 5-3 EDX spectra of (a) SMI powder, and (b) SMI+D powder 69

Fig. 5-4 SEM images of (a) SMI powder, and (b) SMI+D powder 70

Fig. 5-5 Cross-sectional SEM images of (a), (b) Ta-SMI+D wire, and (c), (d) Fe-SMI+D-1wire, (e-f) optical microscope images of (c-d) 71

Fig. 5-6 X-ray diffraction (XRD) patterns for the Fe-SMI and Fe-SMI+D-1 wires 72

Fig. 5-7 Comparison of (a) J_c-B, and (b) J_e-B curves for IMD-processed MgB_2 wires at 4.2 K 74

Fig. 5-8 (a) J_c-B curves and (b) Je-B curves for IMD-processed MgB2 wire (Fe-SMI+D-1) at different temperatures. Previously reported data for Ta-sheathed wire fabricated using SiC addition [7, 8], and J_c data for Nb-Ti wires [12] are shown using dotted lines 76

Fig. 5-9 SEM images of Fe-SMI wire at magnification of (a) 30k, and (b) 80k times, and (c) EDX maps corresponding to the area shown in (a). SEM images of Fe-SMI+D-1 wire at magnification of (d) 30k and (e) 80k times. SEM images of Ta-SMI+D wire at magnification of (f) 30k and (g) 50k times ... 78

Fig. 5-10 (a) STEM dark-field image of Ta-SMI+D wire at 25k times magnification and camera length of 20 cm, (b) STEM dark-field image of region R1 in (a) at 250k times magnification and camera length of 20 cm, (c) STEM bright-field image of region R2 in (a) at 300k times magnification and camera length of 80 cm, (d) STEM dark-field image of region R2 in (a) at 300k times magnification and camera length of 80 cm, (e) high resolution images (800k) and corresponding fast Fourier transforms (FFT) of regions A to E in (c) and (d), and (f) electron energy loss spectroscopy (EELS) images of region R3 in (a) 81

Chapter 6

Fig. 6-1 Molecule structure of coronene ($C_{24}H_{12}$) 85

Fig. 6-2 Transverse cross sectional image observed by optical microscope (a), and longitudinal cross sectional image observed by SEM (b) of PIT-processed MgB_2 wires (diameter: 1.0 mm) ... 86

Fig. 6-3 (a) J_c-B curves, and (b) J_e-B curves of PIT-processed MgB_2 wires at 4.2 K 87

Fig. 6-4 X-ray diffraction patterns of PIT-processed MgB_2 wires 88

Fig. 6-5 SEM images of (a) undoped, (b) 2%, (c) 5%, and (d) 10% coronene-added PIT-processed MgB_2 wires 89

Fig. 6-6 Optical microscope image on the transverse cross section of the IMD-processed MgB_2 wires (diameter: 0.6 mm) 90

Fig. 6-7 (a) J_c-B curves, and (b) J_e-B curves of IMD-processed MgB_2 wires 91

Fig. 6-8 The J_c values at high magnetic fields of undoped and coronene-added MgB_2 wires fabricated with both IMD and PIT processes …… 92

Chapter 7

Fig. 7-1 Photograph (left) and schematic illustration (right) of apparatus to measure I_c versus uniaxial tension…… 98

Fig. 7-2 I_c as a function of uniaxial strain, inset shows I_c/I_{c0} as a function of uniaxial strain (both IMD and PIT are fabricated with 325-mesh B with 10 mol% SiC addition as the method introduced in chapter 4) …… 99

Fig. 7-3 schematic illustration (left) and photo (right) of apparatus to measure I_c versus transverse compression …… 100

Fig. 7-4 Normalized I_c as a function of transverse compressive stress …… 100

Fig. 7-5 (a) The diffractometer and (b) experiment layout …… 101

Fig. 7-6 The relations of a load strain and the lattice strain …… 101

Fig. 7-7 (a) Experimental equipment, (b) magnified image, and (c) wire furnace …… 102

Fig. 7-8 (a) 2-D data of XRD diffraction, and (b) 1-D data of XRD calculated from (a) …… 103

Table captions

Chapter 1

Table 1-1 Important superconducting materials for the development of superconducting wires….6

Chapter 2

Table 2-1. The specifications of all MgB_2 wires …….. 21

Table 2-2. Details of the fabricated wires …….. 30

Chapter 3

Table 3-1. The details of compared wires in Fig. 4 …….. 44

Table 3-2. The characteristic element spectrum details of B (B k), C (C k), Mg (Mg k) and Si (Si k) for Fig. 5(b) …….. 46

Chapter 4

Table 4-1. The a-axis, c axis, and amount of carbon substitution for boron of IMD-processed mono-core MgB_2 wires with different additives …….. 58

Chapter 5

Table 5-1. Compositions of SMI and SMI+D powders obtained from EDX analysis …….. 69

Table 5-2. MgB_2 area fraction and sheath area fraction for high-performance MgB_2 wires …….. 71

Table 5-3. Lattice parameters, amount of carbon substitution for boron, and calculated and measured T_{ic} for Fe-sheathed wires fabricated using SMI and SMI+D powders …….. 72

Chapter 6

Table 6-1 The properties of PIT-processed MgB_2 wires in this experiment …….. 88

Contents

Chapter 1 Introduction 1

1.1 Superconductivity 1

1.1.1 History 1

1.1.2 Superconducting properties and applications 4

1.1.3 Superconducting materials 5

1.2 MgB_2 7

1.2.1 Characteristics of MgB_2 superconductor 7

1.2.2 MgB_2 superconducting wires 8

1.2.3 Internal Mg diffusion process 9

1.3 Thesis content 12

1.3.1 Research purpose, theory, and research methods 12

1.3.2 The characterization methods 14

1.3.3 The research experience and thesis structure 15

Chapter 2 Development of a new method combining IMD and PIT processes for MgB_2 wires 20

2.1 Introduction 20

2.2 Enhancement of critical current properties of IMD-processed MgB_2 wires by Mg addition 21

2.2.1 Experimental details 21

2.2.2 Results and discussion 22

2.3 Fabrication of MgB_2 wires with a new method combining IMD and PIT processes 30

2.3.1 Experimental details 30

2.3.2 Results and discussion 31

2.4 Conclusions 36

Chapter 3 Fabrication of 37-filamentary IMD-processed MgB_2 wires 38

3.1 Introduction 38

3.2 Experimental details 38

3.3 Results and discussion 40

3.4 Conclusions 48

Chapter 4 Enhancement of critical current properties of IMD-processed MgB_2 wires by SiC and liquid aromatic hydrocarbon co-addition 50
4.1 Introduction 50
4.2 Experimental details 50
4.3 Results and discussion 51
4.3.1 Enhancement of J_c and J_e for MgB_2 wires by SiC and liquid aromatic hydrocarbon co-addition 51
4.3.2 Study on the mechanism of the J_c enhancement of MgB_2 wires by SiC and toluene co-addition 57
4.3.3 The microstructure analysis and a proposal of new mechanism of enhanced J_c of MgB_2 wire by SiC addition 60
4.4 Conclusions 64
Chapter 5 Enhancement of J_c properties of MgB_2 wires by pretreating carbon-coated nano-sized B powder with Dimethylbenzene 66
5.1 Introduction 66
5.2 Experimental details 66
5.3 Results and Discussion 68
5.3.1 Starting B powder 68
5.3.2 Fabrication of wires 70
5.3.3 Critical current properties 73
5.3.4 Scanning electron microscopy analysis 77
5.3.5 Transmission electron microscopy analysis 79
5.4 Conclusions 82
Chapter 6 Enhancement of critical current properties of MgB_2 wires by aromatic hydrocarbon ($C_{24}H_{12}$) addition 84
6.1 Introduction 84
6.2 Experimental details 85
6.3 Results and discussion 86
6.4 Conclusions 92
Chapter 7 Summary and prospects 94
7.1 Summary 94

7.2 Some ongoing topics 98
7.2.1 The comparison of mechanical properties for IMD- and PIT-processed MgB_2 wires 98
7.2.2 Strain measurement of IMD-processed MgB_2 wires by synchrotron radiation at SPring-8 101
7.2.3 Reaction observation of IMD-processed MgB_2 wires during the heat treatment by XRD in Spring-8 102
7.3 Prospects 104
Publications 107

Chapter 1 Introduction

1.1 Superconductivity

1.1.1 History

Superconductivity is a phenomenon of exactly zero electrical resistance and expulsion of magnetic fields occurring in certain materials when cooled below a characteristic critical temperature. In 1911, Heike Kamerlingh Onnes and his colleagues found that the resistivity of solid mercury abruptly disappeared at the temperature of 4.2 K [1]. He termed this phenomenon as "superconductivity".

In 1933 [2], the German physicists Walther Meissner and Robert Ochsenfeld discovered a phenomenon that superconductors expel applied magnetic fields by measuring the magnetic field distribution outside superconducting tin and lead samples. The samples were cooled in an applied magnetic field below their superconducting transition temperature. Below the transition temperature the samples cancelled nearly all interior magnetic fields. This phenomenon has come to be known as the Meissner effect. Heinz London and Fritz London showed that the Meissner effect was a consequence of the minimization of the electromagnetic free energy carried by superconducting current in 1935 [3]. So they proposed two equations that govern the microscopic electric and magnetic fields and termed as London equations. Brian Pippard introduced the notion of coherence length in superconductors in his proposal for the non-local generalisation of the Londons' equation concerning electrodynamics in superfluids and superconductors [4]. The non-local kernel proposed by Pippard can be deduced within the framework of the first microscopic theory-BCS theory of superconductivity. BCS theory was proposed by John Bardeen, Leon Neil Cooper, and John Robert Schrieffer in 1957 [5]. It is wonderfully summarized as [6]: an electron moving through a conductor will attract nearby positive charges in the lattice. This deformation of the lattice causes another electron (with opposite spin) to move into the region of higher positive charge density. The two electrons then become correlated (occupying states with equal and opposite momentum and spin) to form Cooper pairs. Because there are a lot of Cooper pairs in superconductor, these pairs overlap very strongly and form a highly collective condensate. In this "condensed" state, the breaking of one pair will change the energy of not only just a single electron or a single pair, but the entire condensate. Thus, the energy required to break any single pair is related to the energy required to break all of the pairs. Because the pairing increases this energy barrier, kicks from oscillating atoms in the conductor (which are small at sufficiently low temperatures) are not enough to affect the condensate as a whole, or any individual "member

pair" within the condensate. Thus the electrons stay paired together and resist all kicks, and the electron flow as a whole (the current through the superconductor) will not experience resistance.

Before the BCS theory, some other important theories of superconductivity were also devised. Maxwell and Reynolds *et al*. [7] found that the critical temperature of a superconductor depends on the isotopic mass of the constituent element in 1950. This important discovery pointed to the electron-phonon interaction as the microscopic mechanism responsible for superconductivity.

Also in 1950, Landau and Ginzburg [8] devised the Ginzburg-Landau theory, which combined Landau's theory of second-order phase transitions with a Schrödinger-like wave equation, had great success in explaining the macroscopic properties of superconductors. In particular, Abrikosov [9] predicted from Ginzburg-Landau theory that there are two categories of superconductors, which are now referred to as Type I and type-II superconductors. Ginzburg–Landau theory defines two parameters, the superconducting coherence length and the London magnetic field penetration depth to discuss the two types of superconductors. In a type-II superconductor, the coherence length is smaller than the penetration depth. This leads to the negative free energy of the interface between superconducting and normal phases. While for the type-I superconductor, the free energy is positive. These caused that the superconductivity of type-I superconductors are abruptly destroyed via a first order phase transition when the strength of the applied field rises above a critical value H_c. However, type-II superconductors have two critical magnetic fields. The first, lower critical field (H_{c1}) is the field at which magnetic flux vortices start to penetrate the material but the material remains superconducting outside of these microscopic vortices. When the vortex density becomes too large, the entire material becomes non-superconducting; this corresponds to an upper critical field (H_{c2}) [10, 11, 12]. Type-I superconductor is normally exhibited by pure metals, such as Hg, Sn and so on. Type-II superconductors are usually made of metal alloys or complex oxide ceramics. The applications of superconductor are usually related to magnetic fields, so only type-II superconductors are used for practical applications due to their high H_{c2}.

The type-II superconductors allow magnetic flux to enter in quantized packets surrounded by a superconducting current vortex. These sites of penetration are known as flux lines. The number of flux lines per unit area is proportional to the magnetic field with a constant of proportionality equal to the magnetic flux quantum. At low temperatures the flux lines are pinned in place and cannot move. These flux pinning prevent flux creep, which can create a pseudo-resistance and depress both critical current density and critical field [11, 12]. The flux pinning is a very important phenomenon for practical applications of type-II superconductors. At high temperatures de-pinning of flux lines “flux creep” occurs due to the thermal activation.

In 1962, the British physicist Brian David Josephson [13] found a macroscopic quantum phenomenon in superconductors, which is termed as Josephson effect. The Josephson effect is the

phenomenon of supercurrent—i.e. a current that flows indefinitely long without any voltage applied—across a device known as a Josephson junction (JJ), which consists of two superconductors coupled by a weak link (a thin insulating barrier, or a short section of non-superconducting metal). The Josephson effect has wide usages such as superconducting quantum interference devices (SQUID), single-electron transistor, and superconducting quantum computing.

During the development of the theory of superconductivity, discovery of new superconductors are also developed. Fig. 1-1 shows the brief history of discovery of superconductors. The superconducting transition temperature (T_c) is increasing by year. Three stages can be observed from the Fig. 1-1. First stage is before 1980s, the discovery is focus on pure metal and Nb-based compounds. Second stage is 1980-2000, the discovery of cuprates with high T_c is a milestone for science. In 1986, Bednorz and Müller [14] discovered superconductivity in a lanthanum-based cuprate perovskite material, which had a transition temperature of 35 K (Nobel Prize in Physics, 1987). Soon after that, the YBCO [15] and Bi-based [16] superconductors with the T_c higher than 77 K (liquid Nitrogen) are discovered. HgBaCaCuO show the highest T_c value of 135 K [17]. Meanwhile, some other compounds are detected with superconductivity in this period. Third stage is after 2000, there is no increase in T_c of superconductivity, but different types of superconductors are discovered. In which, MgB_2 found in 2001 [18] and Fe-based superconductors found in 2008 [19] are most attractive.

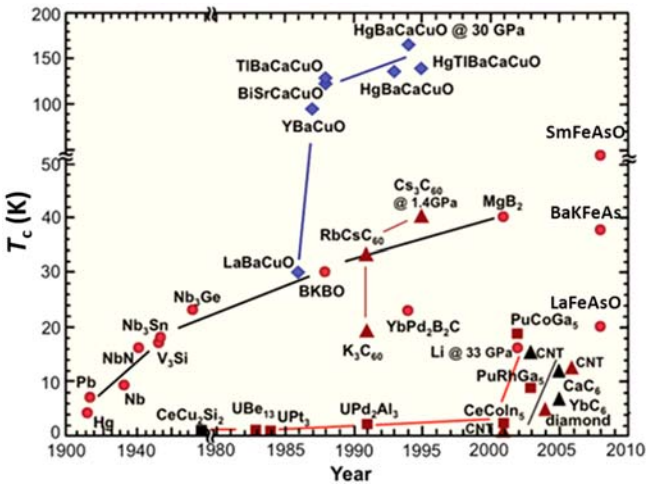

Fig. 1-1 Brief history of discovery of superconductors

In about 100-years history of superconductor, five Nobel prizes have been awarded for the scientists: Heike Kamerlingh Onnes (Discovery of superconductivity, 1913), John Bardeen, Leon N. Cooper, and J. Robert Schrieffer (BCS theory, 1972), Brian D. Josephson (Josephson effect, 1973), Georg Bednorz and K. Alex Müller (Discovery of superconductivity in cuprate perovskite, 1987),

Alexei A. Abrikosov, Vitaly L. Ginzburg, and Anthony J. Leggett (type-II superconductor, 2003). Although there are a lot of new superconductors are being discovered, the mechanism of superconductivity is still unclear, meanwhile the superconductor with high T_c (such as room temperature) are still the dream for human beings. But superconductors have begun to be widely applied because of its special properties.

1.1.2 Superconducting properties and applications

Application is the goal of the research for any materials including superconductor. The properties of superconductor decide its applications. In this section, I will first introduce the basic superconducting properties, and then introduce the application of superconductors. As introduced in the 1.1.1, most superconductors used for practical applications are type-II superconductors, due to their high upper critical fields. So the discussions below are focused on type-II superconductors.

Fig. 1-2 shows the most important properties of superconducting materials. The relations among T_c, critical magnetic field (H_c, for type-II superconductor this is upper critical magnetic field, H_{c2}), and critical current density (J_c), are shown in Fig. 1-2. The surface in this three dimensional figure is the critical interface between the superconducting state and normal state. Inside the surface is the superconducting state, while outside is the normal state. The key properties of superconducting wires are their T_c, H_{c2}, J_c. T_c and H_{c2} are intrinsic properties of superconductors, and their values for superconducting wires are almost determined by the type of superconducting material used. In contrast, J_c is an extrinsic property, and mainly depends on the microstructure of the superconductor. Therefore, the research on superconducting wires should be focused on the enhancement of J_c by controlling the microstructure.

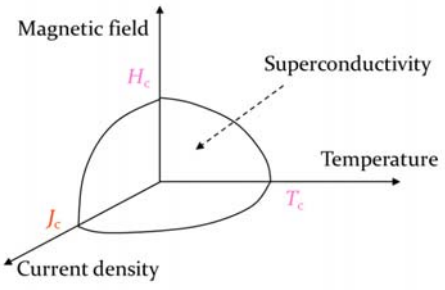

Fig. 1-2 The properties of a superconducting material

Superconductors are mainly used in the following fields:

(1) Superconducting magnets: The superconducting magnets are mainly used in MRI, NMR, and the beam-steering magnets (used in particle accelerators). They can also be used for magnetic separation, such as in the environment and pigment industries.

(2) Electric applications: such as power storage devices (SMES), transformers, electric motors magnetic levitation devices (e.g. maglev trains), fault current limiters and power cables. However, superconductivity is sensitive to changing magnetic fields, so applications that use alternating current (e.g. transformers) will be more difficult to develop than those that use direct current.

(3) superconducting quantum interference device (SQUID): superconductor is used to build Josephson junction which is the essential element of SQUID. SQUID is the most sensitive magnetometer to date.

(4) Superconducting device: superconductors were used to build experimental digital computers using cryotron switches. They are also used to make digital circuits based on rapid single flux quantum technology and RF and microwave filters for mobile phone base stations.

1.1.3 Superconducting materials

Table. 1-1 summarizes the important superconducting material for the development of superconducting wires [20]. Their T_c and H_{c2} are also listed for comparison. The most widely used superconducting materials are Nb-Ti and Nb_3Sn, They are metallic superconductors, and are also low temperature superconductors (LTS). Nb-Ti is relatively easy to fabricate in superconducting wires, and occupies most of the low field magnets such as in MRI. Nb_3Sn is used for high field magnets. Both Nb-Ti and Nb_3Sn based magnets require liquid helium (LHe) as the coolant due to the low T_c, so their operating cost is expensive. High-temperature superconductors (HTS) with T_c exceeding 77K have been widely studied since their discovery. Among them, Bi- and Y-based oxides are used for the development of superconducting wires cooled in liquid nitrogen which is much cheaper than LHe. But the HTS have many technical problems in making wires and coils. They have high anisotropy and only highly textured conductors have desirable performance. That is why the present HTS based magnets are mostly applied in low temperature. Fe-based superconductors have been attracting scientists since its discovery [19] because they contain ferromagnetic element, Fe, as a constituent. Some groups have reached good critical current properties with wires and tapes [21-23]. The J_c dependence on magnetic field is very small which suggests that it is promising to be used for high field magnet. However, the toxic element arsenic may limit its practical applications.

Since its discovery in 2001 [18], MgB_2 with a transition temperature (T_c) at 39 K is expected to be used in liquid-helium-free conditions to replace metallic superconductors that are operated in a liquid helium environment. In contrast to high-T_c oxide superconductors, MgB_2 exhibits fairly strong grain coupling, indicating that grain alignment is not essential for obtaining high superconducting transport currents. This is a big advantage because the MgB_2 wires can be fabricated using a simple low-cost process. Furthermore, the abundant, low-weight, and environment-friendly raw materials that are used are special advantages compared to all other superconducting materials. Based on these advantages, MgB_2 appears to be an excellent candidate as a low-cost superconductor for large-scale applications. However, the critical current property of present MgB_2 wires is still low and needs to be enhanced for large-scale applications.

Table 1-1 Important superconducting materials for the development of superconducting wires

Superconducting material	T_c (K)	H_{c2} at 4.2 K (T)
Oxide superconductor **(HTS)**		
$YBa_2Cu_3O_x$	92	>100
$Bi_2Sr_2CaCu_2O_y$	90	
$Bi_2Sr_2Ca_2Cu_3O_z$	110	
$Tl_2Ba_2Ca_2Cu_3O_w$	125	
$HgBa_2Ca_2Cu_3O_v$	135	
Metallic superconductor **(LTS)**		
Nb–Ti	9.8	11.5
Nb–Zr	10.5	11
V_3Ga	16	25
Nb_3Sn	18	25
Nb_3Al	18	32
$Nb_3(Al,Ge)$	20	43
Nb_3Ga	20	34
Nb_3Ge	23	37
$V_2(Hf,Zr)$	10.1	23
NbCN	17.8	12
MgB_2	39	25
Fe-based superconductor **(LTS)**		
$SmFeAsO_{1-x}F_x$	55	>100
$(Ba_{1-x}K_x)Fe_2As_2$	38	70

1.2 MgB_2

1.2.1 Characteristics of MgB_2 superconductor

MgB_2 has a hexagonal crystal structure as shown in Fig. 1-3 [24]. The boron atoms form graphite-like honeycomb network and the Mg atoms are located at the pores of these hexagons. The in-plane B–B distance is almost half the inter-plane B–B distance. The Mg atom donates its valence electrons to the boron planes, which form ionic bonds with the boron atoms. The mechanism of superconductivity in MgB_2 was widely studied [25-27]. Eisterer M summarized it as [27]: Two three-dimensional (3D) metallic π -bands arise from the boron P_z orbits. One band is electron type, and the other is hole type. Two σ -bands formed by the covalent p_{xy} orbitals which are deep beneath the Fermi energy in graphite cross the Fermi level in MgB_2. Charge is transferred from the σ - to the π -bands and holes are introduced in the σ -bands. The σ -bands retain their covalent character which is a peculiar feature of MgB_2. While the charge carriers of the π -bands are delocalized over the whole crystal, the σ -band holes are localized within the boron layers and the σ -bands are two dimensional (2D). The holes in the σ -bands strongly couple to the optical E_{2g} phonons (in plane boron bond stretching mode), which is mainly responsible for superconductivity in MgB_2. The π -band charge carriers become superconducting, too, although with significantly smaller energy gap, 2 meV. While energy gap of σ -bands is 7 meV.

MgB_2 is a brittle ceramics like the HTS materials. The anisotropy of MgB_2 (1.5~5) is lower than that of HTS [28], which suggests no grain orientation is needed for wire fabrication. This is in contrast to HTS. The coherence length of MgB_2 is 4–5 nm and the penetration depth is 100–140 nm at absolute zero kelvin [29]. Due to the large coherence length, larger than the interatomic spacing, the weak link problem is not severe in MgB_2. MgB_2 has a very sharp $T_{c\text{-onset}}$ of 39–40 K and has a very narrow transition width of less than 1 K. The isotopic B^{10} substitution slightly increases the $T_{c\text{-onset}}$ to 40.25 K [30]. Most of the element substitutions in MgB_2 resulted in a decrease of T_c.

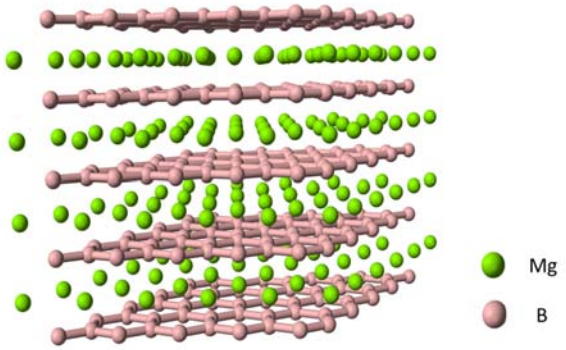

Fig. 1-3 Crystal structure of MgB_2

1.2.2 MgB_2 superconducting wires

Mostly it is necessary to fabricate wire for applications of superconducting material. The most important property of superconducting wires for practical application is current transport ability (critical current density, J_c) in magnetic field. J_c is divided critical current (I_c) by MgB_2 cross sectional area. Engineering J_c (J_e) which is divided I_c by the whole cross sectional area of wire, is more important for practical applications. The critical current properties (J_c and J_e) of superconducting wires are governed by their microstructure and composition.

Some companies (Hype tech in USA [31], Columbus in Italy [32], and Hitachi in Japan [33]) have produced MgB_2 wires for products. The applications using MgB_2 such as MRI [34], SMES [35], and liquid H_2 level sensor [36] were studied at some labs in the world. Because the critical current properties of present MgB_2 wires are still low, most of these applications are considered in low field and low temperature such as 10-20 K. These temperatures can be obtained under liquid-helium-free condition using cryocooler. As introduced above, low cost is the most important advantage of MgB_2 wires. For large-scale practical applications, the critical current properties should be improved to save the operating cost (no helium). In order to meet these requirements of application, the critical current properties in 20 K (liquid hydrogen) and a high magnetic field of around 5 T should be enhanced.

Currently, powder in tube (PIT) process shown in Fig. 1-4 is the most popular method for the fabrication of MgB_2 wires. The starting powders were first packed into a tube, and then the tube was groove-rolled and drawn into a wire with demand diameter, finally the obtained wire was heat treated in a furnace to form MgB_2 wires.

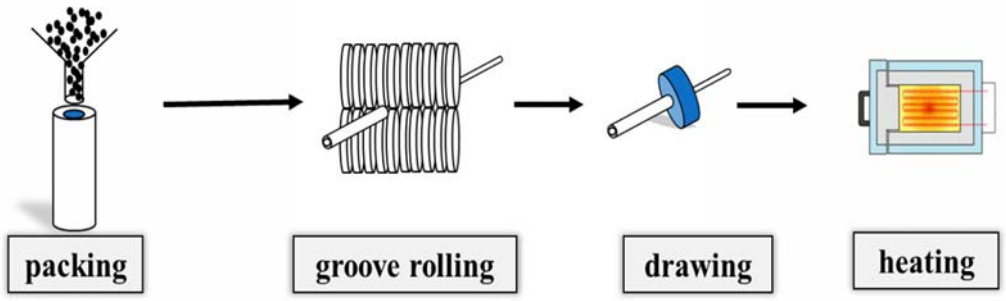

Fig. 1-4 Fabrication of MgB_2 wires with PIT process

PIT process was divided into two categories with respect to the starting powder. MgB_2 powder is used for *ex situ* PIT [37-40], while mixture of Mg powder and B powder for *in situ* PIT [41-47].

The advantage of *ex situ* PIT process is that we can easily obtain high density MgB_2 core. However, we need high temperature heat treatment (higher than 900 ℃) to obtain good connectivity of MgB_2 grains. Furthermore, impurity addition is not so easy as *in situ* method.

The *in situ* PIT process is widely used for the fabrication of MgB_2 wires. However, the reaction between Mg and B to form MgB_2 causes the volume-shrink (thus voids formation) in MgB_2 layer, resulting in the low density MgB_2 core. This low density MgB_2 core obtained by *in situ* PIT process leads to its low J_c [48, 49]. Some methods such as mixing powders [50], high pressure [51], cold pressure [52] and hot pressing [53], are reported to increase the MgB_2 packing density and to enhance the J_c values. Yamada *et al* [53] obtained high J_c of 4.5 x 10^4 A/cm^2 at 10 T and 4.2 K by hot pressing. However, these methods increase the cost of the wire fabrication.

1.2.3 Internal Mg diffusion process

If we separate Mg and B (that is Mg diffuse to B layer from a separated place) to form MgB_2, we can decrease the voids in MgB_2 layer. Giunchi *et al*. [54-56] first used an Mg diffusion method, and decreased the void formation problem effectively. They used a steel pipe as outer sheath, and Nb tube as an inner tube, in which a coaxial internal Mg rod and B powder was filled, to fabricate mono-filamentary and 7-filamentary wires. During the heat treatment, Mg (from the Mg rod) diffused to the B layer and reacted with B to form high density MgB_2 layer.

Our group has been studying this method and we have termed it as internal Mg diffusion (IMD) process. This process is shown in Fig. 1-5. An Mg rod was inserted into the center of a metal tube. Amorphous B powders (sometimes with additive) were packed into the space between the Mg rod and the tube. The composite billet was then cold worked to a wire by groove rolling and drawing, and then the wire was heat treated.

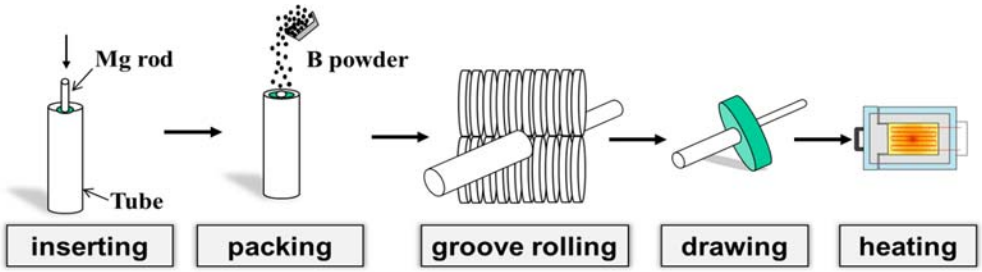

Fig. 1-5 Fabrication of MgB_2 wires by IMD process

Fig. 1-6(a) and (b) show typical transverse and longitudinal cross sections of IMD-processed wire before heat treatment observed by an optical microscopy, respectively. The cross sections show uniform deformation of the composite. As we know, pure Mg has poor deformability at room temperature. However, the existence of B powder surrounding Mg rod improved the deformability of pure Mg rod. Fig. 1-6(c) and (d) show transverse and longitudinal cross section of IMD-processed MgB_2 wire after heat treatment, respectively. MgB_2 layer is formed uniformly along the Fe inner wall and at the center a large hole is generated. Increase of the MgB_2 area fraction, both by decreasing of the hole in wire center and decreasing the sheath area, can increase the engineering critical current density (J_e) of IMD-processed MgB_2 wires.

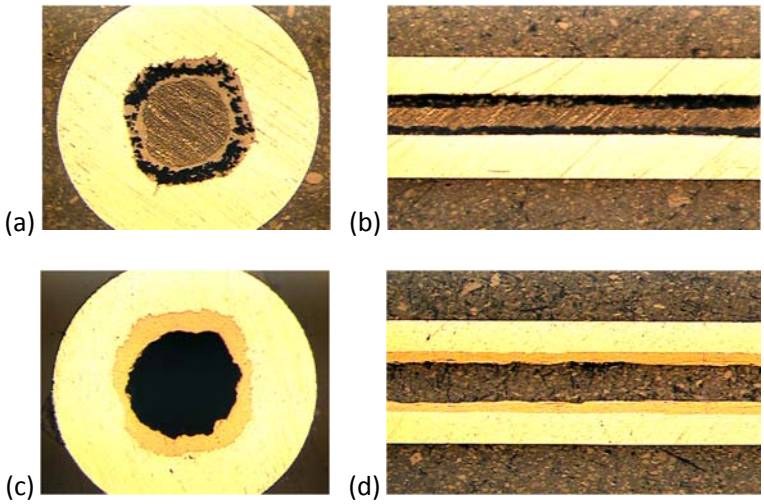

Fig. 1-6 Typical optical microscopy of cross sectional images of IMD-processed MgB_2 wire with diameter of 1.2 mm by optical microscopy, (a) transverse and (b) longitudinal cross section before heat treatment, (c) transverse and (d) longitudinal cross section after heat treatment

Fig. 1-7 shows several IMD-processed MgB_2 wires. Uniform MgB_2 layers are observed along the inner wall of Fe sheath for all wires, which suggests that the IMD process can be used to fabricate large-scale MgB_2 wires with uniform MgB_2 layer.

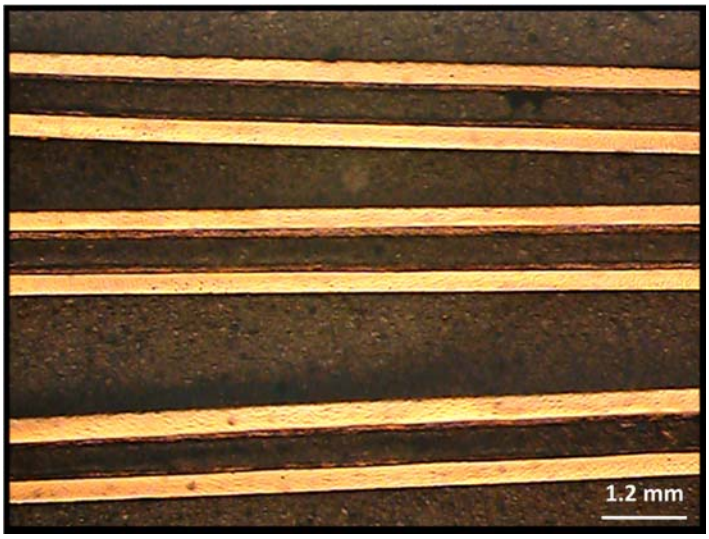

Fig. 1-7 The uniformity in longitudinal direction of the several IMD-processed MgB_2 wires

Fig. 1-8 (a) and (b) show the typical SEM images of the MgB_2 layer of IMD and PIT-processed MgB_2 wires, respectively. The MgB_2 layer of IMD-processed wire is dense while the MgB_2 layer of PIT-processed wire contains many voids and impurities. But the IMD-processed MgB_2 layers have many uneven black spots which are the un-reacted boron or the boron-rich phase as discussed in chapters 2-4.

(a)

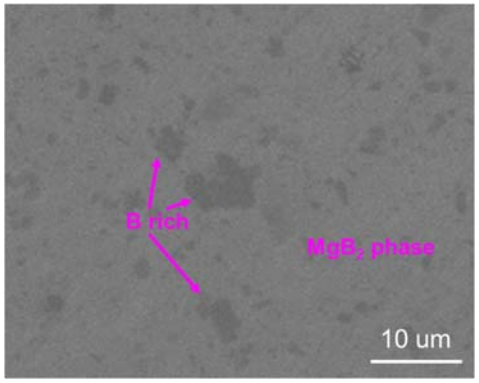

(b)

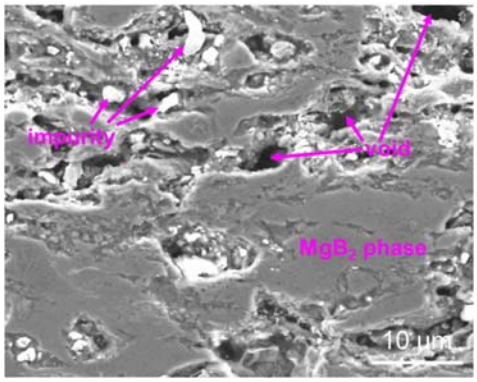

Fig. 1-8 Typical SEM image of MgB_2 wires (a) IMD processed MgB_2 wires, (b) PIT processed MgB_2 wires

1.3 Thesis content

1.3.1 Research purpose, theory, and research methods

The title of this thesis is "the development of high performance MgB_2 wires". Low cost is the most important advantage of MgB_2 to be used as a practical superconducting wire. The purpose of this research is to develop MgB_2 superconducting wires for practical applications with low cost. Currently, there have already been products using MgB_2 superconductors, but the cost of these products are not so low because the critical current properties of these MgB_2 wires are not high enough to operate in the expected condition. The expected condition for MgB_2 wire operation is the operation at ~20 K using a cryocooler or liquid hydrogen. Considering the industrial applications of MgB_2 wires, the J_c of 1.0 x 10^5 A/cm^2 and J_e of 2 x 10^4 A/cm^2 at 20 K and 5 T should be the target values of MgB_2 wire development. Thus the main task of my study is to enhance the critical current properties for MgB_2 wires at 20 K and 5 T. However, I mostly studied the J_c and J_e value at 4.2 K and 10 T, because I_c can be more easily measured under this condition than those at 20 K and 5 T. Although there seems to be no liner relations between the 4.2K^10T and 20K^5T, I select the good samples referring to I_c at 4.2K^10T for the I_c measurement at 20K^5T.

Collings E W *et al*. [57] summarized how to improve the critical current properties of MgB_2 superconducting wires. They considered that there are mainly four factors which determine the critical current properties of MgB_2 wires.

(a) The H_{c2}: The H_{c2} of MgB_2 can be enhanced by dopant. Many effective dopants have been reported for MgB_2. Among them, only C-containing materials have turned out to be the most promising. Carbon atoms substituted for B site produce strong impurity scattering in the π band (as well as the σ band), which is responsible for the increase of H_{c2}. There are many C-containing materials, such as elemental C, C-containing inorganic and organic compounds. The most popular dopant is SiC.

(b) Flux pinning: Some kinds of impurities are effective flux pinning centers. But the main flux pinning center in MgB_2 is flux pinning at grain boundaries. Therefore, small grain size increases the flux pinning at grain boundaries. Impurities also affect the flux pinning at grain boundaries because some impurities can prevent the grain growth, resulting in a small grain size.

(c) Connectivity: Sometimes insulating MgO or amorphous BO_x layers were observed at MgB_2 grain boundaries. These layers are obstacles of superconducting current. Anisotropy has also influence on grain-to-grain current flow in untextured polycrystalline materials, so it is also addressed as a factor affecting connectivity.

(d) Porosity: Porosity (and also voids) is commonly observed in PIT-processed MgB_2 wires, especially, in situ PIT-processed wires. The reduction of porosity is very important to increase J_c of MgB_2 wires.

Taking into account of the factors summarized by Collings E W *et al.* [57] and research situation when I started the work, I designed my methods to study the MgB_2 wires as follows:

1. I selected IMD process for fabricating MgB_2 wires because the PIT process has the voids (porosity) problem for both ex situ and in situ PIT processes. Furthermore, IMD process improves the connectivity by decreasing MgO. Compared to Mg powder used for PIT process, the Mg rod used for IMD process contains less amount of MgO.

2. J_e increases with increasing the MgB_2 area fraction for IMD-processed MgB_2 wires. Decrease in hole of the wire center and decrease of sheath area can both increase the MgB_2 area fraction.

3. J_c increases by the improvement of the reaction between Mg and B for IMD-processed MgB_2 wires. Decrease in un-reacted B particles and decrease in B-rich region can be both obtained by the improvement of the reaction between Mg and B.

4. Multi-filamentary IMD-processed MgB_2 wires are developed. The multi-filamentary IMD wires decrease the MgB_2 filament size, resulting in decrease of the Mg diffusion distance, which can improve reaction between Mg and B. Furthermore, the multi-filamentary MgB_2 wires show good stability which is suitable for practical applications.

5. Carbon-containing material addition is effective to improve J_c values for the IMD-processed MgB_2 wires as well as PIT-processed MgB_2 wires. Our group has already obtained good results by applying SiC addition to IMD MgB_2 wires. However, the uniform dispersion of additive is very important. It is not easy to obtain a uniform mixture of solid SiC and solid B powders. Hence I tried to add a liquid aromatic hydrocarbon to obtain a uniform mixture of SiC and B powders. This is my original consideration though other groups also used the liquid aromatic hydrocarbon for PIT-processed wires. Furthermore, the liquid aromatic hydrocarbon can be absorbed on the surface of B powder, which can (1) increase the amount of carbon substitution for B (increase H_{c2}), and (2) prevent the MgB_2 grain growth (increase flux pinning at grain boundaries), thus enhancement of J_c.

6. Organics addition, especially aromatic hydrocarbon addition, is searched to improve J_c values. The aromatic hydrocarbons have only carbon and hydrogen in molecule, and they have the highest carbon content in all organics; hence they take less impurity (such as oxide) to MgB_2 wire. Furthermore, they are more stable than other elemental carbon such as carbon nano particles. Compared to the inorganics, the low boiling point and decomposing temperature make them easy to obtain the uniform fresh carbon. This fresh carbon can both substitute for B and work as pinning center. My chemistry knowledge is also useful to search the ideal aromatic hydrocarbon.

7. A new inorganic additive without carbon is searched to improve J_c values. Carbon substitution for B enhances J_c only in high magnetic field. However, J_c in low field decreases because carbon decreases the connectivity of MgB_2 grains. A new additive is expected to increase J_c in both high field and low fields.

8. The B powder was refined. Chemistry solvent is expected to remove the impurities absorbed on the surface of B powders.

The details of my research plan are introduced in the *1.3.3*. I selected the IMD process for my Ph.D work as described in 1. In order to deal with 2 and 3, I tried to add Mg powder to B layer of IMD-processed MgB_2 wire, and then developed a new method by a combination of IMD and PIT. These works are introduced in chapter 2. The 4 is introduced in chapter 3, the fabrication of IMD-processed 37-filamentary MgB_2 wire was first successfully carried out. The 5 is carried out in chapter 4, SiC and liquid aromatic hydrocarbon co-addition is introduced. The 6, organics addition, is carried out in chapter 6. This work is to replace the carbon-coated nano-sized B powder introduced in chapter 5. A lot of materials are tried for the 7. I don't describe them in this thesis because they are mostly failed. Chapter 5 and 6 can also be considered as examples for refining B powder described in the 8.

1.3.2 The characterization methods

The low transport critical current properties are the bottleneck for the development of high performance MgB_2 wires for large-scale practical applications with low cost. In this study, I mainly estimated the critical current properties for MgB_2 wires. The value of J_c for each wire was calculated by dividing transport critical current (I_c) by the whole cross sectional area of MgB_2 layer including B-rich region. Furthermore, the engineering J_c (J_e) calculated by dividing I_c by the entire wire area in the transverse cross section was also estimated. The I_c values for the wire were measured at temperatures of 4.2, 10, 15, 20, 25, and 30 K in magnetic fields below 18 T using a four-probe resistance method. The two current probes were soldered to either end of a 4-cm-long wire and the two voltage probes were soldered to the middle of the wire, with a spacing of 1 cm between them. I_c was defined as a voltage drop of 1 μV across the voltage probes.

The microstructures were observed by the optical microscope (OM), Scanning Electron Microscope (SEM), Transmission Electron Microscope (TEM), and scanning TEM (STEM). Structural analyses were carried out with X-ray diffraction (XRD) analysis, Energy dispersive X-ray spectroscopy (EDX), and Electron energy loss spectroscopy (EELS).

1.3.3 The research experience and thesis structure

In 2008, Hur *et al*. [58] fabricated the IMD-processed MgB_2 wires with SiC-added B powder (99.99%, 300-mesh, Sigma-Aldrich Co.), and obtained a much improved J_c of 4.1 x 10^4 A/cm^2 at 4.2 K and 10 T. Then Togano *et al*. [59, 60] and Kumakura *et al*. [61] fabricated multi-filamentary (7 and 19 filaments) IMD wires. Their J_c values for the MgB_2 layer achieved as high as 1 x 10^5 A/cm^2 at 4.2 K and 10 T. As introduced above, these high J_c values are mostly due to the high density MgB_2 layer produced by IMD process.

In 2007, Yamada *et al*. [62] reported that the SiC and ethyltoluene co-added MgB_2 wire showed higher J_c than the only SiC-added wire.

Accordingly, I started my work by applying the SiC and ethyltoluene co-addition to IMD-processed MgB_2 wire. Co-addition of SiC and toluene, and SiC and dimethylbenzene were also tried to IMD MgB_2 wires. And I found that they were more effective than SiC and ethyltoluene co-addition [63]. Through the observation of microstructure, I found that the un-reacted B particles exist in IMD MgB_2 wires [64]. In order to decrease the un-reacted B particles, I added Mg powder to B layer of IMD MgB_2 wires and developed a new method which combined IMD and PIT processes for MgB_2 wire fabrication. This new method increase J_e of MgB_2 wires by increasing MgB_2 area fraction. We also found that using carbon-coated nano-sized B powder to replace the SiC addition can obtain high J_c values with less un-reacted B particles. Thus, I mainly separated my Ph.D thesis in two parts. The first part is the fabrication of MgB_2 wire. The new method combining IMD and PIT processes (chapter 2) and 37-filamentary IMD-processed MgB_2 wires (chapter 3) were described. The second part is impurity addition. The SiC and liquid aromatic hydrocarbon co-addition to 325-mesh B powder (chapter 4), nano-sized B powder with C-coating (chapter 5), and nano-sized B powder with coronene addition (chapter 6) were described.

In chapter 2, I tried to add Mg powder to IMD-processed MgB_2 wires and decreased the un-reacted B particles [65]. The mechanism of decreasing the un-reacted B particles by the Mg powder addition is considered to be that the added Mg power decreases the required Mg diffusion distance and improves the reaction between Mg and B. However, the Mg powder addition also caused void formation as in the case of PIT process. These voids decrease the J_c values. I found that the J_c and J_e are influenced by the un-reacted B particles and the voids. If I continue to add the Mg powder in B layer of IMD-processed MgB_2 wires, the Mg rod should be decreased to make a balance between Mg and B. Based on this consideration, a new method which combined IMD and PIT processes is developed [66]. By this new method, the hole in the center of IMD-processed MgB_2 wires can be decreased, simultaneously the thickness of MgB_2 layer can be increased. Both decrease of hole and increase of MgB_2 layer thickness cause the increase of MgB_2 area fraction, thus increase the J_e of IMD-processed MgB_2 wires [58-61].

In chapter 3, I successfully fabricated 37-filamentary IMD-processed MgB_2 wires [67]. The critical current properties, microstructure, and impurity addition were investigated. The filament size of as small as 100 μm was realized in the IMD-processed MgB_2 wires. Furthermore, this study directly proved that the short B layer thickness can decrease the amount of un-reacted B particles. The successful fabrication of 37-filamentary wire suggests that IMD process can be used to fabricate the long MgB_2 wires for large-scale practical applications.

In chapter 4, SiC and liquid aromatic hydrocarbon co-addition to IMD-processed MgB_2 wires fabricated with low quality B powders (325-mesh, 99%) was described. As introduced above, this works is not only the starting point, but also the jointing point of two parts in my Ph.D thesis as introduced above.

All the works in chapters 2-4 were carried out with the low quality B powders (325-mesh, 99%). It was difficult to import high quality amorphous B powder because it can be used to produce the weapon. When I was doing the work introduced in chapters 2-4, the Ohio state university and hyper tech company used a special plasma-synthesized carbon-coated B powder (Special Materials Inc., SMI powder) to fabricate thin IMD-processed MgB_2 wires (diameter: 0.55 mm) with Nb and Monel double sheaths, and they obtained a high J_c and J_e values for IMD processed MgB_2 wires [68]. I also got this B powders, but I found it was difficult to obtain the high critical current as theirs if I don't apply pre-treatment to the B powder. This leads to the work below.

In chapter 5, I pretreated the C-coated nano-sized B powder by dimethylbenzene and fabricated the IMD-processed MgB_2 wires. The higher critical current properties than those of Ohio state university were obtained [69, 70]. The dimethylbenzene decreases Cl in the B powders, which is the main reason for higher J_c I obtained. Ohio state university recently reported a higher J_c value at 4.2 K and 10 T in their paper [71]. However, there are arguments because they calculated the J_c by MgB_2 area without the B-rich region. In fact, there is MgB_2 in the B-rich region who transports the superconducting current.

Although the high critical current densities were obtained from the SMI B powder, my experiments showed that this B powder is unstable [69, 70]. In addition, this B powder is expensive due to its complex synthesis process [72]. I changed this B powder for another B powder which is discussed in chapter 6.

In chapter 6, we used a new B powder, which is also nano-sized, but undoped B powder. I added an aromatic hydrocarbon (coronene, $C_{24}H_{12}$) to this new B powder and fabricated IMD-processed MgB_2 wires with a diameter of 0.6 mm. I obtained the same level critical current properties as the SMI B powders [68-71]. The B powder without carbon-coating is much stable and cheap, which are due to its simple synthesis process. The $C_{24}H_{12}$ is a popular organic material with no toxicity. The result in chapter 6 is expected to be used in the practical level long wire fabrication.

In addition, Chapter 1 introduced the background and contents of this thesis. In chapter 7, firstly the thesis was summarized. Then some on-going works are introduced. Finally, the future works are proposed.

Reference

[1] Onnes Kamerlingh H 1911 *Leiden Comm.* 120b, 122b, 124c
[2] Meissner W and Ochsenfeld R 1933 *Naturwiss* 21 787
[3] London F and London H 1935 *Physica* 2 341
[4] Pippard A B 1953 *Proc. Roy. SoC* A216 547
[5] Bardeen J, Cooper L N and Schrieffer J R *Phys. Rev* 108 1175
[6] http://en.wikipedia.org/wiki/BCS_theory
[7] Maxwell E 1950 *Physical Review* 78 477
[8] Ginzburg V L and Landau L D 1950 *Zh. Eksp. Teor. Fiz.* 20 1064
[9] Abrikosov A A 1957 *Zh. Eksp. Teor. Fiz.* 32 1442
[10] Bean C P 1962 *Phys. Rev. Lett.* 8 250
[11] Tinkham M 2004 *Introduction to superconductivity* ISBN 0-486-43503-2
[12]Zhang Y H 2008 *ChaoDaoWuLi* ISBN 978-7-312-02177-0
[13] Josephson B D1962 *Physics Letters* **1**, 251
[14] Bednorz J G, Muller K A, 1986 Z. *Phys. B* 64 189‑193.
[15] Wu M K, Ashburn J R, Torng C J, Hor P H, Meng R L, Gao L, Huang Z J, Wang Y Q, Chu C W, 1987 *Phys. Rev. Lett.* 58 908
[16] Maeda H, Tanaka Y, Fukutomi M, Asano T, 1988 *Jpn. J. Appl. Phys.* 27 L209
[17] Lee S, Mun M O, Bae M K and Lee S L 1994 *J. Mater. Chem.* 4 991
[18] Nagamatsu J, Nakagawa N, Muranaka T, Zenitani Y and Akimitsu J 2001 *Nature* 410 63
[19] Kamihara Y, Watanabe T, Hirano M and Hosono H 2008 *J. Am. Chem. Soc.* 130 3296
[20] Kumakura H 2012 *Japanese Journal of Applied Physics* 51 010003
[21] Ma Y 2012 *Supercond. Sci. Technol.* 25 113001
[22] Weiss J D, Tarantini C, Jiang J, Kametani F, Polyanskii A A, Larbalestier D C and Hellstrom E E 2012 *Nature Mater.* 11 682
[23] Togano K, Matsumoto A and Kumakura H 2012 *Solid State Commun*. 152 740
[24] http://en.wikipedia.org/wiki/Magnesium_diboride
[25] An J M and Pickett W E 2001 *Phys. Rev. Lett*. 86 4366
[26] Mazin I I and Antropov V P 2003 *Physica C* 385 49
[27] Eisterer M 2007 *Supercond. Sci. Technol.* 20 R47
[28] Vinod K, Abhilash K R G and Syamaprasad U 2007 *Supercond. Sci. Technol.* 20 R1

[29] Finnemore D K, Ostenson J E, Bud'ko S L, Lapertot G and Canfield P C 2001 *Phys. Rev. Lett.* 86 2420
[30] Hinks D G, Claus H and Jorgensen J D 2001 *Nature* 411 457
[31] http://www.hypertechresearch.com/
[32] http://www.columbussuperconductors.com/
[33] http://search.hitachi.co.jp/sitesearch/HITACHI?SITE=HITACHI&LANG=JA&PL=JA&Q=MgB_2
[34] http://www.columbussuperconductors.com/
[35] ieeexplore.ieee.org/iel5/77/6366257/06384697.pdf?arnumber=6384697
[36] http://www.lib.kobe-u.ac.jp/repository/81003939.pdf#search= 'MgB_2+%E6%B6%B2%E9%9D%A2 %E8%A8%88'
[37] Grasso G, Malagoni A, Ferdeghini C, Roncallo R, Braccini V and Siri A S 2001 *Appl. Phys. Lett.* 79 230
[38] Braccini V, Nardelli D, Penco R and Grasso G 2007 *Physica C* 456 209
[39] Fujii H, Togano K and Ozawa K 2007 J. Mater. Res. 22 1281
[40] Glowacki B A, Majoros M, Vickers M, Evetts J E, Shi Y and McDougall I 2001 *Supercond. Sci. Technol.* 14 193
[41] Suo H, Beneduce C, Dhalle M, Musolino N, Genoud Y and Flukiger R 2001 *Appl. Phys. Lett.* 79 3116
[42] Kumakura H, Matsumoto A, Fujii H and Togano K 2004 *Appl. Phys. Lett.* 84 3669
[43] Goldacker W, Schlachter S I, Obst B and Eisterer M 2004 *Supercond. Sci. Technol.* 17 S490
[44] Sumption M D, Bhatia M, Dou S X, Rindfleisch M, Tomsic M, Arda L, Ozdemir M, Hascicek Y and Collings E W 2004 *Supercond. Sci. Technol*. 17 1180
[45] Kim J H, Zhou S, Hossain M S A, Pan A V and Dou S X 2006 *Appl. Phys. Lett.* 89 142505
[46] Tomsic M J, Rindfleish M A, Yue J, McFadden K, Doll D, Phillips J, Sumption M D, Bhatia M, Bohnenstiehl S D and Collings E W 2007 *Physica C* 456 203
[47] Flukiger R, Hossain M S A and Senatore C 2009 *Supercond. Sci. Technol*. 22 085002
[48] Matsumoto A, Kumakura H, Kitaguchi H, Senkowicz B J, Jewell M C, Hellstrom E E, Zhu Y, Voyles P M and Larbalestier D C 2006 *Appl. Phys. Lett.* 89 132508
[49] Kim J H, Oh S, Heo Y U, Hata S, Kumakura H, Matsumoto A, Mitsuhara M, Choi S, Shimada Y, Maeda M, MacManus-Driscoll J and Dou S X 2012 *NPG Asia Materials* 4 e3
[50] Pan A V, Zhou S, Liu H and Dou S 2003 *Supercond. Sci. Technol.* 16, 639
[51] Prikhna T A, Gawalek W, Savchuk Ya M, Habisreuther T, Wendt M, Sergienko N V, Moshchil V E, Nagorny P, Schmidt Ch, Dellith J, Dittrich U, Litzkendorf D, Melnikov V S and Sverdun V B 2007 *Supercond. Sci. Technol.* 20, S257
[52] Flukiger R, Hossain M S A, and Senatore C 2009 *Supercond. Sci. Technol.* 22 085002
[53] Yamada H, Igarashi M, Nemoto Y, Yamada Y, Tachikawa K, Kitaguchi H, Matsumoto A and Kumakura H 2010 *Supercond. Sci. Technol.* 23 045030
[54] Giunchi G, Ceresara S, Ripamonti G, Di Zenobio A, Rossi S, Chiarelli S, Spadoni M, Wesche R and Bruzzone P L 2003 *Supercond. Sci. Technol*. 16 285

[55] Giunchi G 2003 *Int. J. Mod. Phys. B* 17 453
[56] Giunchi G, Ripamonti G, Perini E, Cavallin T and Bassani E 2007 *IEEE Trans. Appl. Supercond.* 17 2761
[57] Collings E W, Sumption M D, Bhatia M, Susner M A and Bohnenstiehl S D 2008 S*upercond. Sci. Technol.* 21 103001
[58] J. Hur, K. Togano, A. Matsumoto, H. Kumakura, H. Wada, K. Kimura 2008 *Supercond. Sci. Technol*. 21 032001
[59] K. Togano, J. Hur, A. Matsumoto, H. Kumakura 2009 *Supercond. Sci. Technol*. 22 015003
[60] K. Togano, J. Hur, A. Matsumoto, H. Kumakura 2010 *Supercond. Sci. Technol.* 23 085002
[61] H. Kumakura, J. Hur, K. Togano, A. Matsumoto, H. Wada, K. Kimura 2011 *IEEE Transactions on Applied Superconductivity* 21 2463
[62] H. Yamada, N. Uchiyama, A. Matsumoto, H. Kitaguchi H, Kumakura 2007 *Supercond. Sci. Technol.* 20 L30
[63] S. J. Ye, A. Matsumoto, K. Togano and H. Kumakura 2011 *Physica C* 471 1133
[64] S. J. Ye, M. Song, A. Matsumoto, K. Togano, M. Takeguchi, H. Kumakura, R. Teranishi and T. Kiyoshi 2011 *Physica C* 484 167
[65] Ye S J, Song M, Matsumoto A, Togano K, Zhang Y, Kumakura H, Takeguchi M, Teranishi R and Kiyoshi T 2012 *Supercond. Sci. Technol.* 25 125014
[66] Ye S J, Matsumoto A, Togano K, Zhang Y, Ohmura T and Kumakura H 2013 *Supercond. Sci. Technol.* Submitted
[67] Ye S J, Matsumoto A, Togano K, Ohmura T and Kumakura H 2013 *Supercond. Sci. Technol.* 26 105027
[68] Li G Z, Sumption M D, Susner M A, Yang Y, Reddy K M, Rindfleisch M A, Tomsic M J, Thong C J and Collings E W 2012 *Supercond. Sci. Technol.* 25 115023
[69] Ye S J, Matsumoto A, Togano K, Zhang Y, Kumakura H, Song M, Teranishi R and Kiyoshi T 2012 *prestention of ASC2012* 1MB-01
[70] Ye S J, Song M, Matsumoto A, Togano K, Takeguchi M, Ohmura T and Kumakura H 2013 *Supercond. Sci. Technol*. 26 125003
[71] Li G Z, Sumption M D, Zwayer J B, Susner M A, Rindfleisch M A, Thong C J, Tomsic M J and Collings E W 2013 *Supercond. Sci. Technol*. 26 095007
[72] Susner M A, Yang Y, Sumption M D, Collings E W, Rindfleisch M A, Tomsic M J and Marzik J V 2011 *Supercond. Sci. Technol.* 24 012001
[73] Ye *et al*. Preparation

Chapter 2 Development of a new method combining IMD and PIT processes for MgB_2 wires

2.1 Introduction

As introduced in chapter 1, we found that the un-reacted B particles exist in the MgB_2 layer which decreases the J_c properties. The un-reacted B particles are considered to be caused by an insufficient reaction between Mg and B layer due to the long diffusion distance of Mg atoms. These un-reacted B particles are non-superconducting phase, hence, decrease the J_c properties. Here, I explored a new approach - Mg powder addition to the B layer of IMD-processed MgB_2 wires in order to reduce the un-reacted B particles by decreasing the average Mg diffusion distance. Our results showed that this is an effective method to decrease the un-reacted B particles [1]. But it also produced the voids in the MgB_2 layer which is caused by the volume shrink as in the case of PIT process.

If I continue to increase the amount of Mg powder addition to the B layer, the Mg rod diameter should simultaneously be decreased to balance the ratio of Mg and B (1 : 2) to form MgB_2. In the case of 50 mol% Mg powder addition (stoichiometric composition), the diameter of the Mg rod needs to be decreased to 0, which means the IMD process (schematically shown in Fig. 2-1 (a)) changes to the PIT process (schematically shown in Fig. 2-1 (b)). The process with Mg powder addition lower than 50 mol% Mg is in fact a combination of IMD and PIT processes [2] (Schematically shown in Fig. 2-1 (c)).

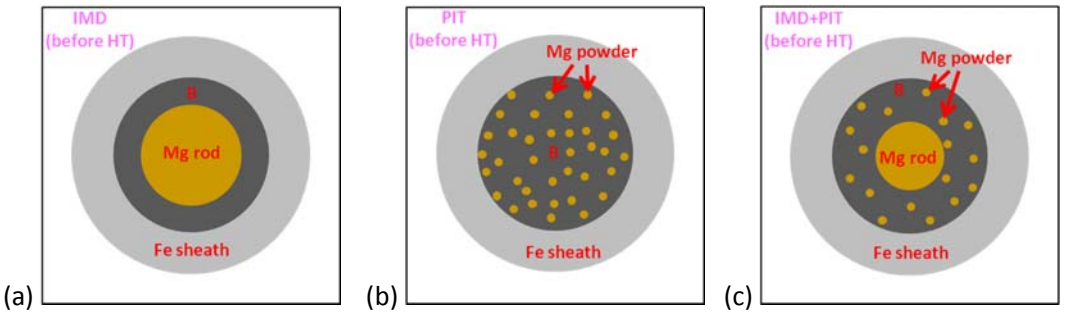

Fig. 2-1 Schematic maps of the transverse cross sections for MgB_2 wires fabricated with (a) IMD, (b) PIT, and (c) a new method combining IMD and PIT

In this chapter, I will introduce this new method of hybridization of IMD and PIT processes for MgB_2 wires by two steps: Firstly, small amounts of Mg powder is added to B layer of IMD-processed MgB_2 wires without the change of Mg rod diameter, and secondly, Mg powder addition to B layer of IMD-processed MgB_2 wires is increased and Mg rod diameter is decreased. The first step focuses on the IMD process with Mg powder addition. The second step mainly introduces a new method which is a hybrid method of IMD and PIT processes. The details for this chapter are described in my previous paper [1, 2].

2.2 Enhancement of critical current properties of IMD-processed MgB_2 wires by Mg addition

2.2.1 Experimental details

An Mg rod (diameter: 2.0 mm) was polished with abrasive paper to remove the oxide and then put into the center of an Fe tube (inner diameter 3.5 mm, outer diameter 6.0 mm). A mixture of amorphous B powder (99%, 325-mesh) and Mg powder (99.8%, 325-mesh) prepared by grinding in an agate mortar was packed into the space between the Mg rod and the Fe tube. The concentration of the Mg in the mixture was varied as 0 mol%, 3 mol%, 6 mol%, 9 mol% and 12 mol%. The composite billet was then cold worked (by groove rolling, swaging, and drawing) to a wire with a diameter of 1.16 mm. After the cold working, short samples of 40 mm length were cut from the wire and subjected to heat treatment. We also prepared wires in which nano-sized SiC powder was added together with the Mg powder to B powder, with the fixed (10 mol%) concentration of SiC. Undoped PIT-processed mono-core wire from the same B and Mg powders with diameter of 1.0 mm was fabricated for comparison. The specifications of wires fabricated in this study are listed in table 2-1.

Table 2-1. The specifications of all MgB_2 wires

No	Sample	Doped SiC (mol%)	Doped Mg powder (Mg/(Mg+B), mol%)	Diameter (mm)	Slope of J_c-B curve (1/T)
A1	Pure, IMD	0	0	1.16	-0.358
A2	3 mol% Mg, IMD	0	3	1.16	-0.337
A3	6 mol% Mg, IMD	0	6	1.16	-0.345
A4	9 mol% Mg, IMD	0	9	1.16	-0.346
A5	12 mol% Mg, IMD	0	12	1.16	-0.328
B	pure, PIT	0	33.3	1.0	-0.364
C1	10 mol% SiC, IMD	10	0	1.16	-0.204
C2	10 mol% SiC + 3 mol% Mg, IMD	10	3	1.16	-0.203
C3	10 mol% SiC + 6 mol% Mg, IMD	10	6	1.16	-0.199
C4	10 mol% SiC + 9 mol% Mg, IMD	10	9	1.16	-0.201

All samples (40 mm length) with no seal at the ends were wrapped with Zr foils and were heated in a furnace as the following process: We first raised the temperature from room temperature to 640 °C in 1 hour, then raised it gradually to 670 °C in 3 hours, held this temperature for 2 hours, and finally cooled the specimens to room temperature in the furnace. This slow raising temperature from 640 °C (lower than Mg melting point, 650 °C) was applied to make the Mg diffuse into B layer rather than vaporize. The heat treatment was carried out in an Ar gas atmosphere (1 atm).

The transport critical current (I_c) of the wires was measured using the four-point resistive method. The J_c was calculated for the cross-sectional area of the reacted layer. While the J_e for the cross-sectional area of the whole wire was also calculated. The cross section of the wire was observed using optical microscopes (KEYENCE VK-8500 for low magnification, while OLYMPUS BX60M for high magnification). Scanning electron microscopy (SEM) and transmission electron microscopy (TEM) were carried out with the Hitachi SU-70 and JEM-2100F, respectively. The sample for TEM was a film with a thickness of 100 nm which was taken from the transverse cross section of a wire and thinned using a focused ion beam (JEOL JEM-FIB9320). STEM dark field (STEM-DF) observations were carried out with a camera length of 20 cm and a collection angle ranging from 70 to 184 mrad.

2.2.2 Results and discussion

Fig. 2-2(a) and (b) show the J_c-B curves and J_e-B curves at 4.2 K for the IMD-processed MgB_2 wires, respectively. Undoped and Mg-added wires are compared. We only measured I_c in fields higher than 6 T because I_c below 6 T was sufficiently high to quench and deteriorates the wires due to the resulting increase in temperature. The value of J_c increased with increasing Mg concentration, with a maximum value at 6 mol% Mg addition; J_c then decreased for higher Mg concentrations. The slopes of J_c-B curves in Fig. 2-2(a) defined with the field range of 10-12 T were shown in table 2-1. All the wires showed almost the same slopes indicating that the magnetic field dependence of J_c was not changed. We ascribe the reduction of J_c at Mg concentrations over 6% to the volume shrinkage (leading to porosity) caused by the reaction between the Mg powder and the B powder, which is well known in the PIT process. The J_c of the 6 mol% Mg-added MgB_2 wire was about twice as high as that of the undoped wire, and is about 1.2 x 10^4 A/cm^2 in 4.2 K and 10 T. J_e shows similar behavior to J_c. Both J_c and J_e values show that the addition of Mg powder to B layer is an effective method to decrease the un-reacted B particles in IMD MgB_2 layer, and thus enhances critical current properties of IMD-processed MgB_2 wires.

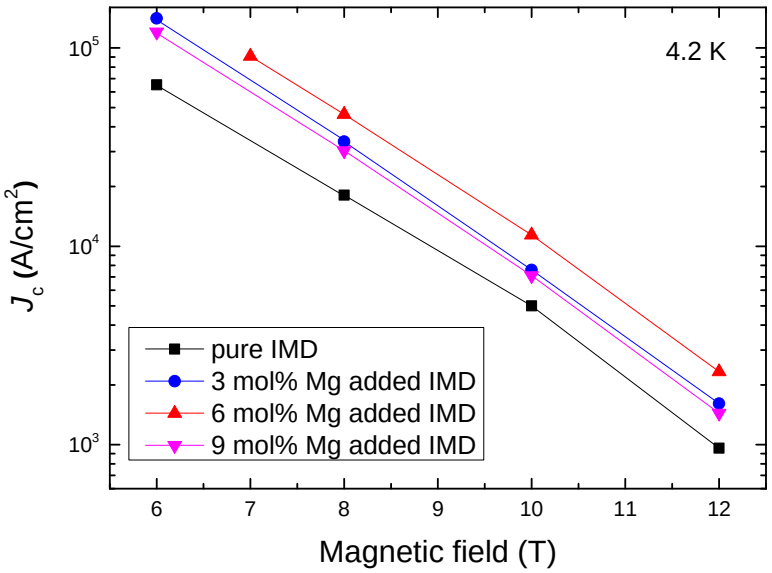

(a)

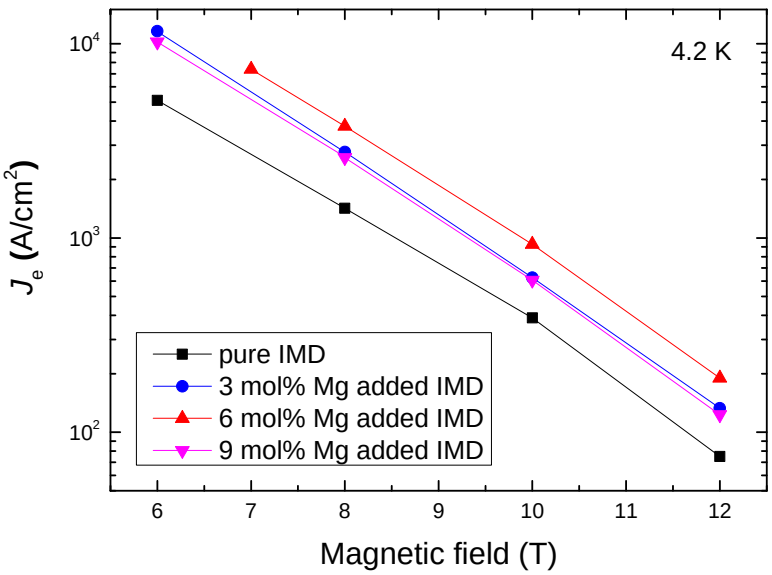

(b)

Fig. 2-2 (a) J_c-B curves and (b) J_e-B curves of IMD-processed undoped and Mg-added MgB_2 wires

Fig. 2-3(a) and (b) show magnified optical microscope images of transverse cross section of undoped and 6 mol% Mg-added IMD-processed MgB_2 wires, respectively. Our previous results [3-5] indicated that the main phase of the reacted layer (yellow domain) is MgB_2, and the blue particles in the reacted layer are the un-reacted B particles. The black spots found in the Fe tube and reacted layer correspond to resins from the polishing process. Compared to the case of the undoped IMD wire shown in Fig. 2-3(a), the presence of unreacted particles decreased in the 6 mol% Mg-added wire as shown in Fig. 2-3(b). A high density of un-reacted B particles was observed at an area far from the hole in Fig. 2-3(a), which can be explained by the long Mg diffusion distance from the center of the wire. This result is consistent with the results of Shimada *et al*. [6]. Un-reacted B particles in the Mg-added wires in Fig. 2-3(b) can be explained by the fact that the starting B powders contained some large particles and these were not easily crushed using a mortar in our lab.

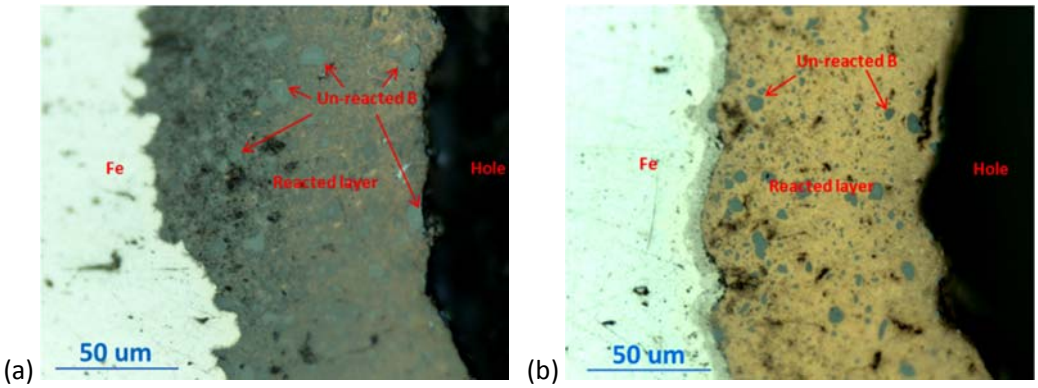

Fig. 2-3 Magnified optical microscope images of transverse cross-section of IMD-processed (a) undoped and (b) 6 mol% Mg-added MgB_2 wires

Fig. 2-4(a) and (b) show SEM images of longitudinal cross section of undoped and 6 mol% Mg-added IMD-processed MgB_2 wires, respectively. The 6 mol% Mg-added wire has smaller size and less amounts of un-reacted B particles than that of undoped wire in longitudinal cross-section, which is consistent with the transverse cross-section shown in Fig. 2-3(a) and (b). Some voids can also be found in the 6 mol% Mg-added IMD-processed MgB_2 wires, which was due to the volume shrinkage when added Mg powder reacted with B. These voids increase as the Mg powder addition increases.

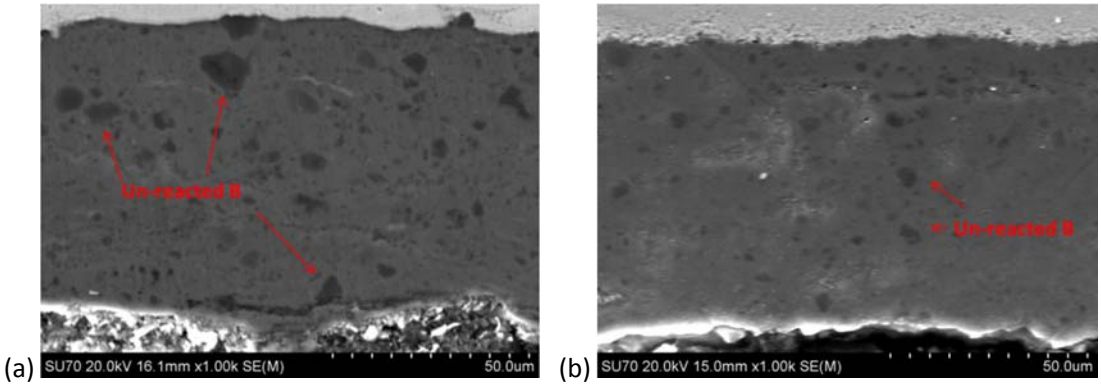

Fig. 2-4 SEM images of longitudinal cross-section of IMD-processed (a) undoped and (b) 6 mol% Mg-added MgB_2 wires

The samples for TEM observations were taken from the transverse cross section of the wires where no un-reacted B layer was found by optical microscopy (yellow domain in Fig. 2-3(a) and (b)).

Fig. 2-5(a) shows a STEM-DF image of undoped samples prepared by the FIB. Fig. 2-5(b) shows a magnified STEM-DF image of the red frame in Fig. 2-5(a). There are two kinds of regions in Fig. 2-5(b), marked (A) and (B). Fig. 2-5(c) and (d) show the high resolution images of the (A) and (B) regions, respectively. Our previous research [7] showed that the region A is polycrystalline, consisting mainly of MgB_2 and MgO for the undoped wires, and MgB_2, MgO and Mg_2Si for the SiC-added wires. The fast Fourier transform (FFT) observed from the region of red frame in Fig. 2-5(c) shows that the crystal is MgB_2 grain, observed in [011] direction. Region B is the amorphous phase as shown in Fig. 2-5(d) and corresponds to un-reacted B particles for both undoped and SiC-added wires.

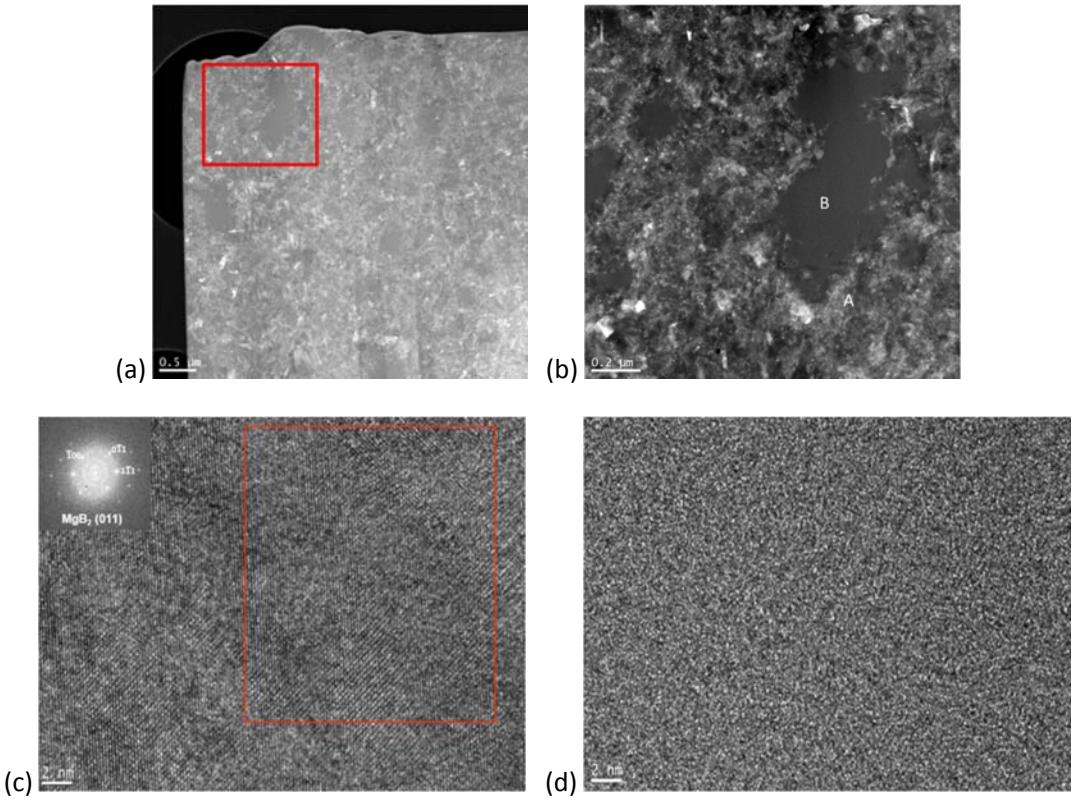

Fig. 2-5 (a) STEM dark field (DF) image of the reacted layer in undoped MgB_2 wire. (b) Magnified STEM-DF image of the red frame in Fig 2-4(a). (c) High resolution image of region (A) in Fig 2-4(b). (d) High resolution image of region (B) in Fig 2-4(b)

Fig. 2-6 shows a STEM-DF image of the 6 mol% Mg-added wire. Compared to the undoped wires shown in Fig. 2-5(a), there are no large amorphous regions in the Mg-added wires. As mentioned above, these samples were taken from the wires wherein un-reacted B particles could not be observed in the optical microscope. This indicates that Mg powder addition decreased the amount of un-reacted B particles even in TEM level. This is in contrast to the case of undoped wire shown in Fig. 2-5(a). Thus, the decrease in the Mg diffusion distance of IMD-processed MgB_2 wires by the Mg powder addition was effective in reducing the amount of un-reacted B particles. This decrease in the quantity of un-reacted B particles is likely responsible for the J_c enhancement seen in Fig. 2-2.

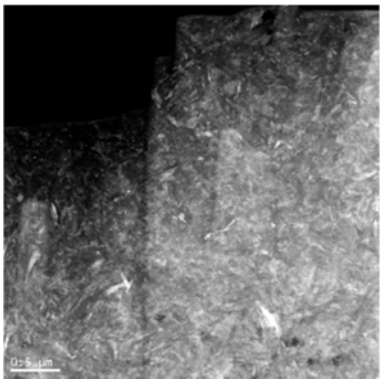

Fig. 2-6 STEM-DF image of 6 mol% Mg-added IMD-processed MgB_2 wire

The concentration of the Mg powder in the starting powders (mixture of Mg and B powders) of the PIT-processed MgB_2 is ~33 mol%. Fig. 2-7 shows the J_c value at 4.2 K and 10 T as a function of the Mg concentration in the B powders. J_c increases with increasing Mg concentration due to the decrease in the amount of un-reacted B particles, while J_c decreased above 6 mol% Mg concentration since the porosity in the reacted layer increased with increasing Mg concentration. Although the J_c started to decrease slowly at the range of 9 ~ 12 mol% Mg addition, we speculate that J_c will monotonically decrease if we increase the Mg concentration above 12 mol% and correspondingly decrease the diameter of the Mg rod at the center of the wire. Finally, at 33 mol% Mg concentration with no Mg rod present, the wire becomes a PIT-processed wire and we obtained low J_c value of about 1.6 x 10^3 A/cm^2 at 4.2 K and 10 T.

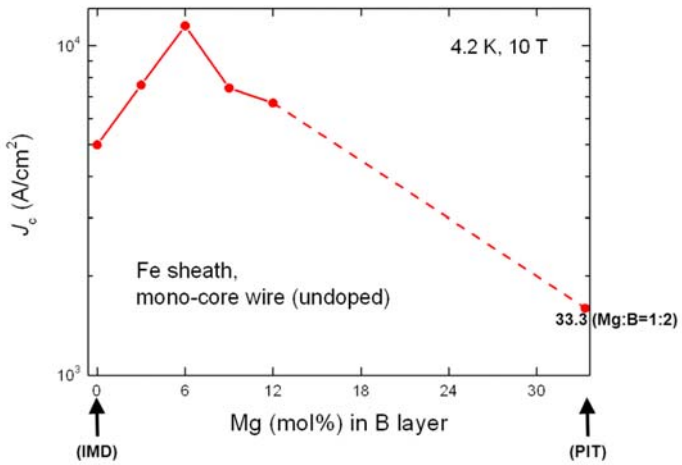

Fig. 2-7 J_c values at 4.2 K and 10 T as a function of Mg concentration of IMD-processed MgB_2 wires

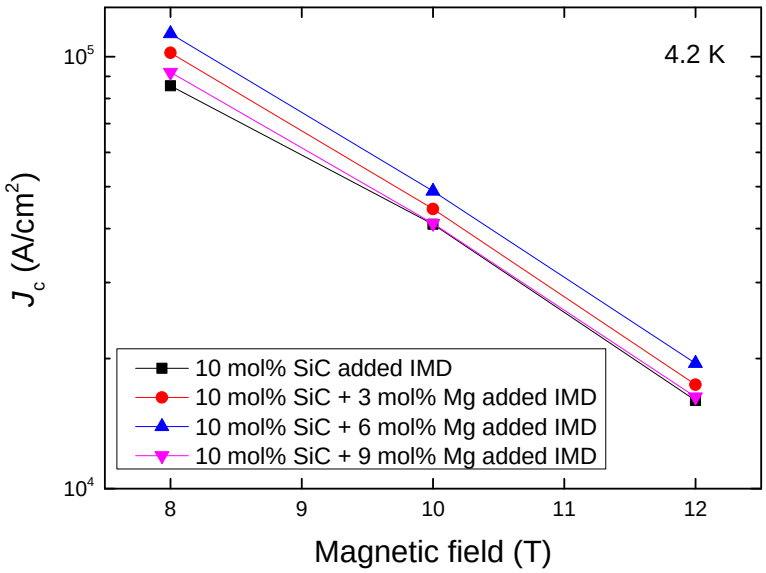

(a)

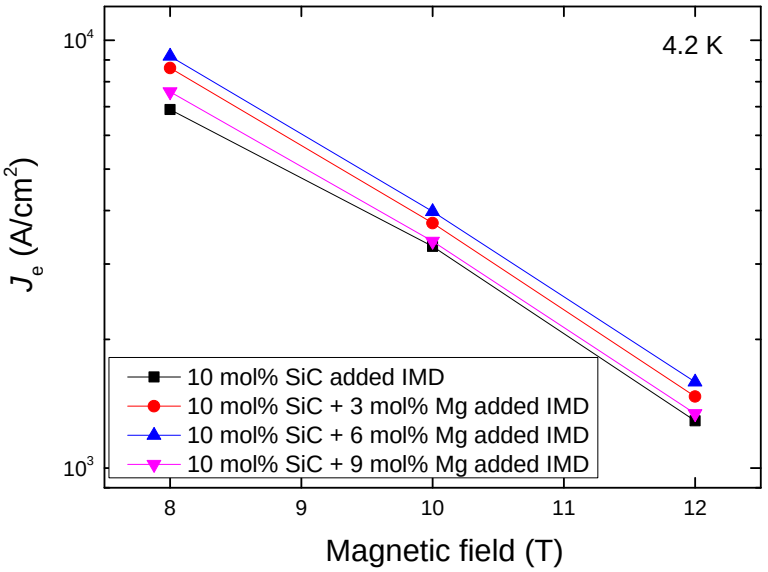

(b)

Fig. 2-8 (a) J_c-B and (b) J_e-B curves of the IMD-processed MgB_2 wires with 10 mol% SiC addition and 10 mol% SiC and Mg powder (3, 6, and 9 mol%) co-addition

Fig. 2-8(a) and (b) show the J_c-B curve and J_e-B curve at 4.2 K for IMD-processed MgB_2 wires with 10 mol% SiC addition and 10 mol% SiC and Mg (of 3 mol%, 6 mol% and 9 mol%) co-addition, respectively. We only measured I_c in fields higher than 8 T because I_c below 8 T for all the wires is sufficiently high to quench and deteriorates the wires. The slopes of J_c-B curves in Fig. 2-7(a) were shown in table 2-1. All the slopes (absolute value) of the J_c-B curves for SiC added wires are smaller than those of the wires with no SiC addition in Fig. 2-2 due to the C-substitution at the B sites. The slopes of the J_c-B curves in Fig. 2-8(a) and (b) are all nearly the same, indicating that Mg addition did not further change the magnetic field dependence of J_c. Here, 6 mol% Mg powder and 10 mol% SiC co-added wire has the highest J_c and J_e values. While 6 mol% Mg powder added wire also shows the highest J_c and J_e values for wires without SiC addition. This suggests that the mechanism of J_c enhancement by the Mg powder addition is the same for both undoped and SiC-added wires. J_c for the 10 mol% SiC and 6 mol% Mg co-added wires was 1.2 times higher than that of only SiC-added wires in all measured magnetic fields. This J_c increase is smaller than that for the wires with no SiC-added. The highest J_c obtained in this experiments is about 5 x 10^4 A/cm^2 at 4.2 K and 10 T, which is almost same with the high J_c value we obtained using high quality B powder with SiC and toluene co-addition [8, 9].

Fig. 2-9 (a) and (b) show STEM-DF images of 10 mol% SiC-added wires and 10 mol% SiC and 6 mol% Mg co-added wires, respectively. SiC-added wires have un-reacted B particles marked as B, while there are less (almost no) un-reacted B particles in the co-added wire. This result is similar to that for the undoped wires and Mg-added wires, suggesting that Mg addition is an effective way to reduce the amount of un-reacted B particles and enhance J_c in impurity-added IMD-processed MgB_2 wires.

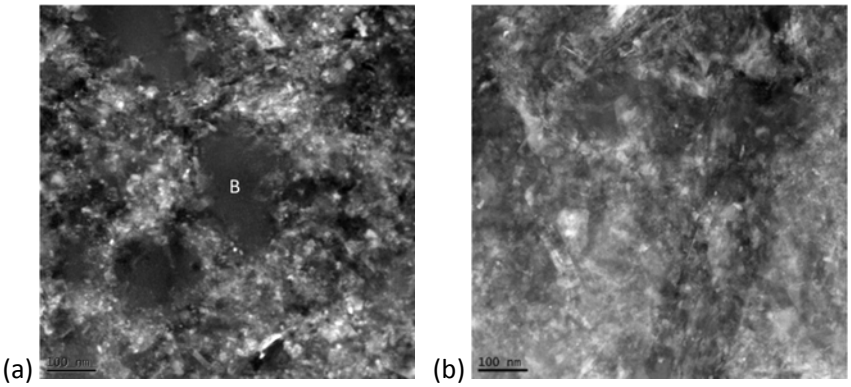

Fig. 2-9 STEM-DF images of (a) 10 mol% SiC-added (b) 10 mol% SiC and 6 mol% Mg powder co-added IMD-processed MgB_2 wires

2.3 Fabrication of MgB_2 wires with a new method combining IMD and PIT processes

As introduced in 2.1, if we continue to increase the Mg powder addition to IMD-processed MgB_2 wires, we should decrease the Mg rod diameter to make a balance between Mg and B. This is a new method– a combination of IMD and PIT processes for MgB_2 wires. In this section, I will discuss this new method for the fabrication of MgB_2 wires.

2.3.1 Experimental details

A 2 mm diameter Mg rod was polished with abrasive paper to remove surface oxide and then put into the center of a Fe tube with a 6 mm outer diameter. A mixture of amorphous B powder (99 %, 325-mesh, Alfa Aesar), Mg powder (99.8%, 325-mesh, Alfa Aesar) and nano-sized SiC were prepared by grinding in an agate mortar which was packed into the space between the Mg rod and the Fe tube. The composite billet was then cold worked (by groove rolling and drawing) to a wire with a diameter as shown in table 2-2. Details of the MgB_2 wire fabrication were described in our previous paper [1-5, 7-8]. The concentration of SiC to B powder was 10 mol% for all wires. Three wires were fabricated with the mixing process of IMD and PIT and were named M1, M2, and M3, respectively. The amount of Mg powders added into the B layer were 6 mol%, 17 mol%, and 25 mol% for the three wires. The Mg rod diameters were 2 mm, 1.7 mm, and 1.4 mm, and the Fe tube inner diameters were 3.5 mm, 4.0 mm, and 4.0 mm to keep the ratio of Mg to B the same as the IMD-processed MgB_2 wire. IMD-processed MgB_2 wires termed M0 and PIT-processed MgB_2 wires termed P0 were also fabricated. The specifications of all these wires are listed in table 2-2. The heat treatment process for IMD-processed MgB_2 wires (4 cm length) is described in (2.2.1).

Table 2-2. Details of the fabricated wires

No.	M0	M1	M2	M3	P0
State	IMD	IMD+PIT	IMD+PIT	IMD+PIT	PIT
Wire diameter (mm)	1.16	1.16	1.2	1.26	1.0
Mg rod (mm)	2	2	1.7	1.4	0
Mg rod area (mm^2)	1π	1π	0.72π	0.49π	0
Fe inner diameter (mm)	3.5	3.5	4	4	3.5
Mg powder concentration (Mg : B, mol%)	0	6%	17%	25%	50%
MgB_2 area fraction (%)	8%	8.1%	21.4%	23.8%	25.3%

A 10 mol% SiC-added PIT mono-core wire with a diameter of 1.0 mm was fabricated from the same B and Mg powders for comparison. This PIT wires (4 cm length) were heated as follows: The temperature was raised to 850 °C for 1 hour, held for 1 hour, and then cooled down in the furnace. We used a higher heat treatment temperature than that for the IMD process because it can yield higher critical current properties for PIT MgB_2 wires fabricated with the same starting materials.

Scanning electron microscopy (SEM) observations and energy dispersive X-ray spectrometry (EDS) mapping were carried out using a Hitachi SU-70 instrument. The cross-sectional area of the reacted layer was observed using an optical microscope (OM, KEYENCE VK-8500). The transport critical current (I_c) of the wires was measured using the four-probe resistive method. J_c was calculated for the cross-sectional area of the reacted MgB_2 layer, while J_e was calculated for the cross-sectional area of the whole wire.

2.3.2 Results and discussion

Fig. 2-10(a) shows an optical microscope image on the transverse cross section of M0, which is the representative image for the IMD-processed MgB_2 wire. The MgB_2 layer is orange in color, due to the high density MgB_2 layer reflecting light, which is consistent with the MgB_2 crystal reported by Lee *et al*. [9]. Fig. 2-10(b) shows an image of P0, which is the representative image for the PIT-processed MgB_2 wire. The MgB_2 layer is dark, which is due to the large amount of voids in the PIT-processed MgB_2 layer absorbing light. Fig. 2-10(c) shows an image of M2. The color in the reacted MgB_2 layer is uniform, which indicates that the reaction is completed (no B-rich region) although the MgB_2 thickness is large (almost 140 μm). As listed in table 2-2, the MgB_2 area fraction for M2 and M3 are 21.4% and 23.8%, respectively. The reacted MgB_2 area fraction of MgB_2 wires fabricated by the mixing processes of IMD and PIT is close to that of the PIT-processed MgB_2 wire (P0), 25.3%. These results suggest that the new method combining IMD and PIT can increase MgB_2 layer thickness and hence yield higher MgB_2 area fraction compared to IMD MgB_2 wires.

(a) 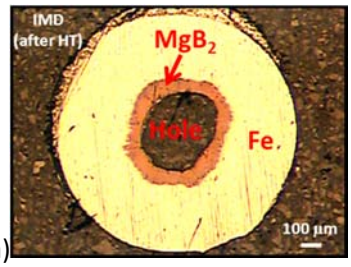

(b) 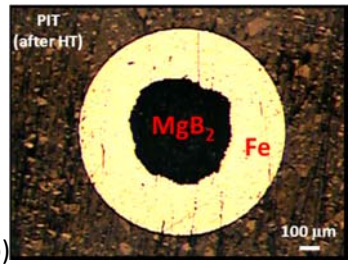

(c) 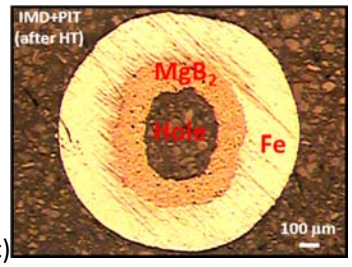

Fig. 2-10 OM images on the transverse cross sections of (a) IMD-processed wire (M0), (b) PIT-processed wire (P0), and (c) the wire fabricated with new method combining IMD and PIT (M2)(Specification of the samples M0 to P0 are listed in table 2-2)

Fig. 2-11(a) and Fig. 2-11(b) show SEM images of the transverse and longitudinal cross sections of M2, respectively. A uniform MgB_2 layer was observed along the Fe sheath and a hole was found in the center of the wire. This result suggests that the mixing process of IMD and PIT can be applied to fabricate large-scale wires for practical applications. Some voids can be found in both transverse and longitudinal cross sections, which are produced by the volume shrinkage caused by the reaction between B powder and Mg powder as in the case of the PIT process. The voids have an ellipsoidal shape only in the longitudinal cross section, which is due to the elongation of Mg powder during the wire fabrication (groove-rolling and drawing) process.

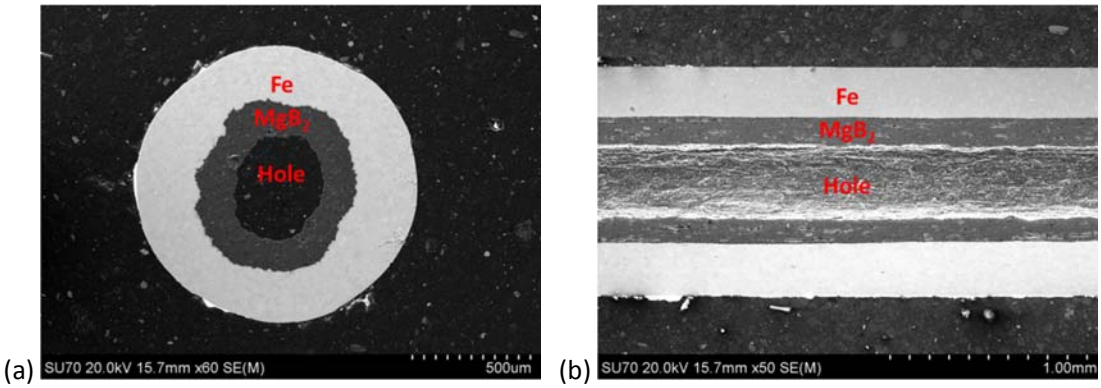

Fig. 2-11 SEM images of the (a) transverse and (b) longitudinal cross sections of the M2 MgB_2 wires (Specification of the samples M0 to P0 are listed in table 2-2)

Fig. 2-12 shows SEM images of the longitudinal cross sections of MgB_2 wires of (a) M0, (b) M1, (c) M2, (d) M3, and (e) P0. The amount and size of the un-reacted B particles (dark areas) decreased and the voids in the MgB_2 layer were increased with increasing Mg powder addition, from Fig. 2-12(a) to (e). In Fig. 2-12(b), the observed small amount of voids looks like bright lines, due to the small amount of Mg powder addition. In Fig. 2-12(c) and (d), a large amount of voids with ellipsoidal shape in the longitudinal direction can be observed. M3 (Fig. 2-12(d)) shows granular MgB_2 similar to P0 (Fig. 2-12(e)). This is due to the large amount (25 mol%) of Mg powder addition to the B layer, which is a half of the amount of Mg powder of P0 (50 mol%). The added Mg powders in the B layer first react with B powders during the temperature-increase process and MgB_2 is formed resulting in shrinkage (voids). This first reaction produces voids near the formed Mg-B compound in the B layer, which is useful for the following Mg diffusion, thus improving the reaction between Mg and B. This is considered to be another mechanism of decreasing un-reacted B by Mg addition. Furthermore, B-rich regions existing far from the Mg rod, which can usually be found in IMD-processed MgB_2 wires [4, 5] even when the nano-sized B powders are used [10, 11], could also be decreased by this mixing process of IMD and PIT. Thus, we obtained a large thickness (almost 140 μm) MgB_2 layer without B-rich particles in this study.

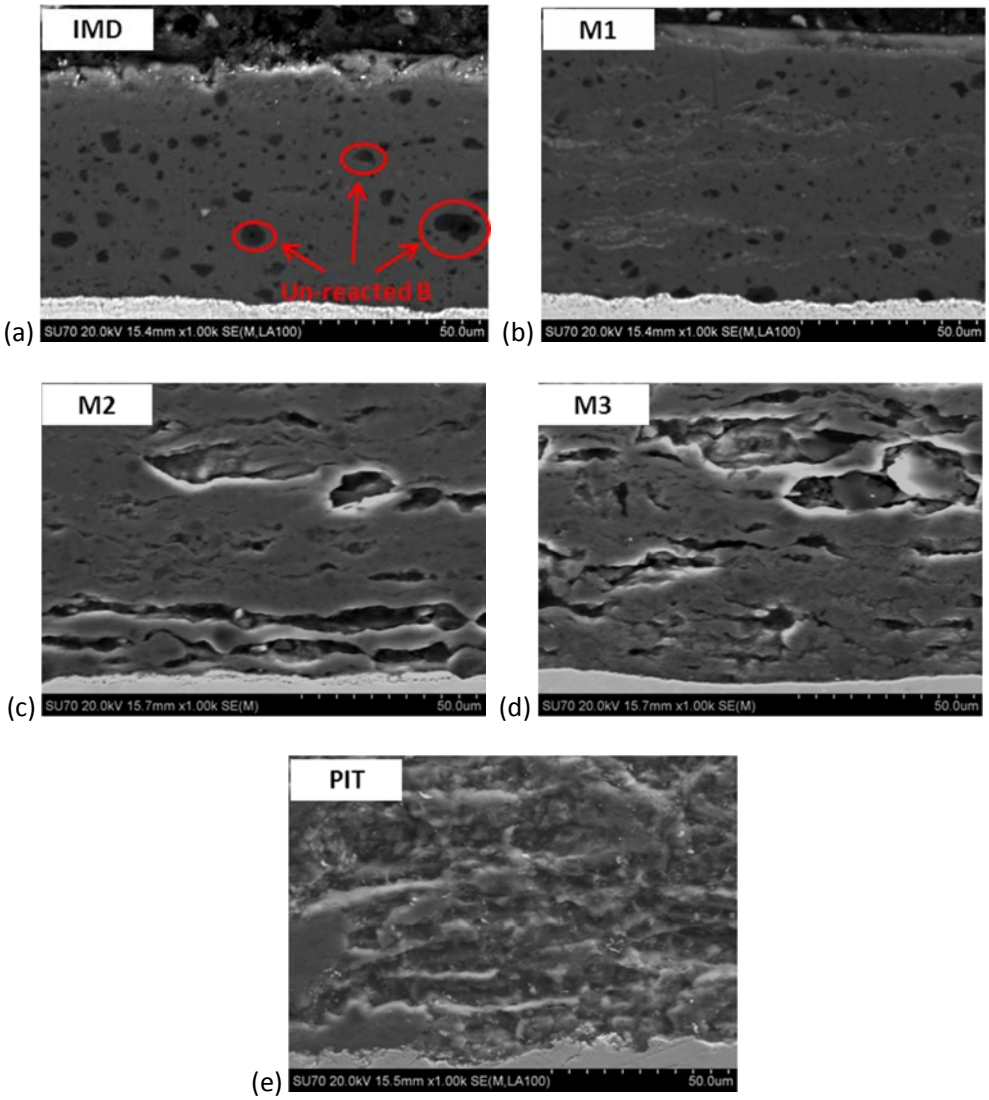

Fig. 2-12 SEM images of the longitudinal cross sections of the MgB_2 wires, (a) M0, (b) M1, (c) M2, (d) M3, and (e) P0. All images were obtained after heat treatment (Specification of the samples M0 to P0 are listed in table 2-2)

Fig. 2-13(a) and (b) show J_c-B and J_e-B curves at 4.2 K for MgB_2 wires of (a) M0, (b) M1, (c) M2, (d) M3, and (e) P0, respectively. We found that the maximum J_c (4.9 x 10^4 A/cm^2 at 4.2 K and 10 T, with M1) and J_e (5.8 x 10^3 A/cm^2 at 4.2 K and 10 T, with M2) values are both obtained by the new method combining IMD and PIT. All the J_c-B curves show almost the same slopes due to the similar carbon substitution for boron by the same 10 mol% SiC addition. The change in J_c values is consistent with the change in microstructure observed by SEM, as shown in Fig. 2-12. With increasing Mg powder addition, the decrease of un-reacted B particles enhances J_c, while the

increase of voids decreases J_c. The PIT-processed MgB_2 wire (P0) shows the lowest J_c (7.5 x 10^3 A/cm^2 at 4.2 K and 10 T) due to the largest amount of voids present in it.

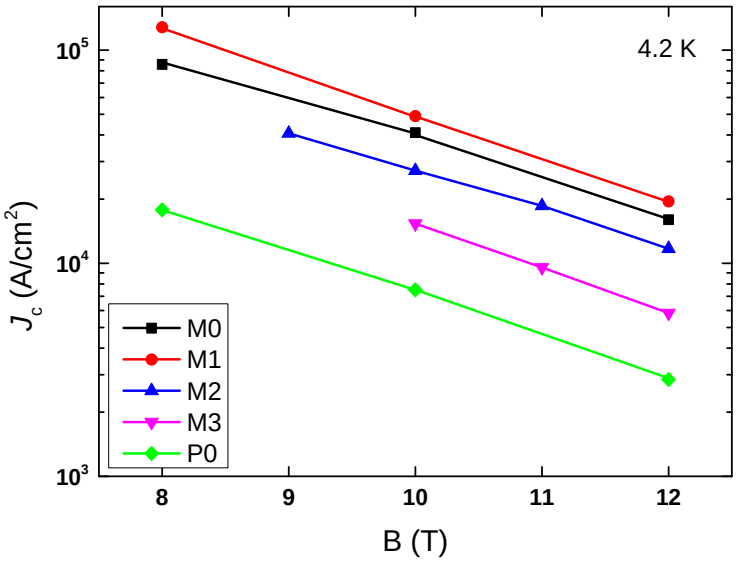

(a)

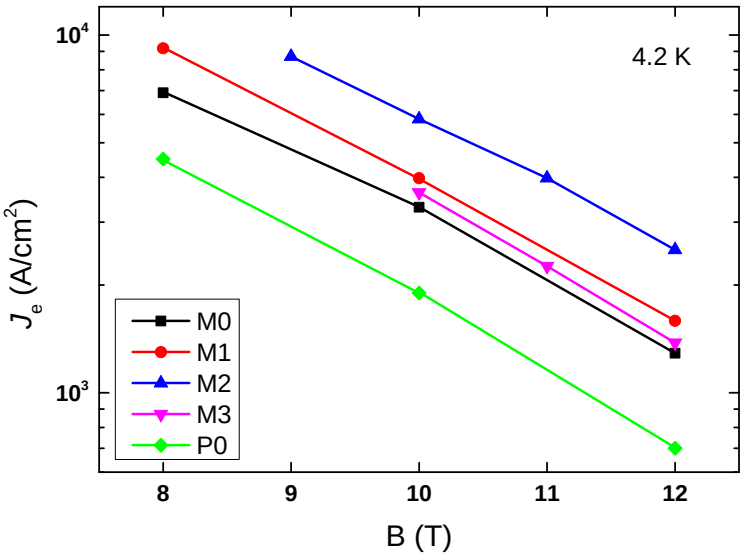

(b)

Fig. 2-13 (a) J_c-B and (b) J_e-B curves at 4.2 K for the MgB_2 wires fabricated in this study (Specification of the samples M0 to P0 are listed in table 2-2)

The J_c and J_e values at 10 T and 4.2 K are compared in Fig. 2-14. As mentioned above, J_c first increases and then decreases with increasing Mg powder concentration. J_e also shows a similar trend but the maximum J_e is obtained at a higher Mg concentration than the maximum J_c. With increasing Mg powder addition, the MgB_2 area fraction increased due to the increase in B layer thickness and the decrease in Mg rod diameter, leading to a higher J_e value. Furthermore, the enhancement of J_e by the Mg powder addition is much larger than that of J_c, which can also be explained by the increase in MgB_2 area fraction. Because J_e values are a much more important parameter than J_c values for practical applications, this new method is advantageous from the viewpoint of practical applications. We have not yet optimized parameters of this new method such as the amount of Mg powder addition, Mg rod size, sheath material and amount of B powder. Thus, the maximum J_c and J_e values can be further enhanced by optimizing these parameters.

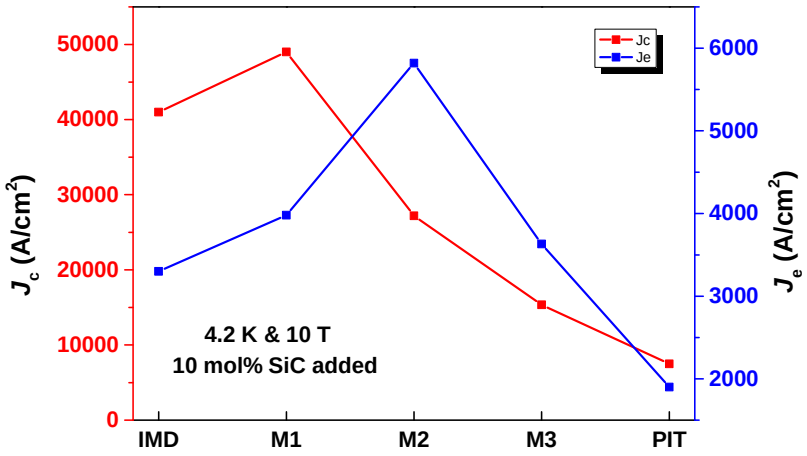

Fig. 2-14 J_c and J_e values at 4.2 K and 10 T as a function of added Mg concentration, i.e. IMD, M1-M3, PIT (Specification of the samples M0 to P0 are listed in table 2-2)

2.4 Conclusions

In order to decrease the amount of un-reacted B particles in the IMD-processed MgB_2 wires, we added Mg powder to the B powder layer to reduce the Mg diffusion distance. J_c increased for Mg concentration below 6 mol% and decreased above 6 mol% Mg addition for both undoped and 10 mol% SiC-added IMD-processed MgB_2 wires. The enhancement of J_c is due to the decrease of un-reacted B particles while the decrease of J_c above 6 mol% Mg addition is due to the increase of porosity caused by the volume shrinkage resulting from the reaction between the Mg and B powders as in the case of PIT process.

A new hybrid method of IMD and PIT processes for fabrication of MgB_2 wires was developed. This new method is that: Mg powder is added to the B layer of the IMD-processed MgB_2 wires and the Mg rod diameter is decreased simultaneously to balance the ratio of Mg to B. J_c and J_e of this method are governed by factors including: the amount of un-reacted B, voids in the MgB_2 layer, and MgB_2 area fraction. In this study, the maximum J_c of 4.9 x 10^4 A/cm^2 at 10 T and 4.2 K was obtained for M1 (6 mol% Mg addition), while the maximum J_e of 5.8 x 10^3 A/cm^2 was obtained for M2 (17 mol% Mg addition). The enhancement of J_e by this process is much larger than that of J_c. This is because both the addition of Mg powder and decrease in Mg rod diameter enable the increase in MgB_2 layer thickness and, hence, the MgB_2 area fraction is increased. The J_c and J_e values obtained in this study are not as high as in our previously reported data because I used low quality B powder in the present experiments. The use of high quality B powder is expected to increase J_c and J_e of the MgB_2 wires fabricated by this new method. Furthermore, this process is expected to improve other properties (such mechanical properties, electrical magnetic properties) of IMD- and PIT-processed MgB_2 wires.

Above all, the new method of combination of IMD and PIT developed in this chapter is expected to fabricate high performance MgB_2 wires for practical applications.

In addition, enhancement of J_e is the technical problem, which will mainly be studied in the fabrication of products. Enhancement of physic properties, J_c are the main work for my Ph.D thesis. Thus the following chapter will not introduce new method developed in this chapter due to the new method increase J_c which is dependent of B powder we used.

References

[1] Ye S J, Song M, Matsumoto A, Togano K, Zhang Y, Kumakura H, Takeguchi M, Teranishi R and Kiyoshi T 2012 Supercond. Sci. Technol. 25 125014
[2] Ye *et al*, submittd
[3] Hur J H, Togano K, Matsumoto A, Kumakura H, Wada H and Kimura K 2008 Supercond. Sci. Technol. 21 032001
[4] Togano K, Hur J, Matsumoto A and Kumakura H 2010 Supercond. Sci. Technol. 23 085002
[5] Kumakura H, Hur J, Togano K, Matsumoto A, Wada H and Kimura K 2011 IEEE Transactions on Applied Superconductivity 21 2463
[6] Shimada Y, Kubota Y, Hata S, Ikeda K, Nakashima H, Matsumoto A, Togano K and Kumakura H 2011 Physica C 471 1137
[7] Song M, Ye S J, Takeguchi M, Matsumoto A, Togano K, Kumakura H, Teranishi R and Kiyoshi T 2012 Conference Proceedings APMC 10 (10th Asia-Pacific Microscopy Conference)/ICONN 2012/ACMM 22 699 (1–2)
[8] Nishijima G, Ye S J, Matsumoto A, Togano K, Kumakura H, Kitaguchi H and Oguro H 2012 Supercond. Sci. Technol. 25 054012
[9] Lee S, Masui T, Yamamoto A, Uchiyama H and Tajima S 2003 Physica C 412 31
[10] Li G Z, Sumption M D, Susner M A, Yang Y, Reddy K M, Rindfleisch M A, Tomsic M J, Thong C J and Collings E W 2012 Supercond. Sci. Technol. 25 115023
[11] Li G Z, Sumption M D, Zwayer J B, Susner M A, Rindfleisch M A, Thong C J, Tomsic M J and Collings E W 2013 Supercond. Sci. Technol. 26 095007

Chapter 3 Fabrication of 37-filamentary IMD-processed MgB_2 wires

3.1 Introduction

As we know, the superconducting wires used for practical applications must be multi-filamentary wires for stability. The 37-filamentary MgB_2 wires for PIT process had been fabricated [1, 2]. But for IMD-process, 19 is the maximum filament number reported so far [3-6]. The fabrication of multi-filamentary IMD wire seems difficult because the Mg rod is not easily to cold-worked. This chapter describes the fabrication of 37-filamentary IMD-processed MgB_2 wires [7]. The critical current properties and microstructures of these wires were investigated.

3.2 Experimental details

An Mg rod (diameter: 2 mm) was placed into the center of a Ta tube (inner diameter: 3.5 mm, outer diameter: 6 mm). The oxide at the surface of the Mg rod was removed by an abrasive paper. The B powder (325-mesh, 99%) was packed into the space between the Ta tube and the Mg rod for the undoped wires, and a mixture of B powder and 10 mol% nano-sized SiC powder was used for the SiC-added wires. The composite was then cold worked (groove rolling and drawing) into a wire with diameter of 1.6 mm. The wire was then cut into 37 pieces of short wires, which were bundled and inserted into a Cu-20%Ni tube (inner diameter: 11.2 mm, outer diameter: 20 mm) to form a new composite. The new composite was then cold worked as above into a 37-filamentary wire (Ta-37) with diameters of 1.6 mm and 1.3 mm (more than 1 meter length for both wires) as shown in Fig. 3-1. The wires were then cut into short wires with a length of 4 cm for the heat treatment. Three kinds of heat treatment processes (shown in Fig. 3-2) were used in this work, denoted #1, #2, and #3. The process #1 consists of the temperature rising from room temperature to 640 °C in 1 hour, holding the temperature at 640°C for 5 hours, and then cooling to room temperature in the furnace. The process #2 consists of a temperature increase to 670 °C in 1 hour and holding at 670 °C for 3 hours, and then cooling to room temperature in the furnace. The process #3 consists of a temperature increase to 640 °C in 1 hour, a further increase to 670 °C in 3 hours, holding at 670 °C for 2 hours, and then cooling to room temperature. The short wires were wrapped with Zr foil and heat treated under Ar gas atmosphere (about 1 atm).

The mono- and 7-filamentary IMD-processed MgB_2 wires with a Ta-inner sheath and a Cu-Ni outer sheath were also fabricated for comparison. And they were termed as Ta-mono and Ta-7, respectively. Both the Ta-7 and Ta-mono are SiC-added wires, and with a diameter of 1.3 mm. The wire fabrication details of Ta-mono and Ta-7 have already been reported in our previous papers [4-6].

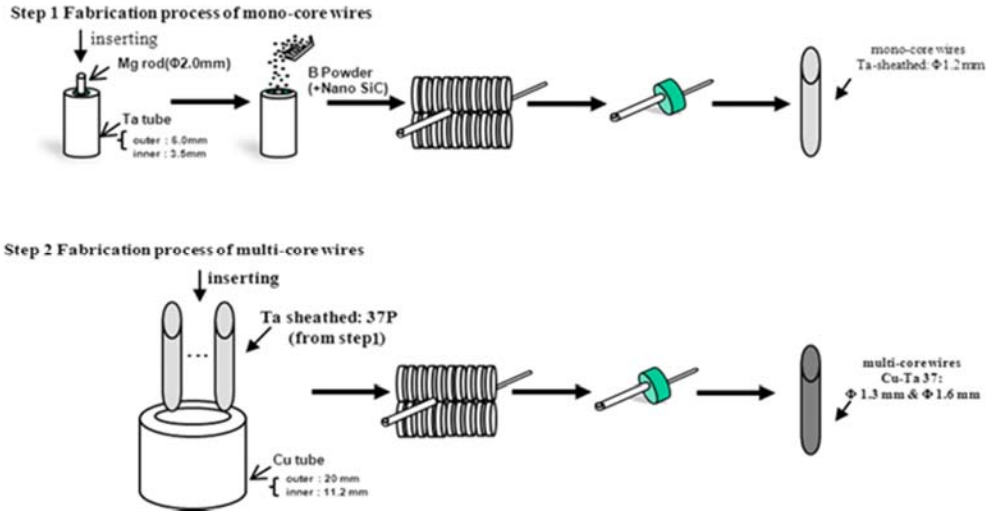

Fig. 3-1 Fabrication process of 37-filamentary IMD-processed MgB_2 wires

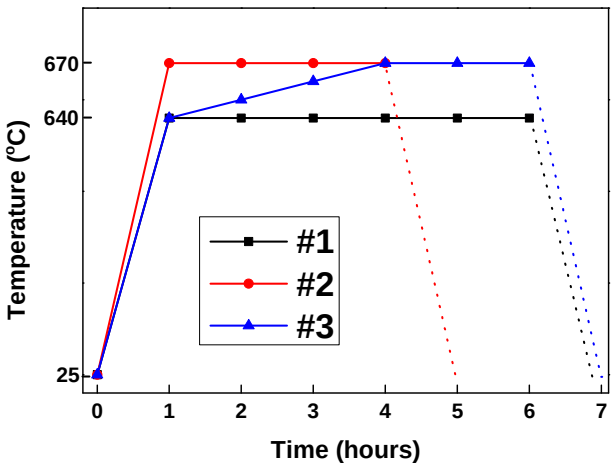

Fig. 3-2 Heat treatment processes for IMD-processed 37-filament MgB_2 wires

3.3 Results and discussion

Fig. 3-3 (a) shows SEM images of the transverse cross section of the IMD-processed 37-filamentary wire (center) and 4 filaments of the wire (surrounding). MgB_2 is formed along the inner wall of the Ta sheath in each filament. A hole is formed at the center of each filament due to Mg diffusion into the B layer. The hole is filled with resin during the polishing process. The filament sizes are small, and with a diameter of less than 100 μm. The MgB_2 area fraction is less than 2% in this experiment, which is smaller than that in the mono- and 7- filament IMD-processed MgB_2 wires in our previous work [8-11]. The low MgB_2 area fraction for the IMD-processed multi-filament MgB_2 wires is mainly due to (1) the thick Ta and Cu-Ni tubes, and (2) the hole generated in the center of each filament. Increase of the MgB_2 fraction of IMD-processed multi-filament MgB_2 wires is now under investigation. Fig. 3-3 (b) shows the EDS element mapping images of one filament of Fig. 3-3(a). The Mg completely diffused to B layer to form MgB_2. There is no concentration difference for Mg in the whole MgB_2 layer. This is because the diffusion distance of Mg in the filament less than 10 μm caused a full reaction between Mg and B. The MgO region can be found in inner wall of MgB_2 hole. This MgO region suggests that the Mg is left even after full reaction with B, which indicates that the MgB_2 area fraction could be further increased by optimizing the Mg rod diameter and B layer thickness. The carbon in the mapping is considered to be caused by the resin introduced during the polishing process.

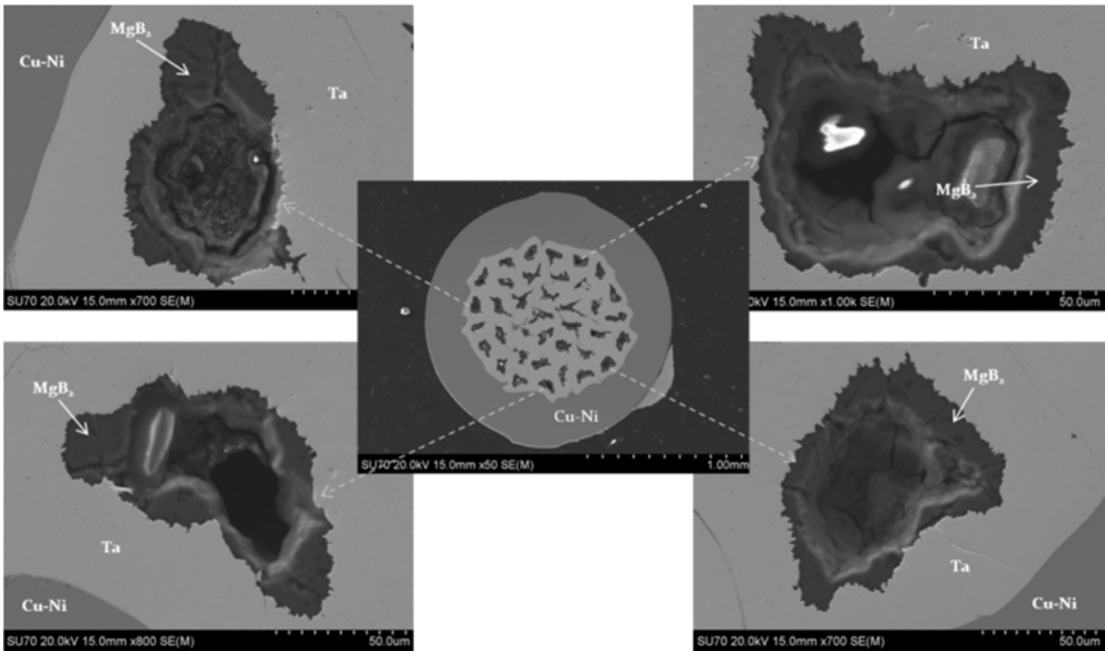

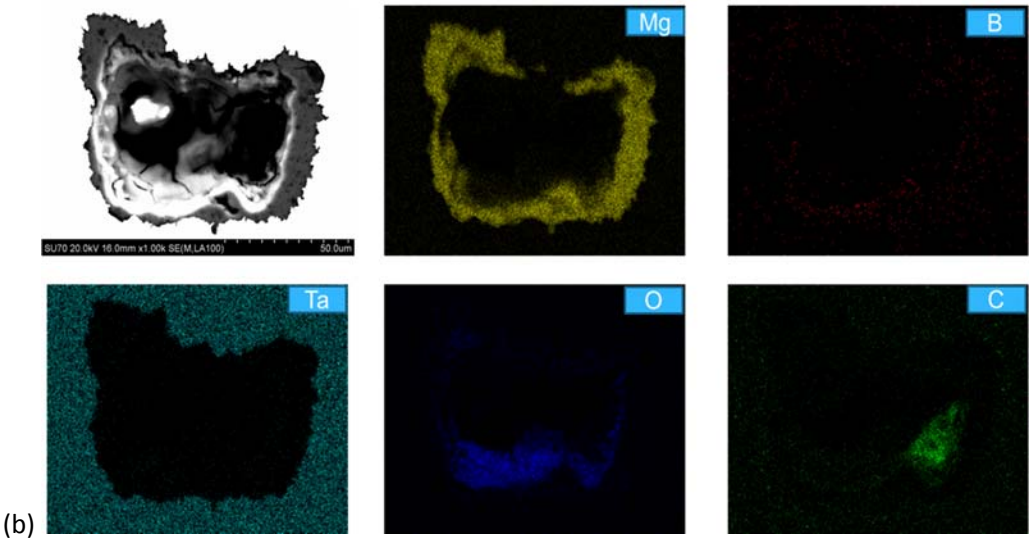

Fig. 3-3 (a) SEM images of IMD-processed 37-filament MgB_2 wires and its filaments, and (b) the elements mapping for one filament of (a)

Fig. 3-4(a) shows the J_e value at 4.2 K and 10 T of the IMD-processed 37-filament MgB_2 wires with the different heat treatment conditions shown in Fig. 3-2. The SiC-added wires show higher J_e

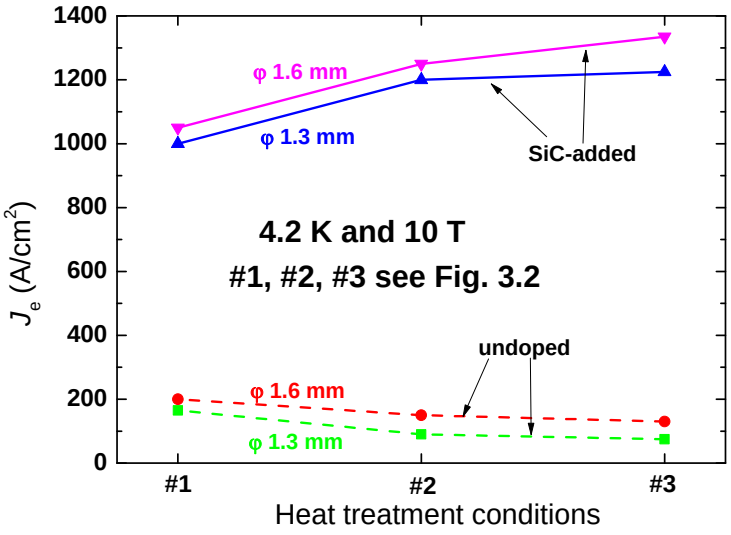

(a)

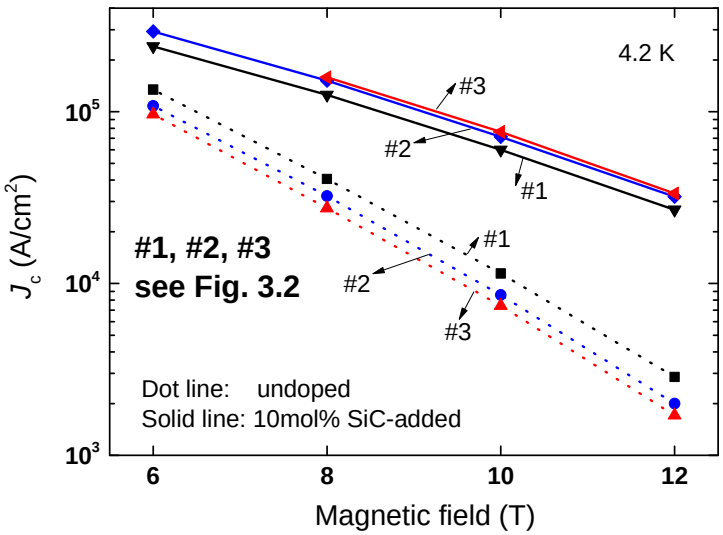

(b)

Fig. 3-4 (a) J_e values at 4.2 K and 10 T, and (b) J_c-B curves at 4.2 K for several heat treatment conditions of the IMD-processed 37-filament MgB_2 wires

values than those of the undoped wires. This is because carbon substitution causes impurity scattering, thereby, enhanced the upper critical field (B_{c2}), and hence enhancement of critical current properties in high fields such as 10 T. The 1.6 mm diameter wires show higher J_e values than that of the 1.3 mm diameter wires for both undoped and SiC-added wires. This is considered that some filaments of the 1.3 mm diameter wires are so small that MgB_2 is no longer uniformly formed along the inner wall of the Ta sheath, while uniform MgB_2 along the inner wall of the Ta sheath is formed for the 1.6 mm diameter wires in this research. Uniform MgB_2 with 1.3 mm diameter could be obtained by optimizing parameters such as the Mg rod diameter, B layer thickness, and thickness of the sheaths. The optimized heat treatment conditions for undoped and SiC-added wires are different. The J_e values for the SiC-added wires are sensitive to the heat treatment conditions, and the #3 conditions can yield the highest J_e. For the undoped wires, #1 yielded the highest J_e values, however, the differences among the three conditions are small.

The J_c-B curves at 4.2 K for the 1.6 mm diameter undoped and SiC-added wires are shown in Fig. 3-4(b). All of the SiC-added wires and undoped wires have similar slopes, respectively. This suggests that the amount of carbon substitution in boron sites is independent of the heat treatment conditions used in this experiment. The highest J_c in all measured magnetic fields for the SiC-added wires was obtained by the #3 heat treatment condition, and the #1 for the undoped wires. The nano-sized SiC particles affect the reaction between Mg and B and are responsible for the J_c difference of SiC-added wires, though the details remain unclear.

Fig. 3-5 shows J_c-B curves at 4.2 K for the IMD-processed MgB_2 wires with the same 10 mol% SiC addition but with different filament numbers, and under the same heat treatment condition (#3). The details of compared wires are listed in table 3-1. The J_c-B curves for all samples show the same slopes due to the same amount of carbon substitution for boron in all of the samples. The 37-filamentary IMD-processed MgB_2 wires show the highest J_c at all measured magnetic fields, achieving a value of 7.6 x 10^4 A/cm^2 (I_c = 27 A) at 4.2 K and 10 T. The Ta-7 wire shows a slightly lower J_c (about 7.1 x 10^4 A/cm^2 at 4.2 K and 10 T) than the Ta-37 wires but higher than that for the Ta-mono wires (6.6 x 10^4 A/cm^2 at 4.2 K and 10 T).

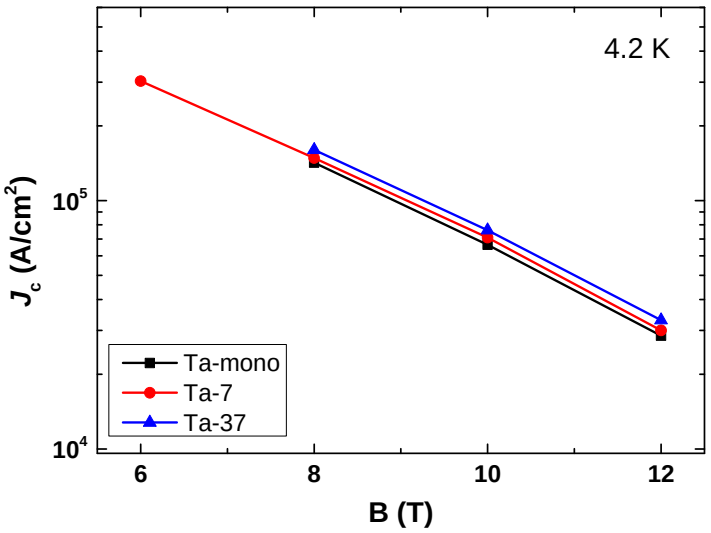

Fig. 3-5 J_c-B curves of the IMD-processed MgB_2 wires with different filaments at 4.2 K

(Specification of the samples are listed in table 3-1)

Table 3-1. The details of compared wires in Fig. 4

	Ta-mono	Ta-7	Ta-37
Diameter (mm)	1.3	1.3	1.6
B layer thickness (μm)	< 100	< 50	< 20
MgB_2 area fraction (%)	5%	3%	1.8%
J_c at 4.2 K and 10 T (A/cm²)	66,000	71,000	76,000

In order to investigate the difference in J_c between the Ta-37 and Ta-mono wires in Fig. 3-5, their transverse cross sectional microstructures were observed with SEM. Fig. 3-6(a) and 6(b) show SEM images of MgB_2 layers near the Ta sheath and near the hole of the IMD-processed Ta-mono MgB_2 wires, respectively. There are a number of dark spots with sizes of 1-10 μm in the MgB_2 layers. I used the SEM-EDX to observe the different spots in Fig. 3-6 (b), the characteristic spectrum details of B (B k), C (C k), Mg (Mg k) and Si (Si k) are listed in table 3-2. The atomic ratio of B decreases and Mg increases from spot 1 (the deep dark spot), to spot 2 (dark spot), and then to spot 3 (normal region, also MgB_2 layer). By comparing the ratio (at%) Mg:B among the three spots, and with spot

3 identified as normal MgB_2 layer, we see that spot 3 is the most Mg-rich, much higher than the stoichiometric ratio of 1:2. I think this is because it is difficult for EDX to detect the light elements such as C and B, so the B and C are underestimated. This suggests that Mg is overestimated because the atomic ratio adds up to 100% for each spot. However, the ratio of Mg to B is expected to be a good indicator to estimate that the dark spots are un-reacted B particles or B-rich region, which is consistent to our previous research [9, 11]. Fig. 3-6(c) and 3-6(d) show SEM images of two filaments of the Ta-37 wires. There are also unreacted B particles in the MgB_2 layer, however, the average size of these is much smaller than that of the Ta-mono wires. The thickness of the MgB_2 layer for the Ta-mono wire is around 100 µm, while that of Ta-37 is mostly less than 20 µm. The smaller thickness of the MgB_2 layer in Ta-37 indicates a shorter Mg diffusion distance, which leads to smaller-sized unreacted B particles. These smaller-sized unreacted B particles in Ta-37 are mainly responsible for its higher J_c, shown in Fig. 3-5.

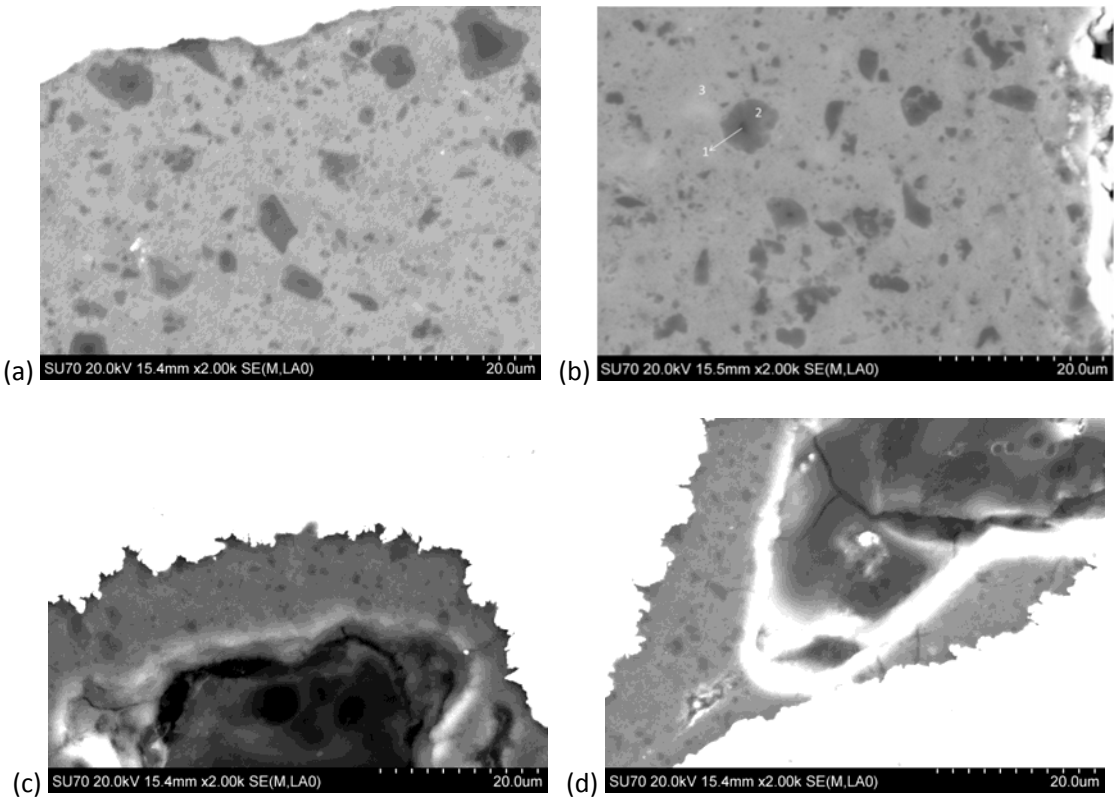

Fig. 3-6 SEM images in transverse cross-section of Ta-mono (a) near the Ta sheath and (b) near the hole (spectrum are observed for spots 1, 2 and 3), (c) Ta-37 filament 1, and (d) Ta-37 filament 2

Table 3-2. The characteristic element spectrum details of B (B k), C (C k), Mg (Mg k) and Si (Si k) for Fig. 5(b)

Atomic %	spot 1	spot 2	spot 3
B k	50.92	37.95	9.88
C k	6.43	5.78	9.91
Mg k	42.04	54.06	70.94
Si k	0.61	2.21	9.27

Fig. 3-7(a) shows the temperature dependence of the J_c-B curves for SiC-added 37-filament wires fabricated with the IMD process. At 20 K, the J_c value is about 1.1 x 10^5, 0.6 x 10^5, and 0.3 x 10^5 A/cm^2 at 3 T, 4 T, and 5 T, respectively. The J_e value is about 2 x 10^3 A/cm^2 at 20 K and 3 T. J_c values higher than 1.0 x 10^5 A/cm^2 are observed at 4.2 K at 9 T, 10 K at 7 T, 15 K at 5 T, and 20 K at 3 T. The temperature dependence of J_c for undoped (heat treatment condition: #1) and 10 mol% SiC-added (heat treatment condition: #1) 37-filament MgB_2 wires is compared in Fig. 3-7(b). The SiC-added wire shows higher J_c at both 4.2 K and 15 K in all measured magnetic fields, while the undoped wire shows higher J_c at 30 K in all measured magnetic fields. At 20 K, the SiC-added wire shows higher J_c in fields higher than 4 T, while it shows lower J_c in fields lower than 4 T. J_c at 20 K and 3T for the undoped wires is about 1.6 x 10^5 A/cm^2, while J_e is about 2.8 x 10^3 A/cm^2. These results reveal that SiC-addition has two effects: One is carbon substitution for boron, which enhances B_{c2} and increases J_c in high magnetic fields. The other is the decrease in T_c, which decreases J_c at high temperatures and low magnetic fields. This suggests that the use of undoped or SiC-added wires for practical applications depends on the application temperature and magnetic field. Fig. 3-7 (c) shows the dependence of I_c on the temperature (higher than 30 K) at the self-field for both undoped and SiC-added IMD-processed 37-filament MgB_2 wires. The undoped wires show higher I_c than the SiC-added wires at all temperatures higher than 30 K. At 30 K, the I_c is about 155 A (J_c: 4.4 x 10^5 A/cm^2) for the undoped wires and 26 A (J_c: 7.3 x 10^4 A/cm^2,) for the SiC-added wires. The difference in I_c at temperatures higher than 30 K is mainly due to the difference in T_c, 38.2 K for the undoped wires and about 33.3 K for the SiC-added wires.

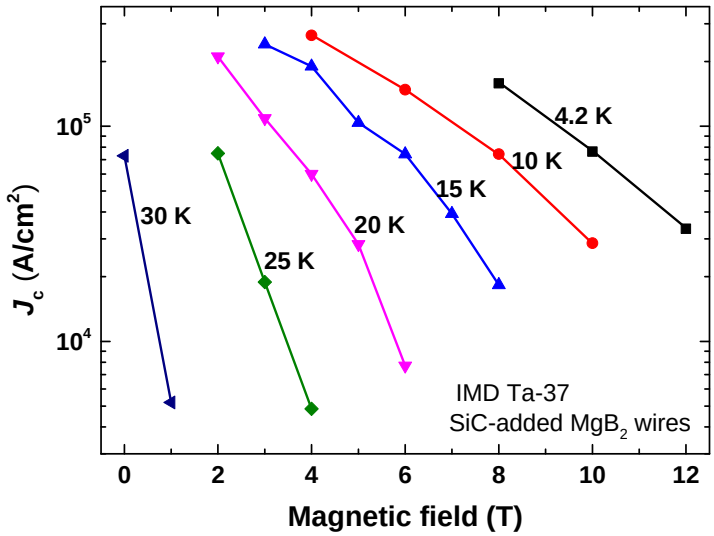
10^5
10^4
J_c (A/cm^2)
30 K
25 K
20 K
15 K
10 K
4.2 K
IMD Ta-37
SiC-added MgB_2 wires
0
2
4
6
8
10
12
Magnetic field (T)

(a)

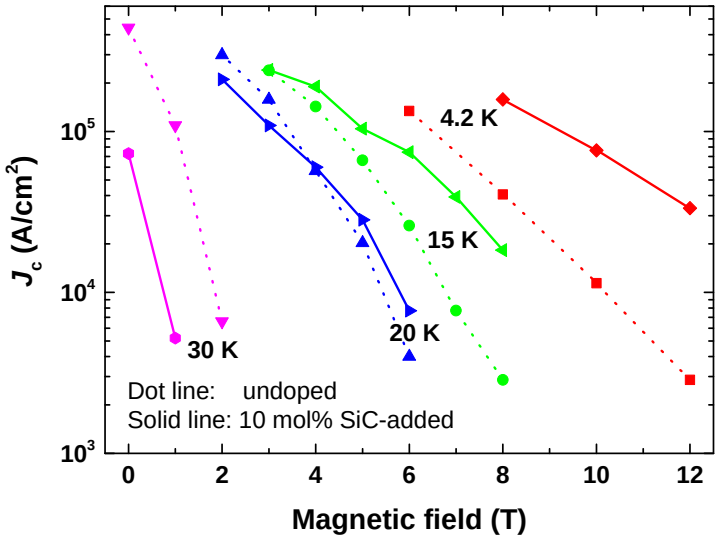
10^5
10^4
10^3
J_c (A/cm^2)
4.2 K
15 K
20 K
30 K
Dot line: undoped
Solid line: 10 mol% SiC-added
0
2
4
6
8
10
12
Magnetic field (T)

(b)

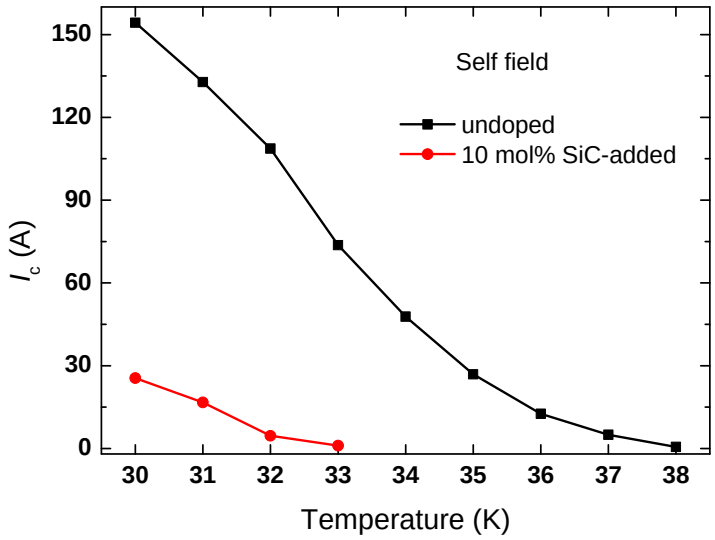

(c)

Fig. 3-7 Temperature dependence of the J_c-B curve for (a) SiC-added, (b) both undoped and SiC-added IMD-processed 37-filament MgB_2 wires, and (c) temperature dependence of I_c on the temperature (higher than 30 K) at the self-field for both undoped and SiC-added IMD-processed 37-filament MgB_2 wires

3.4 Conclusions

We successfully fabricated 37-filament MgB_2 wires with IMD process in this study. The fabrication conditions, impurity addition, critical current properties, and microstructural characteristics are investigated. Compared to mono-filamentary and 7-filamentary wires, higher critical current density was obtained for the 37-filamentary wire, which is considered to be due to the decrease of Mg diffusion distance by the increase of the filament numbers. The filaments size of as small as ~100 μm was obtained, although the Mg rod is considered to be difficult to be cold-worked. This study suggests that the IMD process can be used to fabricate large-scale MgB_2 wires for practical applications. Optimization of the starting composite materials (such as the Mg rod diameter, thickness of the B layer, thickness of the Ta tube, and thickness of the Cu-Ni tube) is expected to increase the MgB_2 superconducting area, which will be investigated in future work.

References

[1] http://www.hypertechresearch.com/index.htm
[2] http://www.columbussuperconductors.com/supercond.asp
[3] Giunchi G, Ceresara S, Ripamonti G, Zenobio A Di, Rossi S, Chiarelli S, Spadoni M, Wesche R and Bruzzone P L 2003 *Supercond. Sci. Technol.* 16 285
[4] Togano K, Hur J, Matsumoto A and Kumakura H 2009 *Supercond. Sci. Technol.* 22 015003
[5] Togano K, Hur J, Matsumoto A and Kumakura H 2010 *Supercond. Sci. Technol.* 23 085002
[6] Kumakura H, Hur J, Togano K, Matsumoto A, Wada H and Kimura K 2011 *IEEE Transactions on Applied Superconductivity* 21 2463
[7] Ye S J, Matsumoto A, Togano K, Ohmura T and Kumakura H 2013 *Supercond. Sci. Technol.* 26 105027
[8] Hur J H, Togano K, Matsumoto A, Kumakura H, Wada H and Kimura K 2008 *Supercond. Sci. Technol.* 21 032001
[9] Ye S J, Song M, Matsumoto A, Togano K, Zhang Y, Kumakura H, Takeguchi M, Teranishi R and Kiyoshi T 2012 *Supercond. Sci. Technol.* 25 125014
[10] Ye S J, Matsumoto A, Togano K and Kumakura H 2011 *Physica C* 471 1133
[11] Ye S J, Song M, Matsumoto A, Togano K, Takeguchi M, Kumakura H, Teranishi R and Kiyoshi T 2013 *Physica C* 484 167
[12] Li G Z, Sumption M D, Susner M A, Yang Y, Reddy K M, Rindfleisch M A, Tomsic M J, Thong C J and Collings E W 2012 *Supercond. Sci. Technol.* 25 115023

Chapter 4 Enhancement of critical current properties of IMD-processed MgB_2 wires by SiC and liquid aromatic hydrocarbon co-addition

4.1 Introduction

As introduced in Chapter 1, C-containing impurity addition (especially SiC addition), originally developed for the PIT process [1-4], is also effective in enhancing in-field J_c values of IMD-processed MgB_2 wires. Hur *et al.* fabricated IMD-processed MgB_2 wires with SiC addition and obtained a J_c of 41,000 A/cm^2 at 4.2 K and 10 T [5]. Our group [6-8] fabricated multi-filamentary IMD wires with SiC addition, and the J_c of MgB_2 layer reached as high as 9.9×10^4 A/cm^2 at 4.2 K and 10 T [7, 8].

For PIT process, Yamada *et al.* reported that the co-addition of ethyltoluene and SiC give further improvement of in-field J_c [9, 10] of MgB_2 wires, and they obtained a very high J_c of 4.5×10^4 A/cm^2 at 4.2 K and 10 T by the co-addition of ethyltoluene and SiC, and applying hot pressing [10].

In this study, I tried the SiC and *p*-ethyltoluene co-addition to the IMD-processed MgB_2 wires. I also tried two other aromatic hydrocarbons, toluene and *p*-dimethylbenzene, which have the similar molecule structure as *p*-ethyltoluene. The details for this chapter are described on our previous paper [11, 12].

4.2 Experimental details

B (99%, 325-mesh) and 10 mol% nano-SiC (a few tens of nanometer size) powders were well ground in a mortar. Liquid aromatic hydrocarbon was then mixed with the starting powders (B+SiC) in the mortar, and then the mixture was kept in the draft chamber till air-dried. After air-drying, the mixture were re-ground into uniform powder. The mixed powder was packed into the gap between a Fe tube and a pure Mg rod which was coaxially inserted into the Fe tube. Then the composite was groove-rolled into a rod shape and drawn into a wire with diameter of 1.2 mm. The wire was cut into short pieces of 40 mm length, which were wrapped with Zr foils and heat treated under Ar gas atmosphere at temperatures of 640℃, 670℃ and 700℃ for 3 h. The details of

fabrication process were described in Chapter 1. We also fabricated wires without addition (pure), and with nano-SiC addition for comparison. Furthermore, the wire with toluene addition was also fabricated for comparison.

The microstructure of the samples was investigated by optical microscope and x-ray diffraction (XRD). Scanning electron microscopy (SEM) and transmission electron microscopy (TEM) were carried out with the Hitachi SU-70 and JEM-2100F, respectively. The samples for TEM observation is the 100 nm thin film of a longitudinal cross section of the wire produced by a focused ion beam (FIB).

The transport critical current (I_c) for the wires was measured at temperatures of 4.2, 10, 15, 20, 25, and 30 K in magnetic fields below 13 T using a four-probe resistance method. The value of J_c for each wire was calculated by dividing I_c by the whole MgB_2 area including B-rich region. The J_e was calculated by dividing I_c by the entire wire area in the transverse cross section.

4.3 Results and discussion

4.3.1 Enhancement of J_c and J_e for MgB_2 wires by SiC and liquid aromatic hydrocarbon co-addition

Fig. 4-1(a), 1(b) and 1(c) show the J_e-B properties of the five samples (pure, SiC addition and three co-addition: SiC+toluene, SiC+ethyltoluene and SiC+dimethylbenzene) heat treated at 640 ℃, 670 ℃ and 700℃ for 3 h, respectively. The J_e value of SiC added wires is superior to that of pure wires in the whole regions of magnetic field and further improvement is observed for SiC+toluene co-added wires. These are independent of heat treatment temperature. On the other hand, SiC added wires and SiC+toluene co-added wires show high J_e values in the high-field region with comparable field dependence which is smaller than that of pure wires. These results are probably due to the C substitution for B which enhances B_{c2}, and hence the J_c [13] (here J_e) in the wires with SiC addition and SiC+toluene co-addition.

At 640℃, SiC+toluene co-added wires show the best J_e values which are about twice as high as that of SiC added wires in all fields. The SiC+ethyltoluene co-addition firstly reported for the PIT processed tape by Yamada *et al* [9, 10] brings about a 10% enhancement in J_e, compared with SiC added wires in all fields. SiC+dimethylbenzene co-added wires show lower J_e value than SiC added wires in 10 and 12 T while higher in 8 T. It is interesting to note that the pure wires show higher J_e

value than the SiC+ethyltoluene co-added wire and SiC+dimethylbenzene co-added wire by about 14% and 33%, respectively, in 6 T while the opposite results are observed above 6 T.

At 670℃, the J_e value of SiC+dimethylbenzene co-added wires is about 3,700 A/cm^2 at 4.2 K and 10 T. The J_e value at 8 T may be under-estimated because the measured I_c was deteriorated due to temperature rise of samples which is caused by the Joule heating at current contact. The sample was damaged and burned at the 8 T measurement, and therefore we couldn't carry out the I_c measurement at 6 T. The SiC+toluene co-addition also brings about J_e enhancement by about 20%, compared with SiC addition in all magnetic fields. SiC+ethyltoluene co-added wire shows J_e value lower than SiC added wire by 50% in all fields.

At 700℃, the result is similar to that at 670℃. The SiC+dimethylbenzene co-added wire shows the best J_e property in all fields although the J_e value in 6 T may be also under-estimated due to the Joule heat generation. The SiC+toluene co-added wire shows higher J_e value than SiC added wire by about 20%, and SiC added wire also shows higher J_e value than SiC+ethyltoluene added wire by about 20% in all fields. Comparing to pure wires, the SiC+dimethylbenzene co-added wire shows about twice J_e value in 6 T while 20 times in 12 T.

The best J_c values calculated for the cross-sectional area of MgB_2 layers of each wire are compared in Fig. 4-1(d). SiC+toluene co-added wire heat treated at 640℃ shows the best J_c property in all fields, and the J_c value at 4.2 K and 10 T is about 4.8 x 10^4 A/cm^2, which is higher than those of SiC added IMD processed wires reported by Hur *et al* [5] and other PIT-processed wires and tapes reported so far. Furthermore, the B powder I used has lower quality (99.8%, 325-mesh) than those used by others [5-8]. The small field dependence observed for wires with additive suggests that C substitution for B in MgB_2 occurred and enhanced critical current properties in high fields. The J_c of the SiC+ethyltoluene co-addition is the lowest among wires with the additives, which is different from the results obtained by Yamada *et al* in the PIT-processed MgB_2 tapes. This difference is considered to be due to the difference of reaction process between the IMD- and PIT-processed MgB_2 wires.

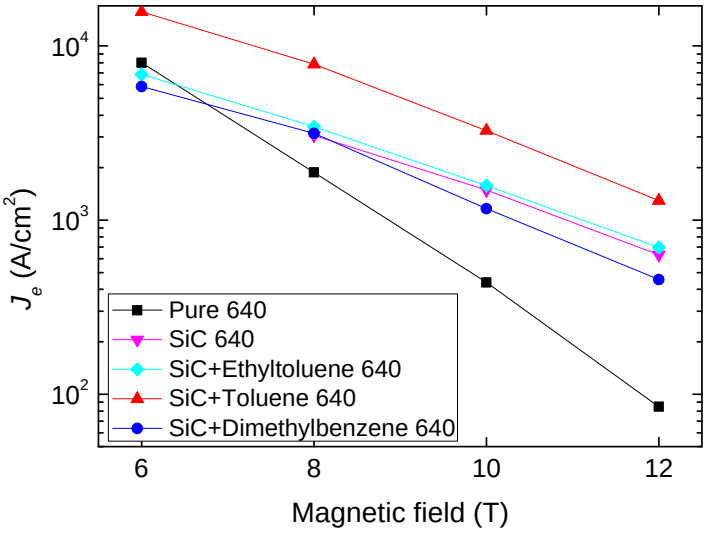
10^4
10^3
10^2
J_e (A/cm^2)
Pure 640
SiC 640
SiC+Ethyltoluene 640
SiC+Toluene 640
SiC+Dimethylbenzene 640
6
8
10
12
Magnetic field (T)

(a)

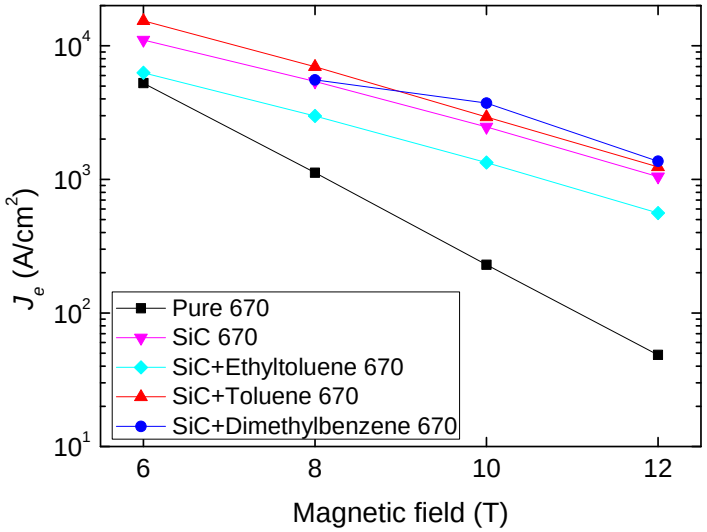
10^4
10^3
10^2
10^1
J_e (A/cm^2)
Pure 670
SiC 670
SiC+Ethyltoluene 670
SiC+Toluene 670
SiC+Dimethylbenzene 670
6
8
10
12
Magnetic field (T)

(b)

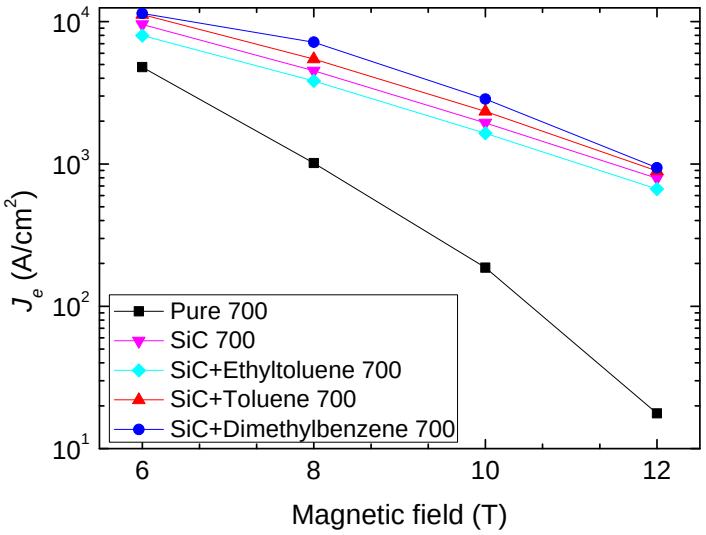

(c)

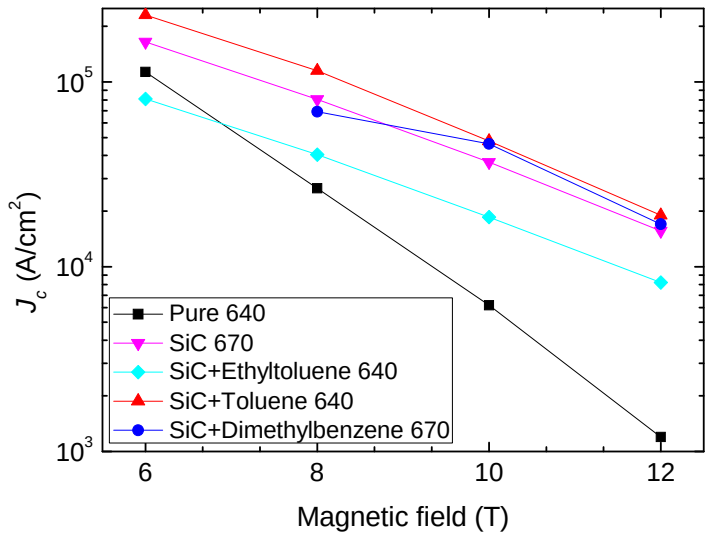

(d)

Fig. 4-1 J_e-B curves (at 4.2 K) of various IMD-processed MgB_2 wires heat treated at (a) 640℃, (b) 670℃ and (c) 700℃ for 3 hours, and (d) J_c-B curves (at 4.2 K) of various IMD processed MgB_2 wires: optimized heat treatment temperature was chosen for each wire

As introduced above, SiC +dimethylbenzene co-added samples showed the effective enhancement of J_e of the IMD-processed MgB_2 wires. I measured the J_c and J_e properties of the SiC+ dimethylbenzene co-added wires at temperatures of 4.2, 10, 15, 20, 25, and 30 K in the magnetic fields below 13 T using a four-probe resistance method. The J_c of pure wires are also measured. Fig. 4-2 (a) and (b) show the J_c-B curves and J_e-B curves of SiC+dimethylbenzene co-added IMD-processed MgB_2 wires, respectively. The J_c at 4.2 K and 10 T for the sample is 4.5 x 10^4 A/cm^2. At 20 K, its J_c is about 5.3 x 10^4 at 5 T and 1.0 x 10^5 A/cm^2 at 4 T. At 30 K and 0 T, its J_c is about the 1.2 x 10^5 A/cm^2. At 20 K and 5 T its J_e is 4.2 x 10^3 A/cm^2. The J_c-B curves for the pure wires are shown in the Fig. 4-2 (c) for comparison. Its J_c values are lower than that of SiC+ dimethylbenzene wires at high measured field and low temperature, while higher at low field and high temperature. At 30 K and 0 T, its J_c is about 1.3 x 10^5 A/cm^2.

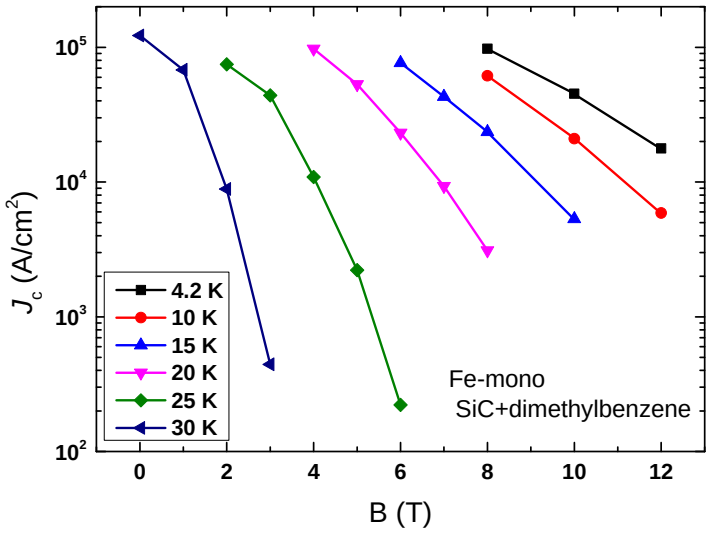

(a)

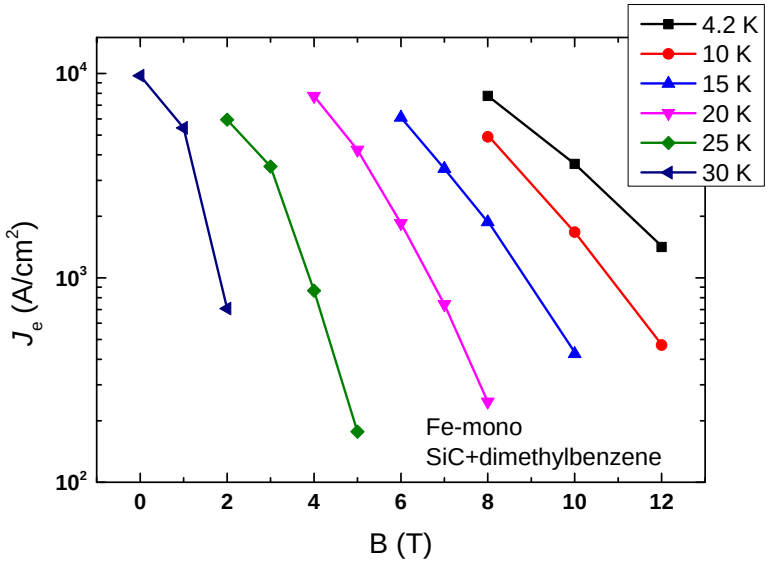

(b)

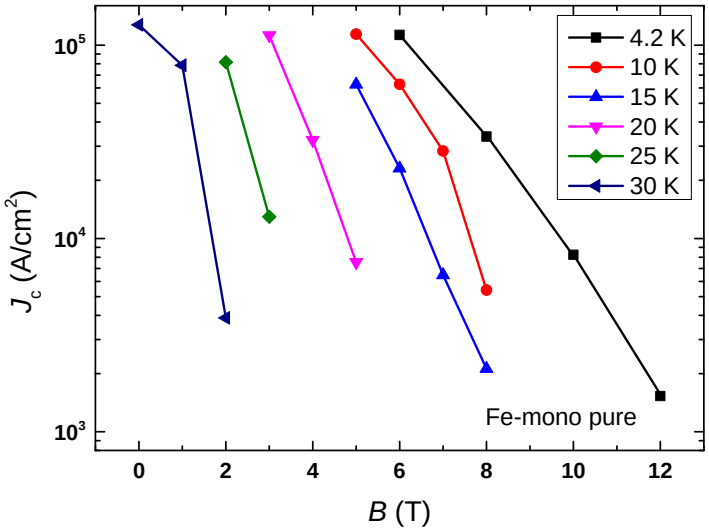

(c)

Fig. 4-2 (a) the J_c-B curves and (b) the J_e-B curves of SiC+dimethylbenzene co-added IMD-processed MgB_2 wires, respectively. (c) the J_c-B curves of pure IMD-processed MgB_2 wires

4.3.2 Study on the mechanism of the J_c enhancement of MgB_2 wires by SiC and toluene co-addition

In order to study the mechanism of J_c increase properties by these additives, I compared the J_c and microstructure of pure, toluene-added, SiC-added, and SiC and toluene co-added IMD-processed MgB_2 wires. The wires in the following experiment were heat treated at 670 ℃ for 3 hours. This temperature condition caused full reaction between Mg and B, hence, it is better to obtain critical current properties with good reproducibility.

Fig. 4-3 show the J_c-B curves of pure wire and wires with toluene addition, SiC addition and SiC+toluene co-addition. The J_c of the added-wires were superior to that of pure wires. We could not measure I_c under 8 T of SiC+toluene co-added wires and SiC-added wires because the current was so high (both wires had an I_c value of more than 200 A at 6 T) that the wire might have burned out due to the Joule heat at the current contact. The SiC+toluene co-added wire showed the highest J_c value above 8 T and the smallest field dependence in all wires. The J_c value of SiC+ toluene co-added wires was about 5 x 10^4 A/cm^2 at 10 T and 4.2 K, which is 1.2 times higher than that of SiC-added wires, but, at 8 T and 4.2 K, the value was almost the same. SiC-added wires showed a notable higher J_c value and smaller magnetic field dependence than toluene-added wires. The J_c value of toluene-added wire was about 17 % of that of SiC-added wires but 1.4 times of that of pure wires at 10 T and 4.2 K. The magnetic field dependence of toluene-added wires was larger than that of SiC-added wires and smaller than that of pure wires.

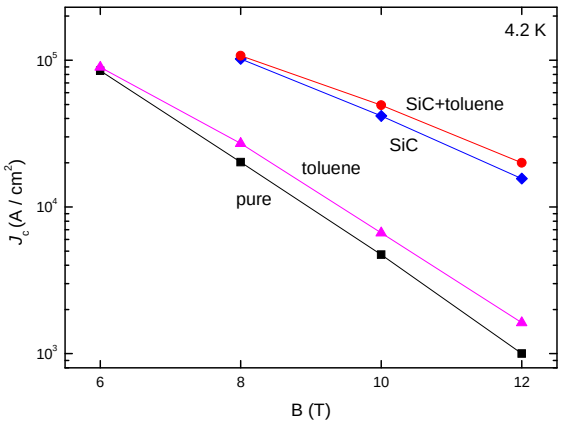

Fig. 4-3 J_c-B curves of IMD-processed MgB_2 wires with different additives

Fig. 4-4 shows the XRD pattern of all wires fabricated in this experiment. Strong Fe peaks are from the Fe sheath. The peaks of Mg_2Si which is formed by the reaction between SiC and Mg are also clearly observed in the SiC- containing additives (SiC addition and SiC+toluene co-addition). MgO may be formed by the reaction during the heat treatment. The 110 peaks of MgB_2 are shifted toward high-angle sides by additives (toluene, SiC, and SiC+toluene). The a-axis, c-axis lattice parameter, and amount of carbon substitution for boron (x in the $Mg(B_{1-x}C_x)_2$) calculated using the results of Lee *et al*. [14] are listed in Table 4-1. The values of the c-axis almost remain the same, while the a-axis decreased with the additives. The amount of carbon substitution for boron in the toluene addition was about 0.01, and that of SiC addition was 0.037, while, in the SiC+toluene co-addition, it was 0.042, which is smaller than the sum of the SiC addition and toluene addition (0.047). This may be due to the reason that SiC and toluene competed and suppressed each other in the reaction process of carbon substitution for boron. This carbon substitute for boron seems to be one of the main reasons for the J_c enhancement [13] in applied magnetic fields of our IMD-processed MgB_2 wires.

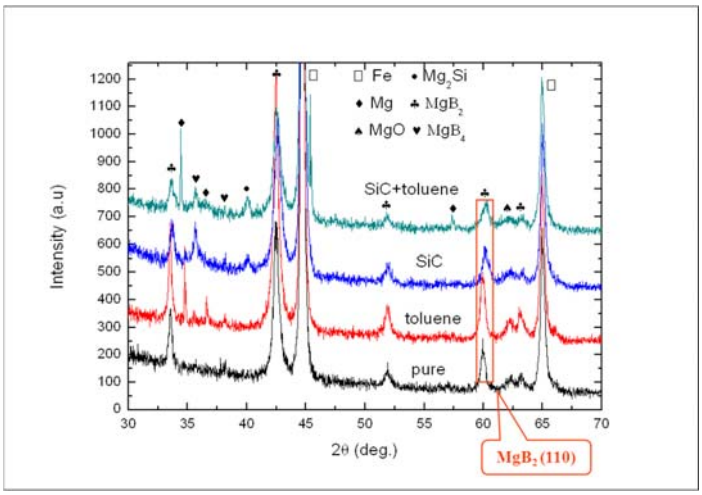

Fig. 4-4 XRD patterns of IMD-processed MgB_2 wires with different additives

Table 4-1. The a-axis, c-axis, and amount of carbon substitution for boron of IMD-processed mono-core MgB_2 wires with different additives

Additives	a-axis (A)	x of $Mg(B_{1-x}C_x)_2$	c-axis (A)
Pure	3.08583	0	3.52058
Toluene	3.08142	0.01	3.52564
SiC	3.06958	0.037	3.52317
SiC+toluene	3.06726	0.042	3.52129

Fig. 4-5(a), (b), (c), and (d) show the SEM images on the transverse cross section of all wires. The grain size of doped wires (Fig. 4-5(b), (c), and (d)) seems smaller than that of pure wires (Fig. 4-5(a)); in particular, the grain size of wires with the toluene-containing addition (Fig. 4-5(b) and (d)) is much smaller. A small grain size can increase the grain boundary area, which increases the flux pinning force, and hence leads to J_c enhancement. This may be another reason why toluene addition increases J_c values.

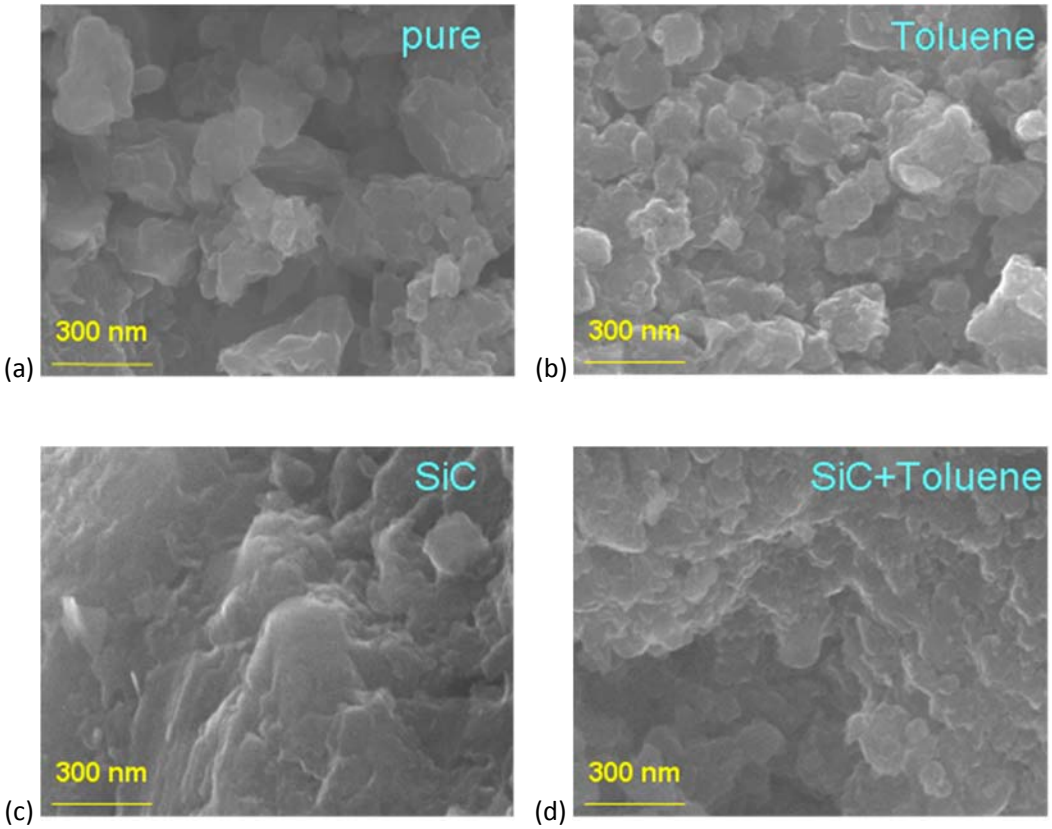

Fig. 4-5 SEM images of IMD-processed MgB_2 wires (a) with no addition, (b) with toluene-addition , (c) with SiC-addition, (d) with both SiC and toluene co-addition

4.3.3 The microstructure analysis and a proposal of new mechanism of enhanced J_c of MgB_2 wire by SiC addition

As introduced above, SiC addition is mainly responsible for the J_c enhancements of IMD-processed MgB_2 wires. In this section, the microstructures of SiC-added IMD-processed MgB_2 wires by SEM and TEM are shown. The undoped wires are also presented for comparison.

Fig. 4-6 show the representative SEM image (Fig. 4-6 (a)) and its EDX element mapping images of SiC-added IMD-processed MgB_2 layer. Fig. 4-6 (b-f) show B, O, Mg, Si, and C elements, respectively. The EDX images indicated that the dark spots are the un-reacted B particles. These un-reacted B particles are not superconductive, so the decrease of this un-reacted B powder can increase the critical current properties of IMD-processed MgB_2 wires.

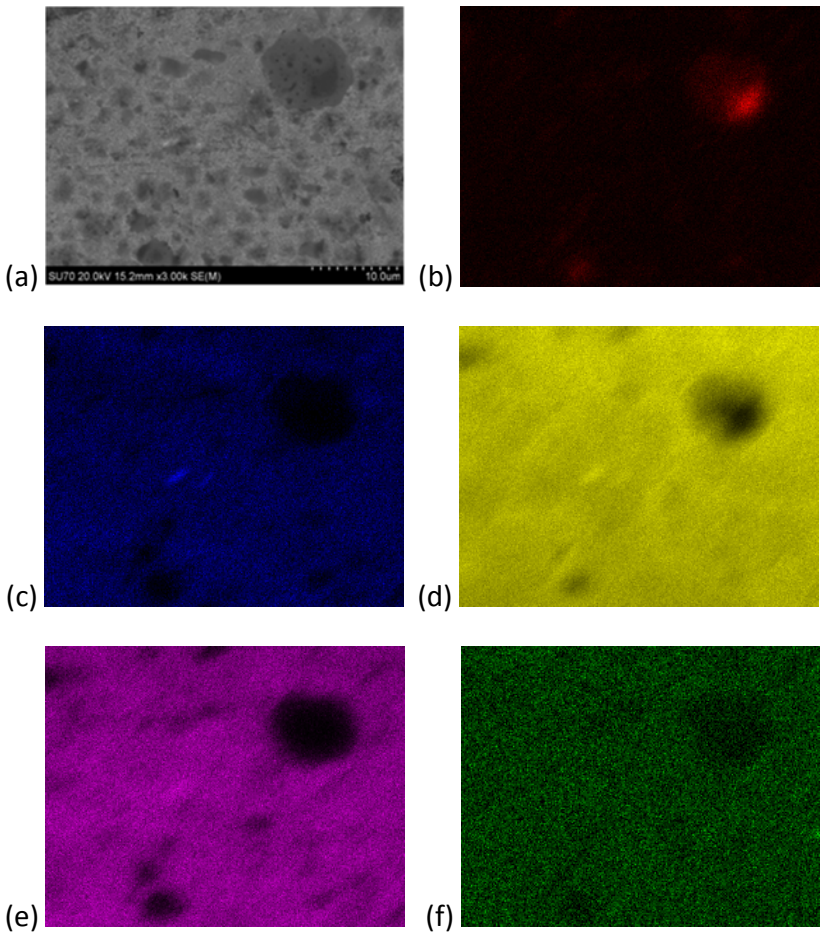

Fig. 4-6 Representative SEM image(a), EDX element mapping images of B, O, Mg, Si and C elements (b - f), on the longitudinal cross sections of SiC-added IMD-processed MgB_2 wires

Fig. 4-7(a) is a TEM bright field image of the MgB_2 layers of SiC-added IMD-processed MgB_2 wires. The grain size is mostly less than 100 nm, which is consistent with the SEM images in Fig. 4-5. Fig. 4-7(b) shows typical high-resolution image of region A in Fig. 4-7(a), and its diffraction pattern is shown in the Fig. 4-7(c). We can see that MgB_2 and Mg_2Si crystals exist in the region A. Fig. 4-7(d) shows the high-resolution image of region B in Fig. 4-7(a). Its diffraction pattern (Fig. 4-7(e)) show that this region is in amorphous state. For the SiC-added IMD-processed MgB_2 wires, the un-reacted B particle is mostly the amorphous state, which is consistent with the SEM-EDX images of Fig. 4-6.

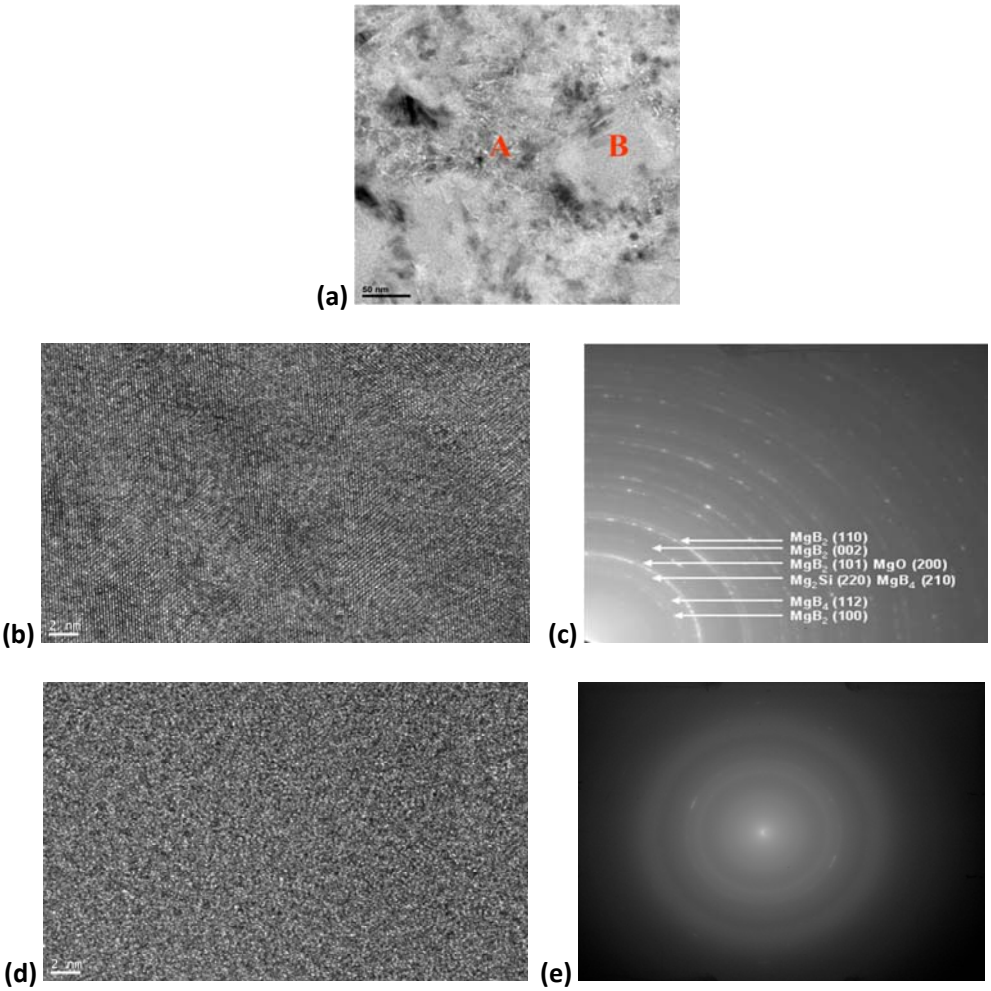

Fig. 4-7 (a) TEM image of IMD-processed mono-core MgB_2 wires with SiC addition, (b) high resolution image of region B in (a), (c) diffraction pattern of (b), (d) high resolution image of region C in (a), (e) diffraction pattern of (d)

Fig. 4-8 (a) and (b) show the TEM images, elemental maps by EDS and energy filtering image (EFI) of pure wires and SiC-added wires, respectively. The amorphous regions are proved to be the un-reacted B particles by EFI. This is consistent with the Fig. 4-6 and Fig. 4-7. The interesting point is that the oxide in the SiC-added wires seems to be more dispersed than that in the pure wires. Fig. 4-8 (c) and (d) show the schematic illustrations of the elemental distributions of pure wires and SiC-added wires, respectively. For pure wires, the MgO has a thin layer around MgB_2 grains, in which the un-reacted B particles can be also observed. While for the SiC-added wires, MgO with nano size is dispersed in the MgB_2 grains. The nano-sized MgO in SiC-added wires can work as flux pinning center to increase J_c, while the MgO thin layer in pure wires prevents the supercurrent. Dispersion of MgO in MgB_2 layer is one reason for the J_c enhancement of IMD-processed MgB_2 wires by SiC addition.

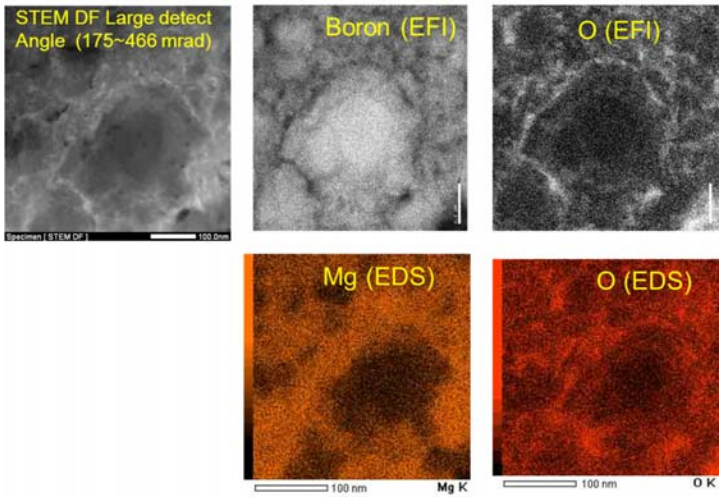

(a)

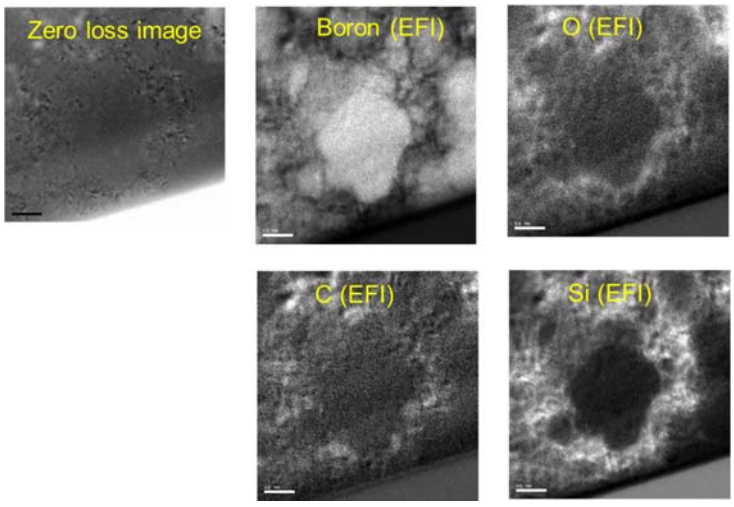

(b)

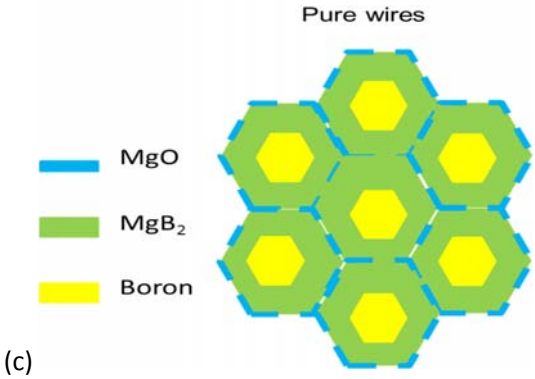

(c)

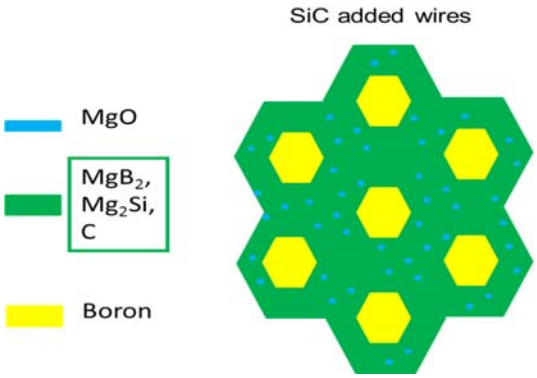

(d)

Fig. 4-8 Elemental maps by EDS and EFI of (a) pure wires and (b) SiC-added wires; the schematic illustrations of the elemental distributions of (c) pure wires and (d) SiC-added wires

4.4 Conclusions

The effect of the addition of both SiC and liquid aromatic hydrocarbon (toluene, *p*-ethyltoluene and *p*-dimethylbenzene) to the IMD-processed MgB_2 wires was investigated. The J_c properties are enhanced by co-addition of SiC with toluene and dimethylbenzene, but not so good for ethyltoluene. The highest J_e and J_c at 4.2 K and 10 T obtained in this work are 3,700 A/cm^2 and 48,000 A/cm^2, respectively, which were achieved for the SiC+dimethylbenzene co-added wires heat treated at 670℃ for 3 hours. The results indicate that the co-addition of SiC and liquid aromatic hydrocarbon is one of the promising methods to improve the J_c as well as J_e of the IMD processed MgB_2 wires.

I also studied the microstructure in order to investigate the mechanism of J_c enhancement. I observed the microstructures of the wires with SiC and/or toluene additives by TEM and SEM. The SiC and toluene co-addition increased the carbon substitution for B in the MgB_2 and the toluene addition decreased the grain size. They are considered to be mainly responsible for the J_c enhancement by the co-addition of SiC and toluene. Furthermore, I speculate that (a) the liquid hydrocarbon make the mixture of SiC and B powder uniform, (b) the absorbed liquid aromatic on the B surface prevent B absorbing oxide, and (c) the liquid aromatic hydrocarbon absorbed on the B surface also prevent the growth of MgB_2 grain. These are also considered to contribute to the J_c and J_e enhancements. I also discovered by TEM that SiC addition distributed oxides in MgB_2 layer. This discovery is useful to explain the J_c enhancement caused by SiC addition.

References

[1] Dou S X, Soltanian S, Horvat J, Wang X L, Zhou S H, Ionescu M and Liu H K 2002 *Appl. Phys. Lett.* 81 3419

[2] Kumakura H, Kitaguchi H, Matsumoto A and Hatakeyama H 2004 *Appl. Phys. Lett.* 84 3669

[3] Yamada H, Hirakawa M, Kumakura H and Kitaguchi H 2006 *Supercond. Sci. Technol.* 19 175

[4] Xu X, Kim J H, Yeoh W K, Zhang Y and Dou S X 2006 *Supercond. Sci. Technol.* 19 L47

[5] Hur J, Togano K, Matsumoto A, Kumakura H, Wada H and Kimura K 2008 *Supercond. Sci. Technol.* 21 032001

[6] Togano K, Hur J, Matsumoto A and Kumakura H 2009 *Supercond. Sci. Technol.* 22 015003

[7] Togano K, Hur J, Matsumoto A and Kumakura H 2010 *Supercond. Sci. Technol*. 23 085002

[8] Kumakura H, Hur J, Togano K, Matsumoto A, Wada H and Kimura K 2011 *IEEE Transactions on Applied Superconductivity* 21 2463

[9] Yamada H, Uchiyama N, Matsumoto A, Kitaguchi H and Kumakura H 2007 *Supercond. Sci. Technol.* 20 L30

[10] Yamada H, Igarashi M, Nemoto Y, Yamada Y, Tachikawa K, Kitaguchi H, Matsumoto A and H Kumakura 2010 *Supercond. Sci. Technol.* 23 045030

[11] Ye S J, Matsumoto A, Togano K and Kumakura H 2011 *Physica C* 471 1133

[12] Ye S J, Song M, Matsumoto A, Togano K, Takeguchi M, Kumakura H, Teranishi R and Kiyoshi T 2013 *Physica C* 484 167

[13] Matsumoto A, Kumakura H, Kitaguchi H, Senkowicz B J, Jewell M C, Hellstrom E E, Zhu Y, Voyles P M and Larbalestier D C 2006 *Appl. Phys. Lett.* 89 132508

[14] Lee S, Masui T, Yamamoto A, Uchiyama H and Tajima S 2003 *Physica C* 412 31

Chapter 5 Enhancement of J_c properties of MgB_2 wires by pretreating carbon-coated nano-sized B powder with Dimethylbenzene

5.1 Introduction

The quality of B powder is crucial to J_c of IMD-processed MgB_2 wires. The B powder I used in chapters 2-4 is not so good for its big size (325-mesh) and poor reactivity with Mg. In June of 2012, Li *et al*. [1] fabricated the IMD-processed MgB_2 wires (diameter: 0.55 mm) by using a special plasma-synthesized 2% carbon-coated B powder (Special Materials Inc., SMI B powder, particle size < 50 nm). And they obtained a high J_c of 1.07 x 10^5 A/cm^2 and a high engineering J_c (J_e) of 1.67 x 10^4 A/cm^2 at 4.2 K and 10 T for different samples.

I also tried this SMI B powder, however, I didn't obtain good results as theirs. After investigating the B powder, I found that many BCl_3 (source material for this B powder) exists in the B powder. Because dimethylbenzene is a good solvent for BCl_3, and our experiments in chapter 4 showed dimethylbenzene enhanced the J_c of IMD-processed MgB_2 wires, I pre-treated the SMI B with dimethylbenzene to remove BCl_3. I found the dimethylbenzene decreased the BCl_3 in B powder and then I obtained higher J_c values [2, 3]. The current transport properties and microstructures were investigated in this chapter. The details are described in my previous paper [3].

5.2 Experimental details

The following process (shown in Fig. 5-1) was carried out to remove residual BCl_3 from the SMI B powder. The powder was first ultrasonically mixed with C_8H_{10}, then the liquid was removed from the mixture by filtering, finally the remaining material was dried in a vacuum furnace at 100 °C. This powder is referred to SMI+D powder in this thesis.

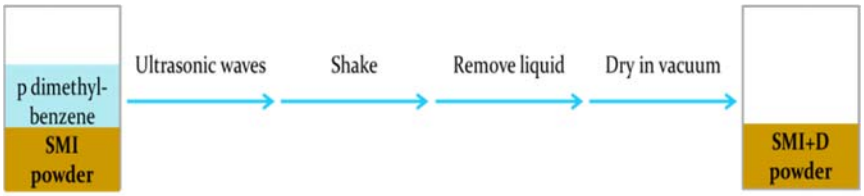

Fig. 5-1 The pretreating process for SMI B powder by dimethylbenzene

The SMI+D powder was used to fabricate wires using two kinds of metal sheathing tubes, made from Fe or Ta, with an outer diameter of 6 mm and an inner diameter of 4 mm. Details of the fabrication process have been previously reported [2-8]. Usually, the diameter of 2 mm Mg rod was used for the Fe-sheathed wire fabricated with SMI B powders, and full-reacted MgB_2 layer (with low MgB_2 area fraction) was formed without B-rich region. In this experiment, we also tried the 1.8 mm diameter Mg rod for Fe-sheathed wire in order to increase the thickness of MgB_2 layer and to obtain high J_e. The Mg rod with a diameter of either 2 mm or 1.8 mm was inserted along the center of the Fe tube, and B powder was packed into the intervening space in the air. The composite was groove-rolled and then drawn into a wire with a diameter of 0.6 mm. Wires formed using Mg rods with diameters of 2 mm and 1.8 mm are referred to as the Fe-SMI+D-1 and Fe-SMI+D-2 wires, respectively. For the Ta-sheathed wire, the composite was first groove-rolled and drawn into a wire with a diameter of 4 mm. This was then inserted into a Cu-Ni tube with an outer diameter of 6 mm and an inner diameter of 4 mm, which was groove-rolled and drawn into a wire with a diameter of 0.6 mm. This Ta-sheathed wire is referred to as the Ta-SMI+D wire. For comparison, an Fe-sheathed wire was also fabricated using the SMI powder, and this is referred to as the Fe-SMI wire. All the fabricated wires were heat treated at 675 °C for 8 h in an Ar gas flow, which is the same temperature used by Li *et al.* [1]. The temperature was ramped up to 675 °C over the course of 1 h, and after the heat treatment, the wires were cooled in the furnace.

The transport critical current (I_c) for the wires was measured at temperatures of 4.2, 10, 15, 20, 25, and 30 K in magnetic fields below 13 T using a four-probe resistance method. The value of J_c for each wire was calculated by dividing I_c by the whole MgB_2 area including B-rich region. The J_e was calculated by dividing I_c by the entire wire area in the transverse cross section.

Scanning electron microscopy (SEM) was carried out using a Hitachi SU-7. Energy dispersive X-ray spectroscopy (EDX) of powders was observed and analyzed by Genesis spectrum system of EDAX Inc., which is connected to SU-7. X-ray diffraction (XRD) analysis was carried out with Miniflex II of Rigaku. The TEM specimen was prepared using focused ion beam milling (JEOL JEM-FIB9320) and had a thickness of 100 nm. TEM and scanning TEM (STEM) observations were carried out using a JEOL JEM-2100F. Electron energy loss spectroscopy (EELS) images were obtained using a FEI Tecnai G2 F30.

5.3 Results and Discussion

5.3.1 Starting B powder

In this experiment, 4 mol% carbon-coated SMI B powder with nanometer-sized particles was first used in the IMD process. However, it was found that the MgB_2 wires fabricated using this powder exhibited a low critical current (I_c). An analysis of the powder indicated that it contained chlorine (Cl), which is thought to originate from the BCl_3 raw material used to produce the B powder. The SMI powder is produced using the following reaction [9]:

$$2\,BCl_3 + 3\,H_2 \xrightarrow{\text{RF plasma}} 2\,B + 6\,HCl$$

However, residual BCl_3 adsorbed on the powder particles can react with humidity when exposed to air, decreasing the quality of the power and resulting in a low critical current in the fabricated MgB_2 wires.

Fig. 5-2 show the XRD pattern of IMD-processed MgB_2 wires fabricated with SMI powder (left), and the images of IMD-processed MgB_2 wires before heat treatment fabricated with SMI and SMI+D powders (right). The BCl_3 absorbed the humidity in the air to form acid, which is considered to be the reason for the rust on the surface of Fe sheath.

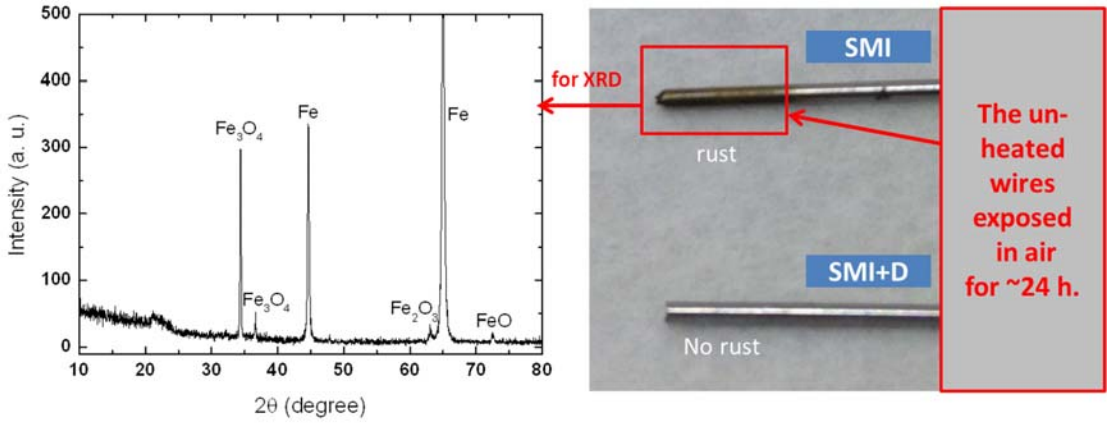

Fig. 5-2 The XRD pattern of IMD-processed MgB_2 wires before heat treatment fabricated with SMI powder (left), and the images of IMD-processed MgB_2 wires fabricated with SMI and SMI+D powders (right)

An elemental analysis of both the SMI and SMI+D powders was carried out using energy dispersive X-ray spectroscopy (EDX). As shown in Fig. 5-3, although both powders exhibited a Cl peak, its intensity relative to that of the main B peak was lower for the SMI+D powder. According to the manufacturer, the typical Cl content in SMI powder is from 0.5 to 1 at% [10]. The results of the elemental analysis are listed in table 5-1 for three different SMI and SMI+D powders (P1, P2, and P3). In table 5-1, the Cl content is likely to be highly over-estimated because the light elements B, C, and O are difficult to detect using EDX. However, the ratio of Cl to B is expected to be a good indicator of the relative Cl content of the different powders. From table 5-1, it can be seen that this ratio is consistently lower for the SMI+D powder, indicating that as expected, the pre-treatment with C_8H_{10} decreases the Cl content in the SMI powder.

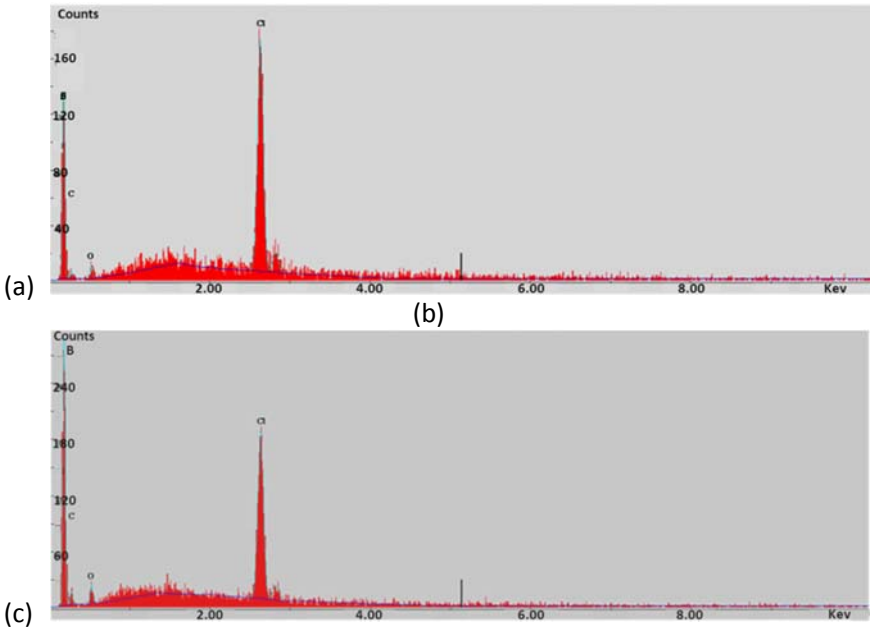

Fig. 5-3 EDX spectra of (a) SMI powder, and (b) SMI+D powder

Table 5-1. Compositions of SMI and SMI+D powders obtained from EDX analysis

Element (At%)	SMI-P1	SMI-P2	SMI-P3	SMI+D-P1	SMI+D-P2	SMI+D-P3
B K	72.48	74.19	71.01	74.05	75.46	75.66
C K	11.65	10.85	14.54	16.56	13.35	13.73
O K	4.94	4.91	4.09	3.61	4.71	4.74
Cl K	10.93	10.05	10.36	5.78	6.48	5.87

Scanning electron microscopy (SEM) was also carried out on the powder samples, and the results are shown in Fig. 5-4. It can be seen that the SMI+D powder (Fig. 5-4 (b)) is somewhat agglomerated, with the agglomerates being up to 15 μm in size. It was found that because of this agglomeration, the powder could be more easily packed into a metal tube than the SMI powder (Fig. 5-4 (a)).

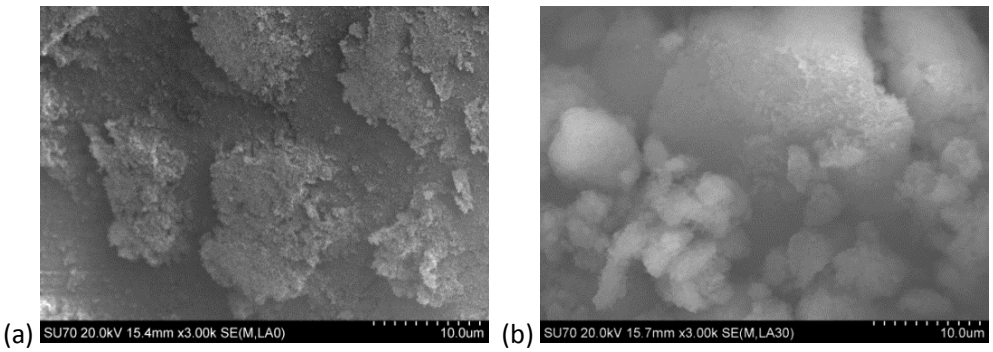

Fig. 5-4 SEM images of (a) SMI powder, and (b) SMI+D powder

5.3.2 Fabrication of wires

In this study, four kinds of wires with a diameter of 0.6 mm were fabricated using the IMD process. For two of the wires, SMI+D powder was used, together with a Mg rod with a diameter of either 2 mm or 1.8 mm and Fe sheath; these will henceforth be referred to as the Fe-SMI+D-1 and Fe-SMI+D-2 wires, respectively. In addition, a Ta-sheathed wire was produced using SMI+D powder (Ta-SMI+D) and a Fe-sheathed wire using SMI powder (Fe-SMI). Details of the fabrication process have been previously reported [2-8].

Fig. 5-5 (a-d) show transverse and longitudinal cross-sectional SEM images of the Ta-SMI+D and Fe-SMI+D-1 wires. For both types of wires, the MgB_2 layer thickness is fairly uniform due to almost complete reaction between the B and Mg. A hole is seen to run along the center of the wires, which in the case of the Fe-sheathed wire, is filled with some unreacted Mg and the resin used to mount the wires for SEM observations. The MgB_2 area fraction and the sheath area fraction for the wires fabricated in the present study are shown in table 5-2. The MgB_2 area fraction is about 7%, except for Fe-SMI+D-2, where it is 11.8% due to the smaller Mg rod diameter. The sheath area fraction for the Fe-sheathed wires is about 75%, while for the Ta-sheathed wire, the sheath (including the Cu-Ni and Ta) area fraction is about 85%. Fig. 5-5 (e, f) show transverse and longitudinal cross-sectional optical microscope images of Fig. 5-5 (c-d). The MgB_2 layer are orange color similar to Fig. 2-10(a), indicating that no B-rich region can be observed in the sample.

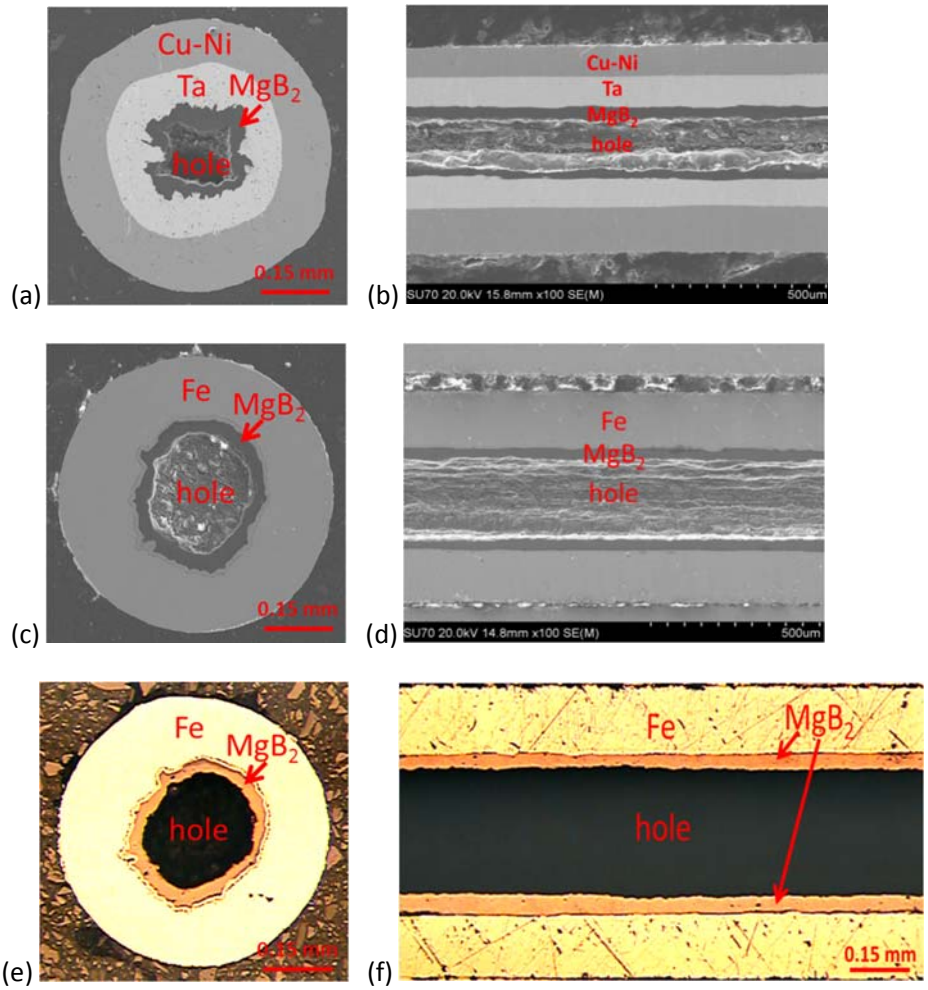

Fig. 5-5 Cross-sectional SEM images of (a), (b) Ta-SMI+D wire, and (c), (d) Fe-SMI+D-1wire, (e-f) optical microscope images of (c-d)

Table 5-2. MgB_2 area fraction and sheath area fraction for high-performance MgB_2 wires

IMD-processed MgB_2 wires	Ohio U. wire 1	Ohio U. wire 2	Ta-mono	Fe-mono -1	Fe-mono -2	Fe-mono
Starting powder	SMI		SMI+Dimethylbenzen			SMI
Heat treatment condition	675 ℃/0.5 h	675 ℃/8 h	675 ℃/8 h			
Diameter (mm)	0.55		0.6			
Sheath material	Inner: Nb, outer: monel		Inner: Ta, Outer: Cu-Ni	Fe		
Sheath area fraction (%)	67	65	85	76	75	78
MgB_2 area fraction (%)	10.1	18.8	7.1	7.0	11.8	6.9
J_c (A/cm²) @ 4.2 K & 10 T	1.07×10^5	0.93×10^5	1.19×10^5	1.15×10^5	0.83×10^5	0.68×10^5
J_e (A/cm²) @ 4.2 K & 10 T	0.97×10^4	1.67×10^4	0.84×10^4	0.81×10^4	0.98×10^4	0.48×10^4

X-ray diffraction (XRD) analysis was carried out for the Fe-SMI and Fe-SMI+D-1 wires as shown in Fig. 5-6. The a- and c-axis lattice parameters were determined from the MgB_2 (110) and MgB_2 (002) peaks in the XRD pattern, respectively. The amount of carbon substitution for boron, and the T_c value were then calculated from the lattice parameters based on the method of Lee *et al*. [11] The T_c value for these wires was also directly measured using a 4-probe method. The lattice parameters, amount of carbon substitution for boron, and calculated and measured T_c for the Fe-sheathed wires using SMI and SMI+D powders are summarized in table 5-3. The amount of C substitution for B (x in $Mg(B_{1-x}C_x)_2$) is 0.033 and 0.030 for the Fe-SMI and Fe-SMI+D-1 wires, respectively. This suggests that the C_8H_{10} has little influence on C substitution for B, and hence on T_c. The measured T_c values are seen to be consistent with the calculated values.

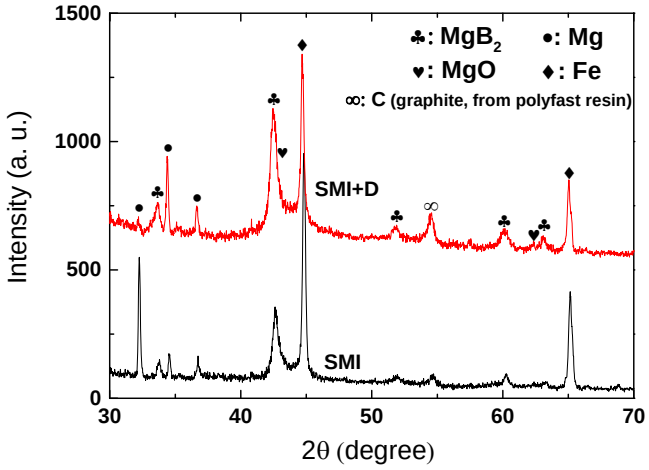

Fig. 5-6 X-ray diffraction (XRD) patterns for the Fe-SMI and Fe-SMI+D-1 wires

Table 5-3. Lattice parameters, amount of carbon substitution for boron, and calculated and measured T_c for Fe-sheathed wires using fabricated SMI and SMI+D powders

	a-axis (Å)	c-axis (Å)	X in $Mg(B_{1-x}C_x)_2$	Calculated T_c (K)	Measured T_c (K)
Fe-SMI	3.071917	3.516894	0.033	33.2	33
Fe-SMI+D-1	3.073768	3.520671	0.030	33.7	33.2

5.3.3 Critical current properties

Fig. 5-7(a) and (b) show the J_c-B and J_e-B curves, respectively, for the different wires. Data for the high-J_c wire (B1) and high-J_e wire (B3) obtained by Li *et al*. [1] are also included for comparison. For all the wires fabricated in the present study, the J_c-B curves have similar slopes, suggesting a similar amount of C substitution for B, which is consistent with the results shown in table 5-3. The Ta-SMI+D and Fe-SMI+D-1 wires both show excellent J_c values. The J_c value for the Ta-SMI+D wire at 10 T and 4.2 K is about 1.2 x 10^5 A/cm^2, which is the highest J_c reported for MgB_2 wires. However, all of the J_e values are lower than the highest value obtained by Li *et al*. [1] (about 1.67 x 10^4 A/cm^2). For the wires fabricated in the present study, the highest J_e value is about 1 x 10^4 A/cm^2 for Fe-SMI+D-2. However, the J_c value for Fe-SMI+D-2 is lower than that for Fe-SMI+D-1, which is due to the presence of less Mg. Thus, some B-rich region remained and decreased J_c. As shown in table 5-2**,** the wires fabricated in the present study had a higher sheath area fraction and a smaller MgB_2 area fraction than those fabricated by Li *et al*. [1]. Decreasing the sheath area fraction by the use of a thin metal tube and increasing the MgB_2 area fraction by optimizing the starting B layer could therefore lead to an increase in J_e. The wires fabricated using the SMI+D powder have higher J_c and J_e than those fabricated using the SMI powder. The SMI powder is so fine that it is not easy to insert it into the space between the Mg rod (diameter: 2 mm) and the sheath (inner diameter: 4 mm). This leads to a lower-density B layer and consequently a lower J_c and J_e. Since the addition of C_8H_{10} causes agglomeration of the powder particles and makes the powder easier to be packed, the B layer density becomes higher. Another reason for the higher J_c for the SMI+D wires may be the reduced amount of Cl, although the mechanism is unclear at present.

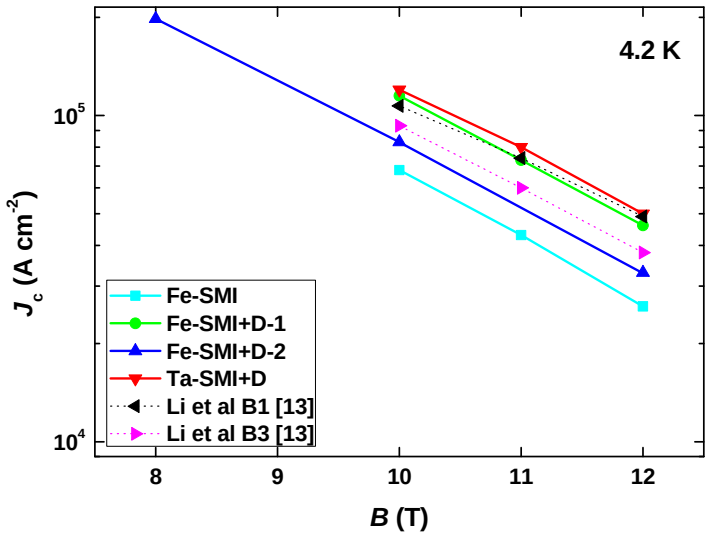

(a)

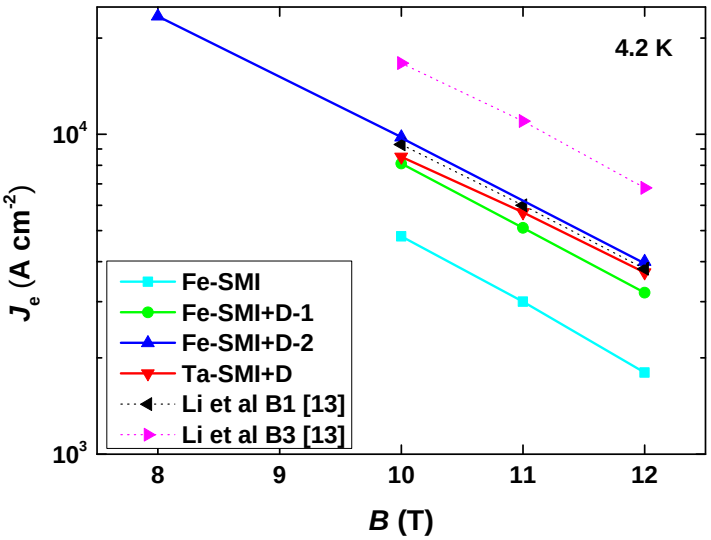

(b)

Fig. 5-7 Comparison of (a) J_c-B, and (b) J_e-B curves for IMD-processed MgB_2 wires at 4.2 K

(Specification of the samples are listed in table 5-2)

Fig. 5-8 shows the measured J_c and J_e values for the Fe-SMI+D-1 wire at different temperatures and magnetic fields. For comparison, the results for Ta-sheathed 7-core (Ta-7) wires previously fabricated with high-quality B powder and added SiC [7, 8] are shown by the dotted lines. In Fig. 5-8(a), the J_c-B curve for the most commonly used Nb-Ti metallic superconducting wire [12] is also shown by a dotted line. The slope of the J_c-B curve for the Fe-SMI+D-1 wire is seen to be lower than that for the Ta-7 wire at both 4.2 and 20 K. This is due to the fact that the Ta-7 wire had more carbon substitution (x = 0.1 in $Mg(B_{1-x}C_x)_2$) [7, 8] for boron than the Fe-SMI+D-1 wire (x = 0.03). At 20 K, the Fe-SMI+D-1 wire exhibits a higher J_c at fields below 6 T. At 20 K and 5 T, the J_c value for the Fe-SMI+D-1 wire is 7.6 x 10^4 A/cm^2, which is higher than the value of 5 x 10^4 A/cm^2 for the Ta-7 wire. It is also the highest value ever reported for MgB_2 wires. At 10 K, the J_c values for the wires fabricated in the present study are higher than that for Nb-Ti wires at 4.2 K in the magnetic fields at which the measurements were carried out. Fig. 5-8(b) shows the J_e-B curve for the Fe-SMI+D-1 wire, with the Ta-7 wire shown for comparison. The J_e of Nb-Ti metallic superconducting wire is not shown because the paper we refereed [12] has no J_e data. The J_e value for the Fe-SMI+D-1 wire is about 5.3 x 10^3 A/cm^2 at 20 K and 5 T, which is almost 3 times higher than the value of 1.8 x 10^3 A/cm^2 for the Ta-7 wire. In addition, a J_e value higher than 2 x 10^4 A/cm^2 could be speculated at 15 K and 5 T, which is already acceptable for applications such as magnetic resonance imaging [13] and maglev trains. Thus, IMD-processed MgB_2 wire is a promising candidate for such applications under liquid-helium-free conditions.

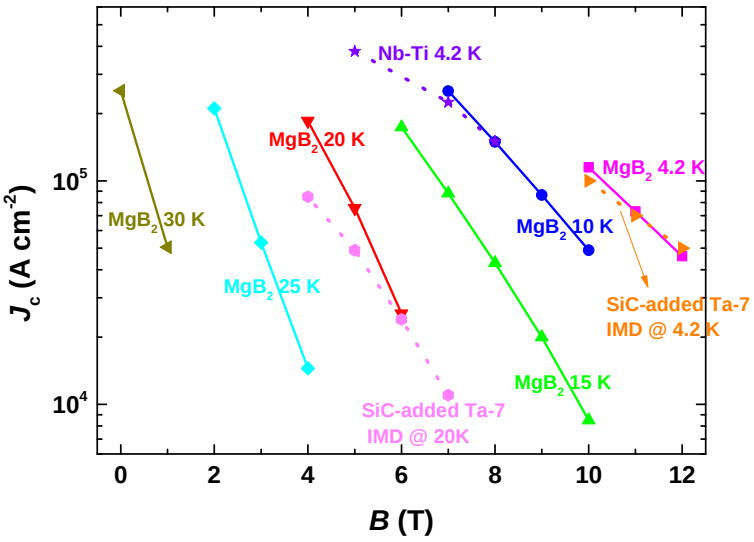

(a)

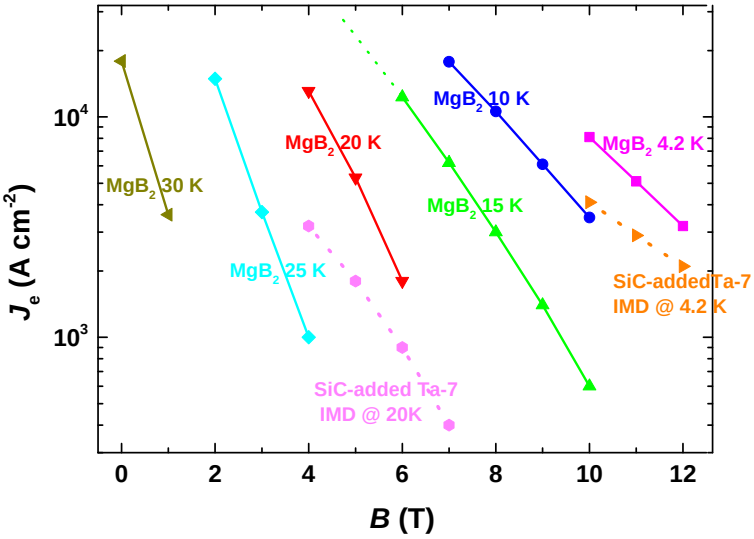

(b)

Fig. 5-8 (a) J_c-B curves and (b) J_e-B curves for IMD-processed MgB_2 wire (Fe-SMI+D-1) at different temperatures. Previously reported data for Ta-sheathed wire fabricated using SiC addition [7, 8], and J_c data for Nb-Ti wires [12] are shown using dotted lines

5.3.4 Scanning electron microscopy analysis

Fig. 5-9 (a) and (b) show SEM images of the longitudinal cross section of the MgB_2 layer in the Fe-SMI wire at magnifications of 30k and 80k, respectively. High density MgB_2 layer can be observed from the SEM images. A large number of bright spots can be seen against the darker background. Fig. 5-9 (c) shows EDS maps of the area seen in Fig. 5-9 (a), which indicate that the bright spots correspond to MgO. The distribution of MgO is not uniform. It can also be seen that voids with sizes of less than 100 nm (indicated by red ellipses) exist near the MgO in Fig. 5-9 (a) and (b), although the reason why the MgO and void regions are associated with each other is at present unclear. MgO is mainly considered to be the product of Mg and B_2O_3, and there are mainly two reasons why the B_2O_3 exists: one is because B powder has oxide as shown in table 5-1, another may be due to the oxidation of nano-sized B powder during its packing in the air. These voids are thought to be the result of the poor packing of the SMI powder in the space between the Mg and the sheath. Fig. 5-9 (d) and (e) show SEM images of the longitudinal cross section of the MgB_2 layer in the Fe-SMI+D-1 wire at magnifications of 30k and 80k, respectively. MgO is also seen to be present in this wire. Although from the SEM images, it is not easy to directly compare the amount of MgO in the two types of wire, the number of voids is less for the Fe-SMI+D-1 wire and the void size is smaller. This is considered to be due to the C_8H_{10} pre-treatment, and results in a higher J_c and J_e. Fig. 5-9 (f) and (g) show SEM images of the Ta-SMI+D wire. Although the amount of MgO appears comparable to that for the Fe-SMI and Fe-SMI+D-1 wires, almost no voids can be seen. This is consistent with our previous findings that a higher density MgB_2 layer was obtained with a Ta sheath than with an Fe sheath [7, 8].

(a) 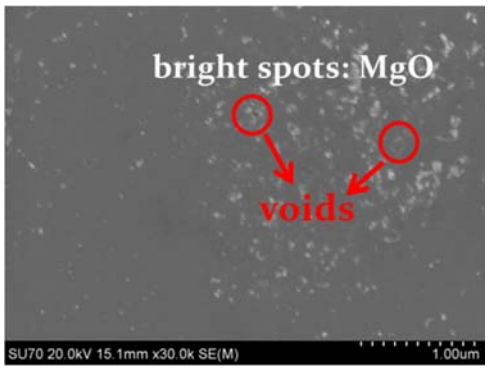

(b) 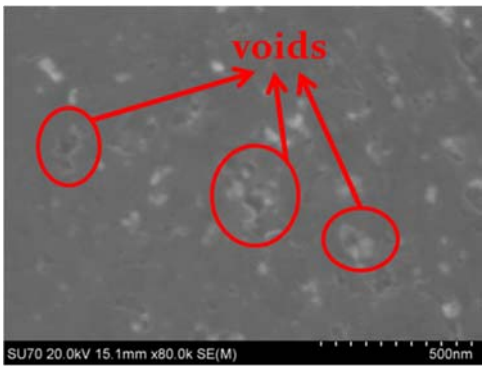

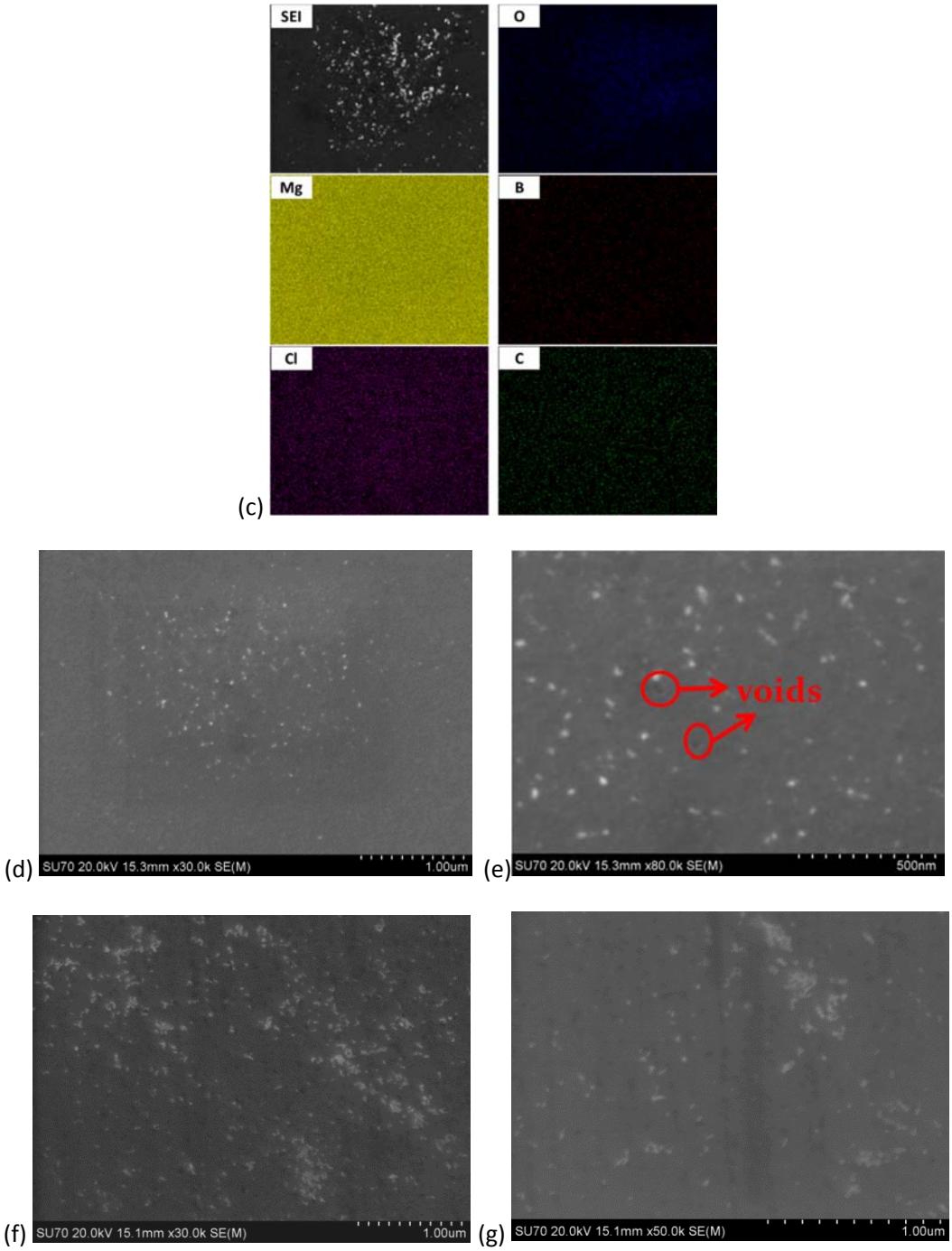

Fig. 5-9 SEM images of Fe-SMI wire at magnification of (a) 30k, and (b) 80k times, and (c) EDX maps corresponding to the area shown in (a). SEM images of Fe-SMI+D-1 wire at magnification of (d) 30k and (e) 80k times. SEM images of Ta-SMI+D wire at magnification of (f) 30k and (g) 50k times

5.3.5 Transmission electron microscopy analysis

Although the J_c value is strongly dependent on the density of the MgB_2 layer and the level of impurities present, the nanoscale microstructure is also expected to have an important influence. Therefore, a transmission electron microscopy (TEM) analysis was carried out on the MgB_2 layer in the Ta-SMI+D wire that exhibited the highest J_c value.

Fig. 5-10(a) shows a dark-field scanning TEM (STEM) image taken at a magnification of 25k and a camera length of 20 cm, in which the MgB_2 layer is seen to be uniform with a grain size of less than 100 nm. This small grain size is expected to lead to considerable flux pinning at grain boundaries. The regions labeled R1, R2, and R3 were then selected for more detailed analysis. Fig. 5-10(b) shows an image of region R1, taken at a magnification of 250k and a camera length of 20 cm. It can be seen that there are many grains with sizes less than 20 nm, as indicated by the red ellipses. Again, these are expected to act as effective flux pinning centers.

Fig. 5-10(c) and (d) show a bright-field image (300k and camera length 80 cm) and the corresponding dark-field image (300k and camera length 40 cm) of region R2, respectively. Five regions, labeled A to E, were selected for high-resolution imaging at 800K. The resulting images are shown in Fig. 5-10(e), where the insets represent electron diffraction patterns obtained by applying a fast Fourier transform (FFT) to the corresponding images. The layer was found to be mainly composed of MgB_2, with some MgO also being present, which is consistent with the SEM results.

Fig. 5-10(f) shows electron energy loss spectroscopy (EELS) elemental images obtained from region R3, together with a STEM-high-angle-annular-dark-field (STEM-HAADF) image for comparison. The red circles indicate MgO particles with sizes of less than 50 nm. Unreacted B particles can be also found, as indicated by the green rectangles. Since both types of particles would act as barriers to the superconducting current, it is expected that the J_c value could be increased by reducing their number. The MgO particles originate mainly from the starting B powder, so their number could be reduced by refining the powder. One way of reducing the number of unreacted B particles would be to shorten the Mg diffusion distance, which could be achieved by reducing the MgB_2 layer thickness and fabricating multi-filament wires.

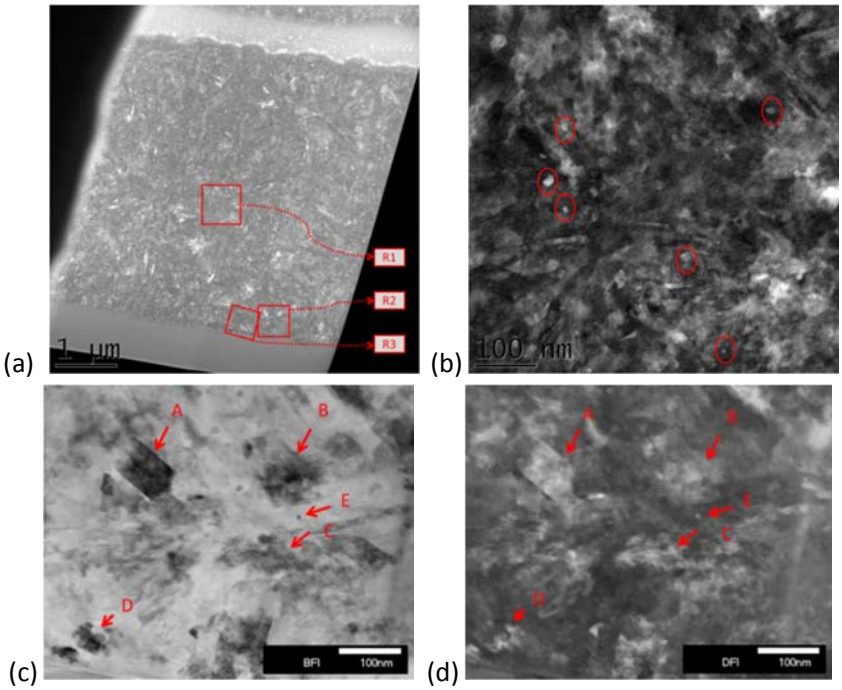
(a)
R1
R2
R3
1 μm
(b)
100 nm
(c)
A
B
E
C
D
BFI
100nm
(d)
A
B
E
C
D
DFI
100nm

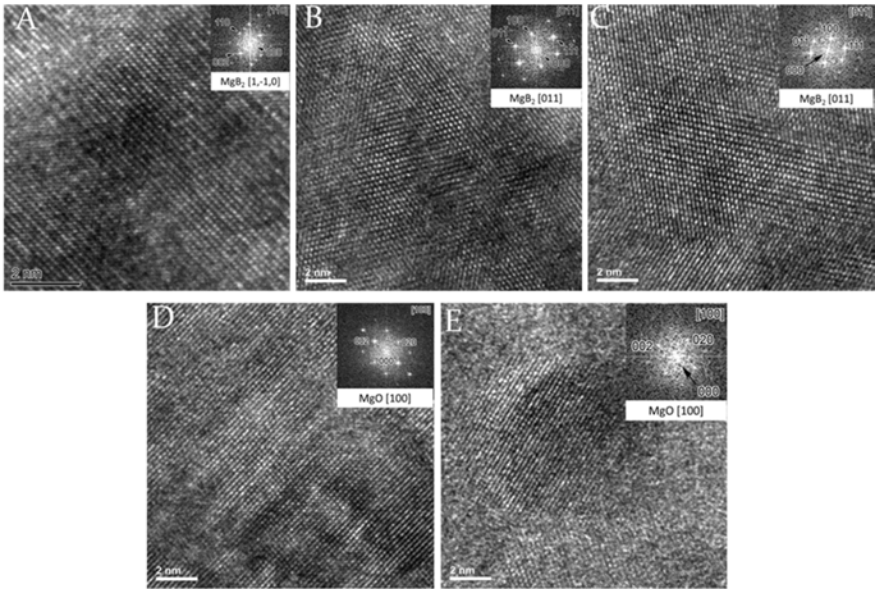
A
MgB2 [1,-1,0]
B
MgB2 [011]
C
MgB2 [011]
D
MgO [100]
E
MgO [100]

(e)

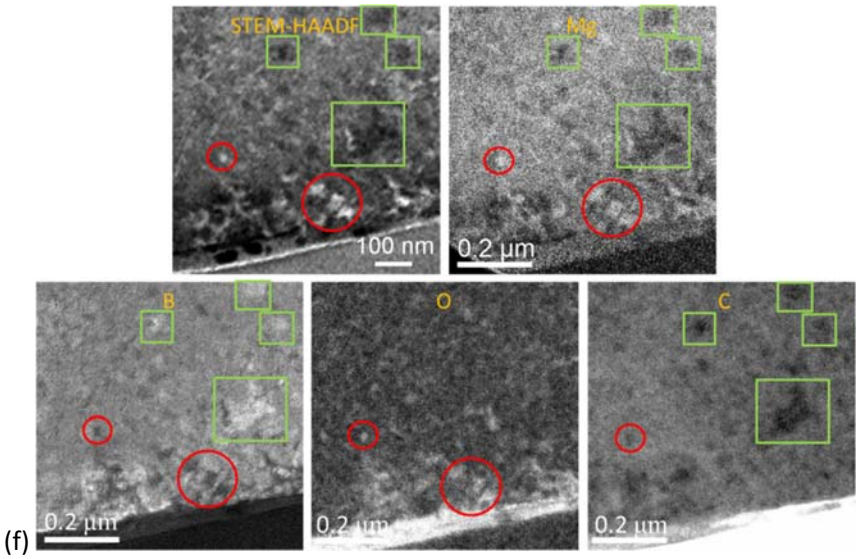

Fig. 5-10 (a) STEM dark-field image of Ta-SMI+D wire at 25k times magnification and camera length of 20 cm, (b) STEM dark-field image of region R1 in (a) at 250k times magnification and camera length of 20 cm, (c) STEM bright-field image of region R2 in (a) at 300k times magnification and camera length of 80 cm, (d) STEM dark-field image of region R2 in (a) at 300k times magnification and camera length of 80 cm, (e) high resolution images (800k) and corresponding fast Fourier transforms (FFT) of regions A to E in (c) and (d), and (f) electron energy loss spectroscopy (EELS) images of region R3 in (a)

The TEM results thus indicate that the MgB_2 layer is composed of small MgB_2 grains, mostly with sizes less than 100 nm, together with small MgO and unreacted B particles. However, similar grain sizes were also found for IMD-processed MgB_2 wires using SiC and Mg co-additives and a different type of B powder (99%, 325-mesh), for which a lower J_c value of 5 x 10^4 A/cm^2 at 10 T and 4.2 K was obtained, as has been previously reported [14]. Thus, one reason for the higher J_c obtained in the present study is thought to be the lower concentration of unreacted B particles in the MgB_2 layer. PIT-processed wires with much lower MgB_2 filling factors also exhibited similar grain sizes, despite the considerably lower J_c values [15]. The results of the present study suggest that the most effective approach to obtaining a high J_c is to produce a high-density MgB_2 layer with few voids and unreacted B particles, by suitable treatment of the wire and by ensuring a short Mg diffusion distance by producing thinner wires.

5.4 Conclusions

High-performance MgB_2 wires with diameters of 0.6 mm were fabricated using the IMD process. Pre-treatment of carbon-coated B powder with nanometer-sized particles using C_8H_{10} was found to lead to an increase in the critical current. The C_8H_{10} is thought to decrease the amount of Cl in the powder and increase the B packing density, which has a significant positive influence on the critical current.

For both Ta- and Fe-sheathed wires, the highest J_c value was about 1.2 x 10^5 A/cm^2 at 4.2 K and 10 T, and the J_e value was about 1 x 10^4 A/cm^2. The Fe-SMI+D-1 wire exhibited a J_c of 7.6 x 10^4 A/cm^2 and a J_e of 5.3 x 10^3 A/cm^2 at 20 K and 5 T, which are the highest values reported for MgB_2 wires to date. At 10 K, the J_c value for the wires fabricated in the present study was actually higher than that for Nb-Ti wires at 4.2 K for the magnetic fields at which the measurements were carried out.

The MgB_2 layer in the wire that exhibited the highest J_c value was found (by SEM and TEM) to be uniform and contain small grains, almost all less than 100 nm, and many less than 20 nm. Small amounts of unreacted B particles were also present in the layer. Although a similar small grain structure was found in previous IMD- and PIT-processed MgB_2 wires, they exhibited lower J_c values. Thus, the high density of the MgB_2 layer and the presence of fewer and smaller unreacted B particles are considered to be the main reasons for the large critical current obtained in the present study. Further increases in the J_c and J_e values could be achieved by decreasing the MgO (in size and in amounts), voids and unreacted B particles. The J_e value could also be increased by increasing the MgB_2 area fraction.

This study indicate that IMD-processed MgB_2 wires are promising superconductors for applications such as magnetic resonance imaging and maglev trains that can operate under liquid-helium-free conditions. The BCl_3 exists in SMI B powder, and the carbon-coating process by mixing the BCl_3, H_2, and CH_4 in RF plasma are difficult to control. These make SMI B powder not suitable for fabrication of long wires for large-scale practical applications. In chapter 6, I tried a new B powder and a new carbon-coating process.

References

[1] Li G Z, Sumption M D, Susner M A, Yang Y, Reddy K M, Rindfleisch M A, Tomsic M J, Thong C J and Collings E W 2012 *Supercond. Sci. Technol.* 25 115023

[2] Ye S J, Matsumoto A, Togano K, Zhang Y, Kumakura H, Song M, Teranishi R and Kiyoshi T 2012 *prestention of ASC2012* 1MB-01

[3] Ye S J, Song M, Matsumoto A, Togano K, Takeguchi M, Ohmura T and Kumakura H 2013 *Supercond. Sci. Technol*. 26 125003

[4] Hur J, Togano K, Matsumoto A, Kumakura H, Wada H and Kimura K 2008 *Supercond. Sci. Technol.* 21 032001

[5] Ye S J, Matsumoto A, Togano K and Kumakura H 2011 *Physica C* 471 1133

[6] Ye S J, Song M, Matsumoto A, Togano K, Takeguchi M, Kumakura H, Teranishi R and Kiyoshi T 2013 *Physica C* 484 167

[7] Togano K, Hur J, Matsumoto A and Kumakura H 2010 *Supercond. Sci. Technol.* 23 085002

[8] Kumakura H, Hur J, Togano K, Matsumoto A, Wada H and Kimura K 2011 *IEEE Trans. Appl. Supercond.* 21 2463

[9] Susner M A, Yang Y, Sumption M D, Collings E W, Rindfleisch M A, Tomsic M J and Marzik J V 2011 *Supercond. Sci. Technol*. 24 012001

[10] Private communication with Dr. James. V. Marzik of Specialty Materials, Inc.

[11] Lee S, Masui T, Yamamoto A, Uchiyama H and Tajima S 2003 *Physica C* 412 31

[12] Hong S, Geschwindner D, Mantone A, Marancik W, Zalek S and Zhou R 1989 *IEEE Transactions on Applied magnetics* 25 1934

[13]http://ir.bruker.com/phoenix.zhtml?c=121496&p=irol-ewsArticle&ID=1362507&hi

[14] Ye S J, Song M, Matsumoto A, Togano K, Zhang Y, Kumakura H, Takeguchi M, Teranishi R and Kiyoshi T 2012 *Supercond. Sci. Technol.* 25 125014

[15] Zhu Y, Matsumoto A, Senkowicz B J, Kumakura H, Kitaguchi H, Jewell M C, Hellstrom E E, Larbalestier D C and Voyles P M 2007 *Journal of Applied Physics* 102 013913

Chapter 6 Enhancement of critical current properties of MgB_2 wires by aromatic hydrocarbon ($C_{24}H_{12}$) addition

6.1 Introduction

In chapter 5, I introduced that high critical current properties can be obtained for IMD-processed MgB_2 wires by using nano-sized carbon-coated B powder (SMI B, particle size < 50 nm) [1-3]. The use of nano-sized B powder produced high density MgB_2 layer with less voids and less un-reacted B particles. This is mainly responsible for the high critical current properties we obtained. However, the SMI B powder is produced with a complex plasma spray synthesis process [4]. For this process, the BCl_3 gas and H_2 gas are injected into RF plasma to form nano-sized amorphous B powder. The BCl_3 is easily adsorbed on the surface of nano-sized B, which make the B powder unstable (BCl_3 is highly reactive with moisture) as mentioned in chapter 5. The pretreatment of SMI B powder by dimethylbenzene can decrease BCl_3, and thus increases the critical current properties [2, 3]. But the BCl_3 still exists in the B powder even after the pretreatment by dimethylbenzene. This unstable B powder increases the risk of non-uniformity of critical current properties during the fabrication process of MgB_2 wires for large-scale applications. Furthermore, the C-coating on B powder is through the injection of CH_4 into the plasma [4]. This process is very difficult to control the amount of carbon-coating. In addition, about 0.5%~1.0% B oxide exists in this B powder.

In this chapter, firstly, I changed SMI B powder for a new one. The new B powder is produced by a Turkey company. The B powder is synthesized from the following process:

$$B_2H_6 \xrightarrow{\triangle} 2B + 3H_2$$

The B powder has a particle size of less than 250 nm that is bigger than that of SMI B powder (less than 50 nm). The purity is 98.5 %, which is almost the same as the SMI B powder but no BCl_3 exists in the new B powder.

Secondly, I used the coronene ($C_{24}H_{12}$) as the carbon source. Coronene is the polycyclic aromatic hydrocarbon comprising six peri-fused benzene rings as shown in Fig. 6-1. The carbon content in the coronene molecule reaches 96 wt%. The structure of six peri-fused benzene rings has the highest symmetry of all organics expect benzene. The high symmetry indicates that its

decomposed products are uniform. The coronene decomposes at about 600 °C [5]. The reaction between Mg and B for both IMD and PIT processes also occurs at about 600 °C. Therefore, we can expect that carbon atoms in coronene effectively substitute for B. Furthermore, the coronene is no toxic and abundantly exists in sedimentary rock. All these advantages suggest that coronene is a good candidate as a carbon additive for MgB_2 superconducting wires.

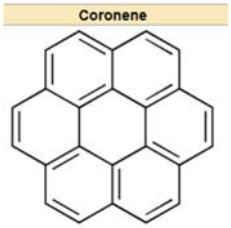

Fig. 6-1 Molecule structure of coronene ($C_{24}H_{12}$)

In this study, I applied the coronene addition to the fabrication of MgB_2 wires with both IMD and PIT processes. The critical current properties and microstructures were investigated for these wires [6].

6.2 Experimental details

Both IMD- and PIT-processed MgB_2 wires are fabricated with the same methods as introduced in our previous paper [7-12]. B powders for both IMD and PIT process are obtained from a Turkey company as introduced above. The coarse Mg powder with size of 100~600 μm is used for PIT process. The diameter of PIT wire is 1.0 mm. The 2%, 5%, and 10% coronene-added wires are fabricated. Undoped wires are also fabricated for comparison. All the PIT wires are heat treated at 700 °C for 1 hour.

The diameter of IMD wires is 0.6 mm. The reason of the use of small diameter for IMD wire is to decrease the Mg diffusion distance as introduced in chapter 5. The undoped, 5 mol% coronene-added, and 10 mol% SiC-added wires are fabricated. Fe tube with inner diameter of 4 mm and outer diameter of 6 mm are used as sheath. The diameters of Mg rod for all wires are 2 mm. I also changed the diameter of Mg rod to 1.8 mm for one coronene-added wire (termed $C_{24}H_{12}$ 5% 1) as described in chapter 5. Furthermore, several wires are also fabricated using dimethylbenzene-pretreated SMI B powder (same as in chapter 5) for comparison. All the IMD-processed MgB_2 wires are heat treated at 670 °C for 6 hours.

6.3 Results and discussion

Fig. 6-2 (a) shows an optical microscope image on transverse cross section of the PIT-processed MgB_2 wires (diameter: 1.0 mm). MgB_2 core can be found in the Fe sheath. The orange region is the high density MgB_2 layer, while the black region is voids. Fig. 6-2 (b) shows SEM image on the longitudinal cross section of the PIT-processed MgB_2 wires. The textured MgB_2 can be found in the wire direction, which is because the coarse Mg powders were elongated during the wire drawing. If a void is elongated in one direction, the void area in perpendicular direction could be decreased because the volume of voids that is caused by the reaction between Mg and B powders is fixed. I considered that the structure (elongated voids in wire direction) shown in Fig. 6-2(b) can enhance the critical current properties of MgB_2 wires because it decreases the voids in transverse cross section of the wire.

(a) 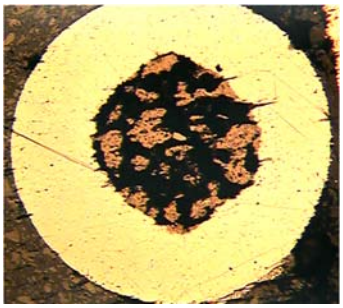 (b) 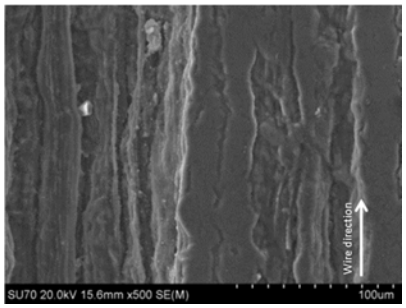

Fig. 6-2 Transverse cross sectional image observed by optical microscope (a), and longitudinal cross sectional image observed by SEM (b) of PIT-processed MgB_2 wires (diameter: 1.0 mm)

Fig. 6-3 (a) shows the J_c-B curves of PIT-processed MgB_2 wires at 4.2 K. The undoped, 2%, 5%, and 10% coronene-added wires are compared. The highest J_c values are obtained by the 10% coronene-added wires. The J_c achieves 1.8 x 10^4 A/cm^2 at 4.2 K and 10 T, which is fairly high for PIT-processed MgB_2 wires. As we know, the slope of J_c-B curves can be used to estimate the amount of C substitution for B site in MgB_2 wires. The slope of J_c-B curves of 2% addition is lower than that of undoped wire, while higher than that of 5% coronene-added wire. But there is no big difference between 5% and 10% addition. The less addition (undoped and 2%) show higher J_c properties when we extrapolate the J_c-B curves to low fields. We should optimize the amounts of coronene addition taking into account of the magnetic field where we use this conductor. The amount of carbon addition can be easily controlled by the amount of coronene addition, while that of carbon-coated SMI B powder is difficult to control due to the plasma process. Fig. 6-3 (b) shows the J_e-B curves of PIT-processed MgB_2 wires at 4.2 K. The J_e of 4.9 x 10^3 A/cm^2 at 4.2 K and

10 T was obtained by 10% coronene-added wire. The dependence of J_c-B and J_e-B curves on the amount of coronene addition is almost the same because the MgB_2 area fraction is similar for all wires due to the same wire fabrication process.

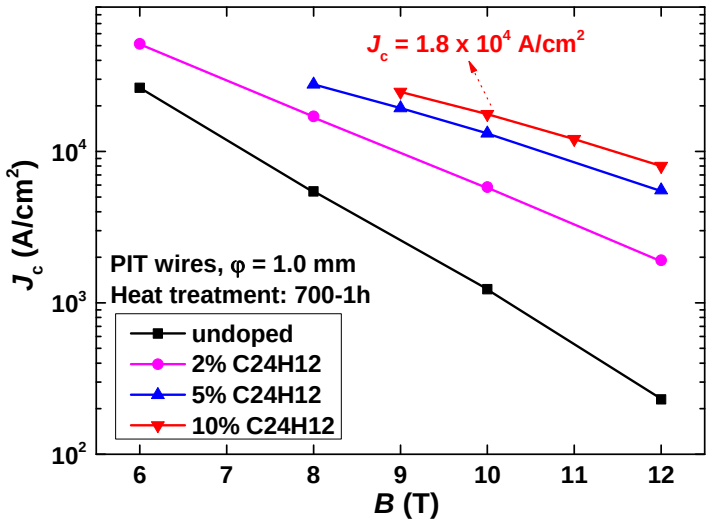

(a)

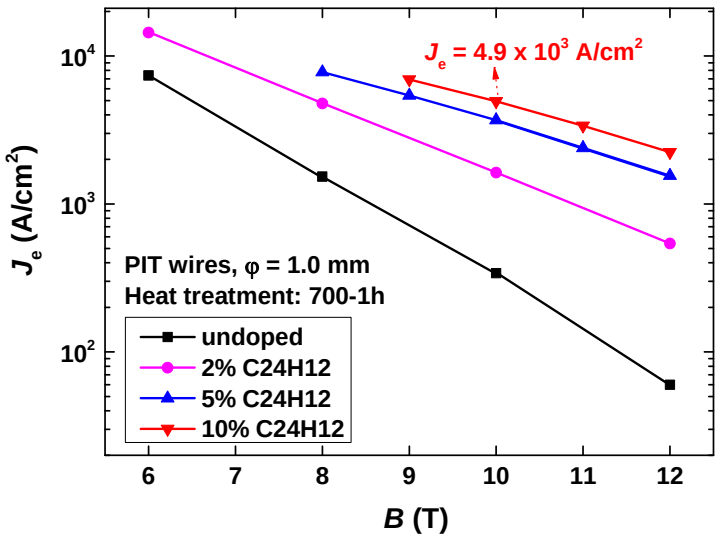

(b)

Fig. 6-3 (a) J_c-B curves, and (b) J_e-B curves of PIT-processed MgB_2 wires at 4.2 K

Fig. 6-4 shows X-ray diffraction patterns of PIT-processed MgB_2 wires. The amount of carbon substitution for B and T_c both calculated from MgB_2 110 peak according to Wilke *et al*'s method [13] are shown in table 6-1. The amount of carbon substitution for B is 4.5% for 5 % coronene-added wires, while 4.8% for 10% coronene-added wires. This suggests that the excess coronene addition (10%) has little influence on the increase of the carbon substitution for B, which is consistent of the slopes of J_c-B curves in Fig. 6-3. The 10% coronene-added MgB_2 wire has higher J_c than that of 5% coronene-added wire, though they have similar amount of carbon substation for B. This may be due to that the excess carbon in 10% coronene-added wire works as the flux pinning center to enhance the J_c values. The T_c values measured by resistivity method are also shown. The differences of T_c values between measured and calculated are larger for undoped and 2% coronene-added wires, while smaller for 5% and 10% coronene-added wires. This may be because the impurity in B powder (<1.5%) also decreases the T_c. This impurity effect is not considered in Wilke *et al* 's method.

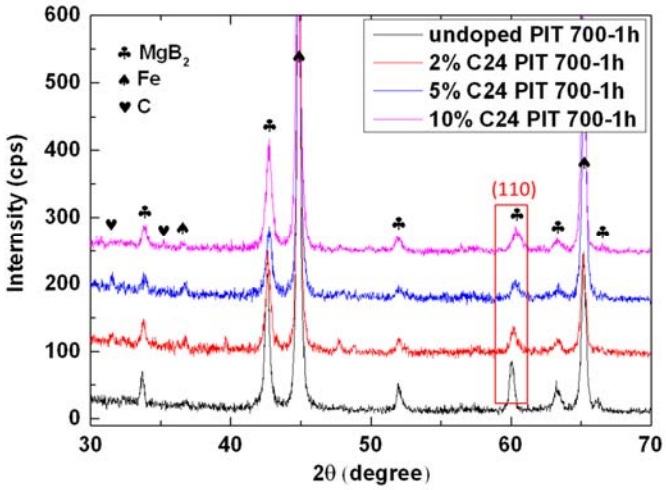

Fig. 6-4 X-ray diffraction patterns of PIT-processed MgB_2 wires

Table 6-1 The properties of PIT-processed MgB_2 wires in this experiment

	Delta a (A)	X in $Mg(B_{1-x}C_x)_2$	Calculated T_c (K) * reference [13]	Measured T_c (K) by resistivity
undoped	**-**	**-**	**38.8**	**38**
2% C24H12	**0.005**	**0.016**	**38**	**36.9**
5% C24H12	**0.014**	**0.045**	**35**	**35.1**
10% C24H12	**0.015**	**0.048**	**34.4**	**34.2**

Fig. 6-5 shows the SEM images of (a) undoped, (b) 2%, (c) 5%, and (d) 10% coronene-added PIT-processed MgB_2 wires. These images are observed in the longitudinal cross section. It is difficult to see the big difference between the undoped wires (a) and coronene-added wires (b-d).

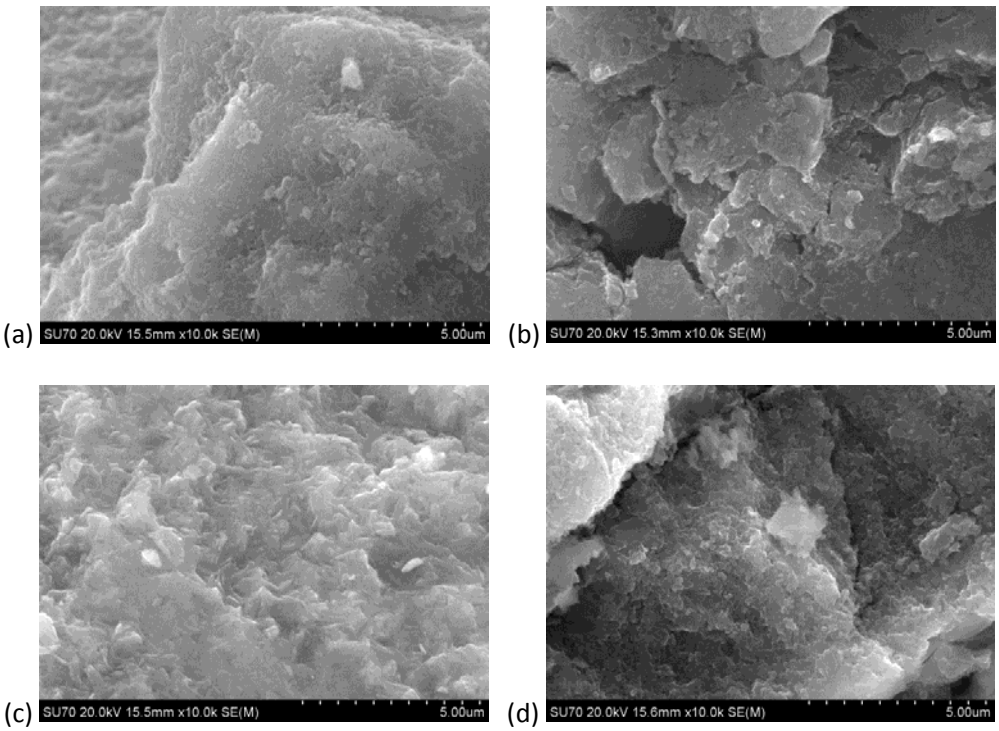

Fig. 6-5 SEM images of (a) undoped, (b) 2%, (c) 5%, and (d) 10% coronene-added PIT-processed MgB_2 wires

Fig. 6-6 shows an optical microscope image on the transverse cross section of the IMD-processed MgB_2 wires (diameter: 0.6 mm). The MgB_2 layer is formed uniformly in the inner wall of Fe sheath with a hole in the wire center. The orange color of reacted layer is due to that the high density MgB_2 reflects light, which is similar to Fig. 2-10 in chapter 2. On the other hand, PIT-processed MgB_2 layer shown in Fig. 6-2 are dark or dark orange is due to the voids in MgB_2 layer absorb light.

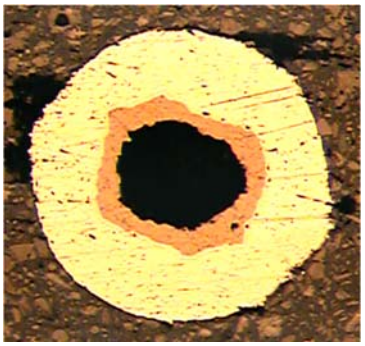

Fig. 6-6 Optical microscope image on the transverse cross section of the IMD-processed MgB_2 wires (diameter: 0.6 mm)

Fig. 6-7 shows (a) J_c-B curves, and (b) J_e-B curves for IMD-processed MgB_2 wires fabricated in this experiment. Two coronene-added MgB_2 wires are shown in Fig. 6-7(a). The J_c of the wires fabricated with dimethylbenzene-pretreated SMI B powder (SMI+D) are also included in the figure. The difference of two wires is a small difference of Mg rod diameter. This change of rod diameter is also introduced in chapter 5. The lower J_c of SMI+D wires obtained in this chapter is due to the different heat treatment conditions. In this chapter, the wire is heat treated at 670 °C for 6 hours, while at 675 °C for 8 hours in chapter 5. The high J_c value of 1.07 x 10^5 A/cm^2 at 4.2 K and 10 T is obtained for the coronene-added wire. The J_e has already reached to 1.12 x 10^4 A/cm^2 at 4.2 K and 10 T. The coronene-added wires and SMI+D wires show similar high J_c and J_e values. These J_c and J_e are all higher than those of SiC–added wires. SiC is the most popular additive for MgB_2 wires to date. However, the J_c of SiC-added wires is about 3.3 x 10^4 A/cm^2 at 4.2 K and 10 T in this experiment, which is a little lower than those obtained in our previous results [7-12]. Furthermore, the undoped wires show the J_c of 4 x 10^3 A/cm^2 at 4.2 K and 10 T, which is also the similar level as our previous results [7-12]. The low J_c values for undoped and SiC-added wires suggest that the high J_c and J_e obtained in this experiment is mostly due to the coronene addition. The optimization of fabrication parameters such as the amount of additive and the heat treatment condition is expected to further improve critical current properties.

This chapter is my recent work, I haven't measure the J_c and J_e at 20 K. The J_c and J_e at 20 K should be interesting due to the similar high J_c and J_e as SMI B powder at 4.2 K. It is not easy to predict J_c and J_e values at 20 K because it is sensitive to the amount of carbon substitution for B. However, the coronene addition can control amount of carbon substitution for B which is useful to obtain high J_c in both high and low fields. Furthermore, because the B powder I used in this chapter is larger than that of SMI B powder, the J_c and J_e are expected to be further enhanced by optimization of B powder size and addition of coronene.

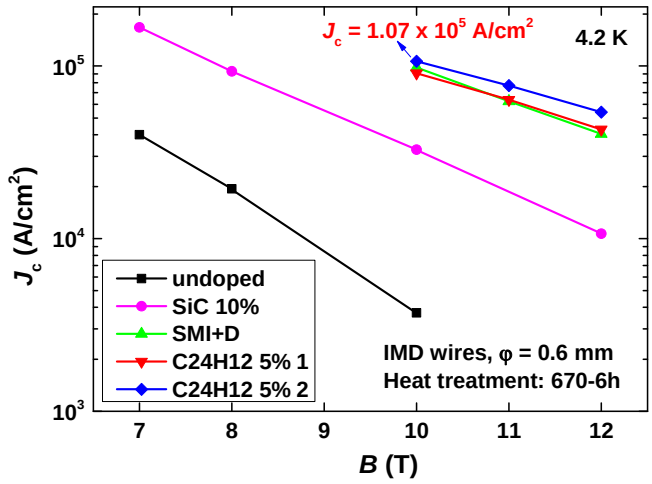

(a)

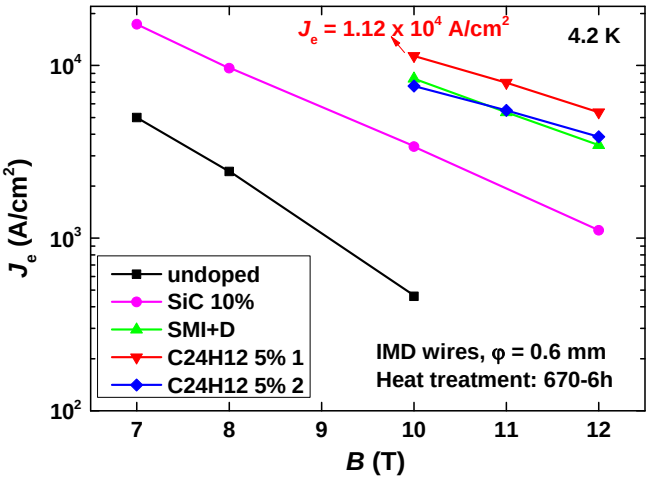

(b)

Fig. 6-7 (a) J_c-B curves, and (b) J_e-B curves of IMD-processed MgB_2 wires

Fig. 6-8 shows the J_c values at high magnetic fields of undoped and coronene-added MgB_2 wires fabricated with both IMD and PIT processes. The J_c-B curve is still linear for all samples even at a high magnetic field of 18T. So I roughly estimated the B_{irr} by extrapolating the J_c-B curves to higher fields. In this study B_{irr} is determined with a criterion of (supercurrent) J = 100 A/cm^2 in the J_c

measurement. The B_{irr} of coronene-added IMD-processed MgB_2 wires has reached to 25.6 T, which is higher than the reported values for MgB_2 wires and tapes. The B_{irr} of PIT wire reached to 22.5 T, which is similar to the 60 mol% SiC-added PIT-processed MgB_2 tapes [14], but the coronene I used in this experiment is only 5 mol%. This indicates that coronene addition is more effective in carbon substitution for B than SiC addition.

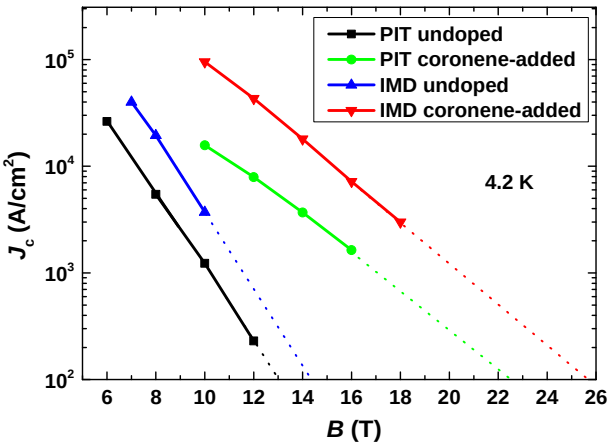

Fig. 6-8 The J_c values at high magnetic fields of undoped and coronene-added MgB_2 wires fabricated with both IMD and PIT processes

6.4 Conclusions

In this chapter, I added an aromatic hydrocarbon - coronene ($C_{24}H_{12}$) to MgB_2 wires fabricated by both IMD and PIT process. The J_c of 1.8 x 10^4 A/cm^2 and J_e of 4.9 x 10^3 A/cm^2 at 4.2 K and 10 T are obtained for 10 mol% coronene-added PIT-processed MgB_2 wires. Furthermore, a high J_c of 1.07 x 10^5 A/cm^2 and a high J_e of 1.12 x 10^4 A/cm^2 at 4.2 K and 10 T are obtained for coronene-added IMD-processed MgB_2 wires. The extrapolated B_{irr} of coronene-added IMD-processed MgB_2 wires reached to 25.6 T at 4.2 K. These obtained values (J_c, J_e, and B_{irr}) are competent to the highest values reported for MgB_2 wires so far. The J_c and J_e at 20 K due to the machine time of magnet and insufficiency of helium. Because the B powder I used in this chapter is larger than that of SMI B powder, the J_c and J_e are expected to be further enhanced (higher than SMI or achieve to target set in chapter 1) by optimization of B powder size and addition of coronene. The coronene addition seems promising to fabricate high performance MgB_2 wires with low cost for large-scale practical applications.

References

[1] Li G Z, Sumption M D, Susner M A, Yang Y, Reddy K M, Rindfleisch M A, Tomsic M J, Thong C J and Collings E W 2012 *Supercond. Sci. Technol.* 25 115023

[2] Ye S J, Matsumoto A, Togano K, Zhang Y, Kumakura H, Song M, Teranishi R and Kiyoshi T 2012 *prestention of ASC2012* 1MB-01

[3] Ye S J, Song M, Matsumoto A, Togano K, Takeguchi M, Ohmura T and Kumakura H 2013 *Supercond. Sci. Technol*. 26 125003

[4] Susner M A, Yang Y, Sumption M D, Collings E W, Rindfleisch M A, Tomsic M J and Marzik J V 2011 *Supercond. Sci. Technol.* 24 012001

[5] Talyzin A V, Luzan S M, Leifer K, Akhtar S, Fetzer J, Cataldo F, Tsybin Y O, Tai C W, Dzwilewski A and Moons E 2011 *J. Phys. Chem. C* 115 13207

[6] Ye S et al, preparation for submission

[7] Hur J, Togano K, Matsumoto A, Kumakura H, Wada H and Kimura K 2008 *Supercond. Sci. Technol.* 21 032001

[8] Togano K, Hur J, Matsumoto A and Kumakura H 2009 *Supercond. Sci. Technol.* 22 015003

[9] Togano K, Hur J, Matsumoto A and Kumakura H 2010 *Supercond. Sci. Technol.* 23 085002

[10] Kumakura H, Hur J, Togano K, Matsumoto A, Wada H and Kimura K 2011 *IEEE Transactions on Applied Superconductivity* 21 2463

[11] Ye S J, Matsumoto A, Togano K and Kumakura H 2011 *Physica C* 471 1133

[12] Ye S J, Song M, Matsumoto A, Togano K, Takeguchi M, Kumakura H, Teranishi R and Kiyoshi T 2013 *Physica C* 484 167

[13] Wilke R H, Budko S L, Canfield P C and Finnemore D K 2004 *PHYSICAL REVIEW LETTERS* 92 217003

[14] Matsumoto A, Togano K, Takeguchi M, Kumakura H 2008 *Supercond. Sci. Technol.* 21 065007

Chapter 7 Summary and prospects

In this chapter, the whole thesis is summarized first, and then some topics I have done and some ongoing works are introduced, finally, prospects for the future of the IMD-processed MgB_2 wires is given.

7.1 Summary

As I introduced in the chapter 1, MgB_2 had attracted much attention for both physicist and material scientists in the first several years since its superconductivity was discovered. It is expected to be used under no-helium conditions to replace metallic superconductors that are operating in a liquid helium environment. Some companies (Hype tech in USA, Columbus in Italy, and Hitachi in Japan) have produced MgB_2 wires for sale. But the present MgB_2 can only be used in the low temperatures (4.2-20 K, obtained by liquid helium or cryocoolers), due to its low critical current properties. The application using MgB_2 for such as MRI, SMEMS, and liquid surface sensor are studied in many labs all over the world.

As we know, the J_c obtained by MgB_2 film is much higher than that of the MgB_2 wire, therefore the J_c could be increased if the MgB_2 wire achieves the similar microstructure to the film. Furthermore, our group developed so-called IMD process, and obtain much higher J_c of MgB_2 wires than that of PIT wires. However, J_c is still not so high as practical level, and J_e is low either. Consequently, my work focused on enhancement of both J_e and J_c.

The un-reacted B particles are observed in the MgB_2 layer of IMD-processed MgB_2 wires. The un-reacted B particles in MgB_2 layer are considered to be caused by the long Mg diffusion distances in IMD process. In order to decrease these un-reacted B particles, I added some amount of Mg powder in the B powder layer of IMD-processed MgB_2 wires. Consequently I developed a new method for fabricating MgB_2 wires combining IMD and PIT processes. These works were described in chapter 2. I found that Mg powder addition is effective to decrease the un-reacted B particles and to enhance the J_c values. But simultaneously Mg powder addition formed some voids in MgB_2 layer and these voids decreased the J_c values. After optimizing the decrease of un-reacted B particles and the decrease of voids, the high J_c and J_e of MgB_2 wires were obtained.

With increasing Mg powder into the B layer of IMD-processed MgB_2 wire, the Mg rod in the center of the wire should be decreased to make the balance between Mg and B. This is a new method which combined IMD and PIT processes. By this new method, the hole in the center of

IMD-processed MgB_2 wires can be decreased, simultaneously, the thickness of MgB_2 layer can be increased. Both decrease of hole and increase of MgB_2 layer thickness cause the increase of MgB_2 area fraction, thus increase the J_e of IMD-processed MgB_2 wires. In our experiments, the maximum J_c of 4.9 x 10^4 A/cm^2 at 10 T and 4.2 K was obtained for M1 (6 mol% Mg addition), while the maximum J_e of 5.8 x 10^3 A/cm^2 was obtained for M2 (17 mol% Mg addition). For the nano-sized B particles, the Mg powder addition could also be used to decrease the B-rich region as observed by Li *et al* [1, 2]. So this new method, which combined IMD and PIT processes for MgB_2 wires, can enhance J_e in spite of B powder size.

The multi-filamentary superconducting wires are important for practical applications. In chapter 3, we succeeded in fabricating IMD-processed 37-filamentary MgB_2 wires. SiC-added 37-filamentary MgB_2 wires show higher J_c value (7.6 x 10^4 A/cm^2 at 4.2 K and 10 T) than the mono-filament and 7 filament wires fabricated under the same conditions. The short Mg diffusion distance of 37-filamentary IMD-processed MgB_2 wires decreases un-reacted B particles. This is the main factor giving rise to the high J_c values. The successful fabrication of 37-filamentay wire indicates that the IMD process can be used to fabricate MgB_2 wires for large-scale applications.

It was reported that the co-addition of SiC and ethyltoluene is effective in the PIT-processed MgB_2 wires. Accordingly, it may be also effective in the IMD-processed MgB_2 wires. In chapter 4, I used ethyltoluene and some other liquid aromatic hydrocarbons (such as toluene, and dimethylbenzene) which have similar structures to the ethyltoluene. The J_c properties are enhanced by the toluene and dimethylbenzene, but ethyltoluene is not so effective. This suggests that there are some differences between IMD and PIT process. The J_e of IMD-processed MgB_2 wire was also highly enhanced. And I first reported that IMD-wires can achieve higher J_e than that of PIT-wires fabricated with the same situation. I studied the mechanism of J_c enhancement from the microstructure. I observed the wires with SiC and/or toluene additives. I found that the SiC and toluene co-addition increases the carbon substitution for B in the MgB_2, and I also found that toluene addition make the grain size small. Furthermore, (a) the liquid hydrocarbon make the mixture the SiC and B powder uniform, (b) the adsorbed liquid aromatic hydrocarbon on the B surface prevents B from adsorbing oxide , and (c) the absorbed liquid aromatic hydrocarbon on the B surface also prevents the growth of MgB_2 grain, are all considered to contribute to the J_c and J_e enhancements. In addition, TEM observation indicates that oxide is distributed in the MgB_2 layer of SiC-added wire, which is an important discovery for the mechanism of SiC addition.

When I was doing the work mentioned above, the researchers in Ohio state university and hyper tech company used a special plasma-synthesized 2% carbon-coated B powder (Special Materials Inc., SMI powder) to fabricate thin IMD-processed MgB_2 wires (diameter: 0.55 mm). And they obtained a high J_c of 1.07 x 10^5 A/cm^2 and a high engineering critical current density (J_e) of 1.67 x 10^4 A/cm^2 at 4.2 K and 10 T for different samples [1]. The small diameter of the wire is considered to decrease the Mg diffusion distance, which leads to an improved reaction between Mg and B,

thus a high J_c is obtained. I also tried this B powder, however, I found I can't obtain good results as theirs. I investigated the B powder, and I found that many BCl_3 (source material for this B powder) exists in the B powder. Because dimethylbenzene dissolve BCl_3 and our experiments in chapter 2 also showed dimethylbenzene enhanced the J_c of IMD-processed MgB_2 wires, I pre-treated SMI B powder using dimethylbenzene. I found the dimethylbenzene decreased the BCl_3 in B powder and then I obtained higher J_c values than those of Ohio state university. For both Ta- and Fe-sheathed wires, the highest J_c value was about 1.2 x 10^5 A/cm^2 at 4.2 K and 10 T, and the J_e value was about 1 x 10^4 A/cm^2. Furthermore, the Fe-SMI+D-1 wire exhibited a J_c of 7.6 x 10^5 A/cm^2 and a J_e of 5.3 x 10^3 A/cm^2 at 20 K and 5 T, which are the highest values reported for MgB_2 wires to date. At 10 K, the J_c value for the wires fabricated in the present study was actually higher than that for commercial Nb-Ti wires in 4.2 K for the magnetic fields at which the measurements were carried out. The researchers in Ohio state university recently reported a higher J_c value [2], but their J_c was calculated excluding the B-rich region where MgB_2 exists. Our J_c value is the real J_c of MgB_2 layer and still the highest record in the world. The detailed microstructures are also observed. These work mentioned above are introduced in chapter 5.

The carbon-coated nano-sized B powder is responsible for the high J_c and J_e of IMD-processed MgB_2 wires. However, the C-coating process of SMI B powder using plasma method is not easily carried out, thus the powder is expensive. And this B powder is unstable because BCl_3 exists. Therefore I tried a new B powder and used aromatic hydrocarbon coronene ($C_{24}H_{12}$) as the carbon source in chapter 6. Similar high J_c and J_e values to carbon-coated B powders in chapter 5 were obtained. The J_c properties are expected to be further enhanced by optimizing the amount of addition and heat treatment conditions.

In a conclusion, there are mainly two parts of work in my Ph.D thesis. First is fabrication process of MgB_2 wires. Second is impurity addition. These two parts can be also divided to three stages by B powder.

First stage is chapters 2-4, which are based on the low quality B powder (325-mesh, 99%). I mainly focused on (1) search for new addition, (2) decrease of the un-reacted B by Mg addition, (3) decrease of the hole in the center, (4) increase of the MgB_2 area fraction, (5) development of a new method combining IMD and PIT, and (6) fabrication of 37-filamentary IMD wires.

Second stage is chapter 5, which is based on carbon-coated nano-sized B (SMI B) powder. Carbon-coated nano-sized B powder is good for enhancement of critical current properties, but it is difficult to control the amount of carbon, unstable (BCl_3 exists), and expensive. I used the dimethylbenzene to decrease BCl_3 in B powders and successfully obtained the highest J_c and J_e values.

Third stage is chapter 6, which is based on a new B powder, but without carbon-coating. I coated the B powder with a new hydrocarbon ($C_{12}H_{24}$). A high performance similar to that obtained by

dimethylbenzene-pretreated SMI B powder in chapter 5 was achieved. This work is still ongoing work. The work in this chapter is expected to be applied to fabricate the large-scale MgB_2 with low cost for practical applications.

I think the works performed in my PHD thesis have contained some new results for MgB_2 wires, but there are still many unfinished works which should be further studied. Below I want to introduce some ongoing work (7.2), and then give a prospect for MgB_2 wires (7.3).

7.2 Some ongoing topics

The following works are mainly carried out by my colleagues. Some are partly finished (7.2.1) and some are un-finished (7.2.2 and 7.2.3). I introduce them here because these works are related to the work of my PHD thesis. Furthermore, these works are important for the development of the high performance MgB_2 wires for practical applications, and need to be continued.

7.2.1 The comparison of mechanical properties for IMD- and PIT-processed MgB_2 wires

In this work, mechanical properties in magnetic fields of MgB_2 mono-core wires fabricated with both IMD and PIT processes were investigated. Both IMD and PIT wires are fabricated with 10 mol% SiC-added 325-mesh B powder by using the method introduced in chapter 4. The detail of the work is published [3]. Here I just give a simple introduction:

Fig. 7-1 shows the apparatus used to measure I_c under uniaxial tension. A 40 mm long sample was prepared. Both ends (10 mm each) were soldered to current terminals of the test apparatus. A pair of voltage taps with 10 mm separation were soldered on the specimen. The stress value was deduced from the tensile load, which was measured by a load cell, and divided by the whole cross-sectional area of the sample. The strain value was deduced from the displacement, which was measured by a clip-on gauge, and divided by the initial length of the specimen.

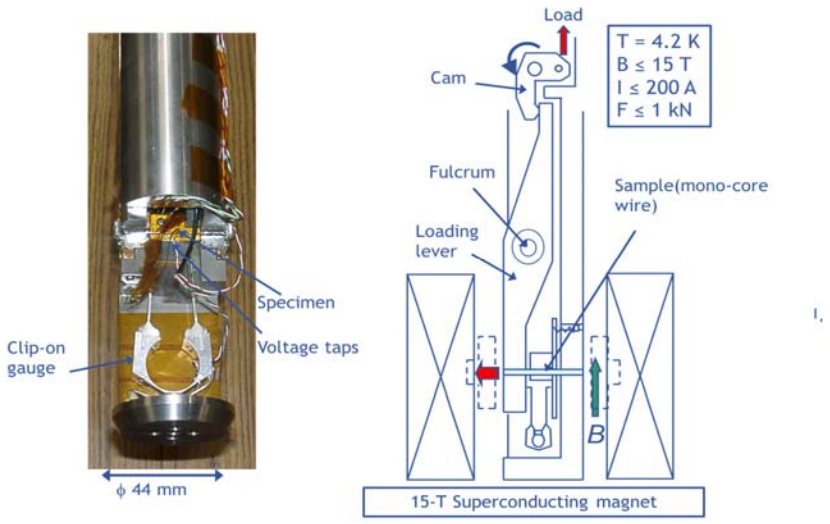

Fig. 7-1 Photograph (left) and schematic illustration (right) of apparatus to measure I_c versus uniaxial tension

Fig. 7-2 shows the tensile strain (ε) dependence of I_c for IMD-MgB_2 and PIT-MgB_2 wires at 10 T, 4.2 K. Solid markers indicate I_c measured at fixed strain. Open markers indicate I_c measured at zero stress which is to check the reversibility of I_c. The strain did not go back to zero when the stress was released to zero because of the plastic deformation of the wire. The obtained I_c–ε relations of both wires are similar in shape. I_c increased linearly and reversibly with increasing tensile strain up to the reversible limit (irreversible strain, ε_{irr}), at which the maximum I_c value was observed. I_c deteriorated irreversibly at $\varepsilon > \varepsilon_{irr}$. The irreversible strain ε_{irr} values were 0.67% and 0.54 % for IMD and PIT wires, respectively. The inset of Fig. 7-2 shows the reversible region ($\varepsilon < \varepsilon_{irr}$) of I_c–ε normalized by I_{c0} (I_c at zero strain). Each (I_c/I_{c0}) – ε plot can be fitted with a linear function. The slope values of each function correspond to the strain sensitivity. The deduced strain sensitivity values are 0.14 and 0.21 for IMD and PIT wires, respectively.

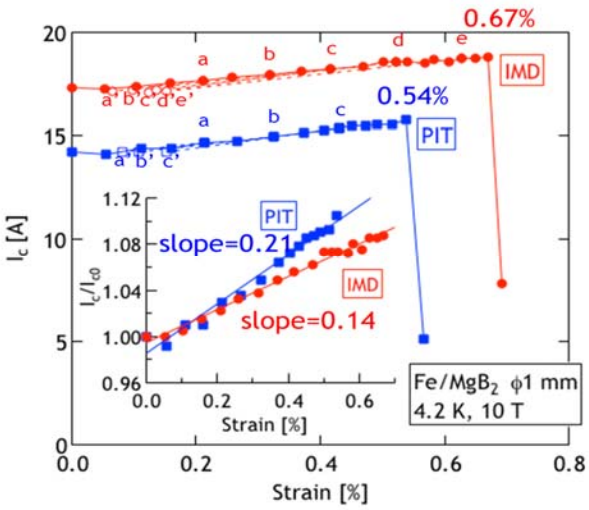

	ε_{irr}	$d(I_c/I_{c0})/d\varepsilon$
IMD	0.67%	0.143
PIT	0.54%	0.213

Fig. 7-2 I_c as a function of uniaxial strain, inset shows I_c/I_{c0} as a function of uniaxial strain (both IMD and PIT are fabricated with 325-mesh B with 10 mol% SiC addition as the method introduced in chapter 4)

Fig. 7-3 shows the apparatus used to measure I_c under transverse compression. Both ends (10 mm each) of the 40 mm long sample were soldered to current terminals of the test apparatus. A pair of voltage taps with 10 mm separation was soldered. The width of the pressure block, which is made of GFRP (glass-fiber-reinforced plastics), is 3 mm. The compressive stress was calculated using the pressure block width and the cross-sectional area of the wire.

Fig. 7-4 shows transverse compressive stress (σ_t) dependence of normalized I_c ((I_c/I_{c0})– σ_t) for IMD and PIT wires at 10 T, 4.2 K. Solid and open markers indicate I_c at fixed (loaded) strain and at stress-released condition, respectively. I_c remained the initial value and was reversible up to a

certain threshold stress. I_c deterioration of IMD-MgB_2 wire started at the transverse compressive stress of 206 MPa, whereas PIT-MgB_2 wire I_c at 160 MPa.

This experiment was carried out only at 4.2 K. IMD-processed MgB_2 wires showed better mechanical properties in magnetic fields than those of PIT-processed MgB_2 wires. The other temperatures (10-20 K), sheath materials, and the number of filaments should be considered in the future work.

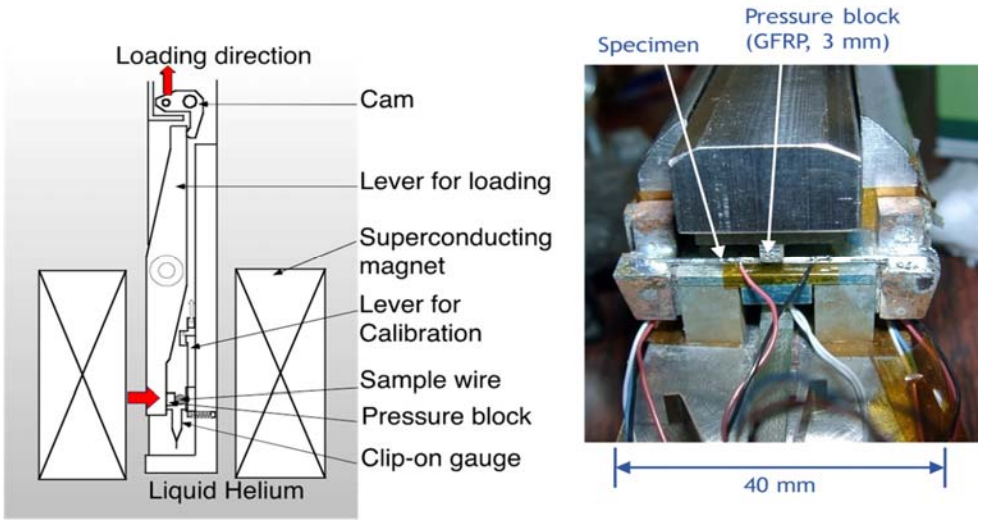

Fig. 7-3 Schematic illustration (left) and photo (right) of apparatus to measure I_c versus transverse compression

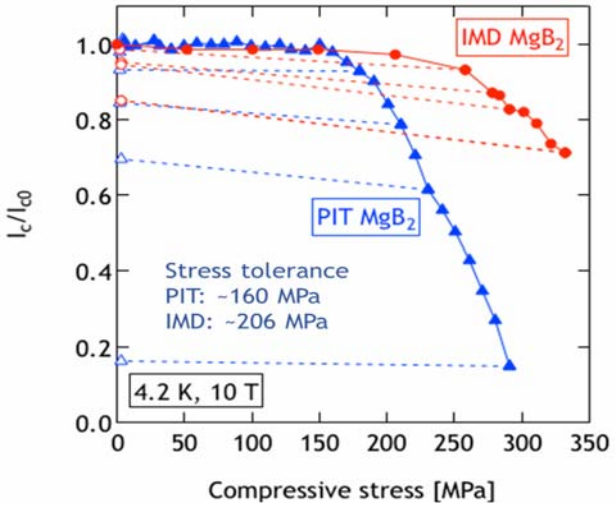

Fig. 7-4 Normalized I_c as a function of transverse compressive stress (both IMD and PIT are fabricated with 325-mesh B with 10 mol% SiC addition as the method introduced in chapter 4)

7.2.2 Strain measurement of IMD-processed MgB_2 wires by synchrotron radiation at SPring-8

The superconductive properties are affected by external strain. J_c under a stress of superconducting wire was investigated in 7.2.1. When a distortion is added to a superconducting wire, the strain condition is different depending on the internal structure and the manufacturing method of wire. Therefore, it is necessary to observe directly the distortion of internal superconductor in the superconducting wire. A lattice strain measurements of MgB_2 wire were performed by diffraction method at the BL22XU of SPring-8 with the approval of the Japan Synchrotron Radiation Research Institute (JASRI) (Proposal No. 2013B1573 and 2012B1435). The BL28B2 diffractometer and the experimental layout are shown in Fig. 7-5 (a) and (b), respectively. The relations between a load strain and the lattice strain of a measured *ex situ* PIT-processed MgB_2 wires are shown in Fig. 7-6. The MgB_2 crystal showed elastic distortion behavior for the loading force. We haven't finished the measurement of IMD-processed MgB_2 wires due to the short machine time, and we will apply the next machine time to do it.

(a) 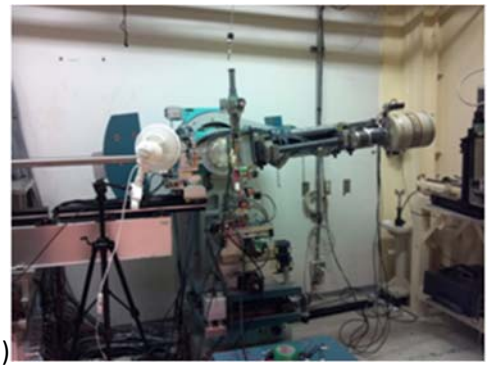 (b)

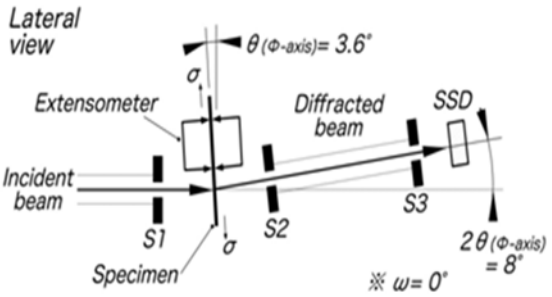

Fig. 7-5 (a) The diffractometer and (b) experiment layout

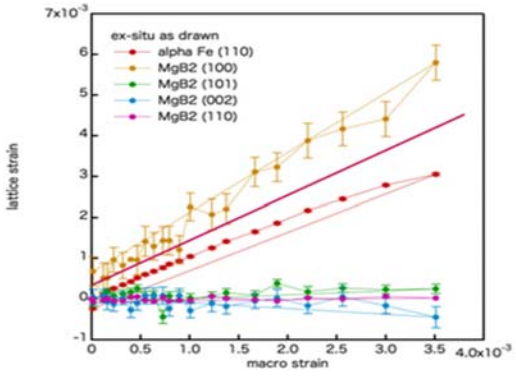

Fig. 7-6 The relations of a load strain and the lattice strain

7.2.3 Reaction observation of IMD-processed MgB_2 wires during the heat treatment by XRD in Spring-8

In this research, we used the strong XRD to observe the reaction process of IMD-processed MgB_2 wires during the heat treatment. We measured the XRD pattern twice per second. The experiment is carried out with the station 3 of beam BL22XU in the spring-8 (Under the shared use program of Japan Atomic Energy Agency Facility (JAEA Proposal No. 2013A-E22 and 2013B-E20, JASRI Proposal No. 2013A3789 and 2013B3782)). Fig. 7-7 shows (a) the experimental equipment, (b) magnified image, and (c) wire furnace. The sample was sealed in a silica tube filled with Ar gas, which is similar to the real heat treatment process. The photon energy of XRD is 30 keV, and the beam size is 0.5 x 0.2 mm. The detecting image is a 2-D diffraction pattern, as shown in Fig. 7-8(a). The calculated 1-D diffraction pattern data are shown in Fig. 7-8 (b). MgB_2 can be found in the heat treatment process from the obtained data, while there is only Mg peak for no heat treatment sample. This experiment gives the direct information of the MgB_2 formation reaction during the heat treatment. We can expect to enhance the critical current properties by controlling the microstructure of MgB_2 based on the information. The experiment is not yet completed due to limited machine time. We will continue the measurement when we have enough machine time.

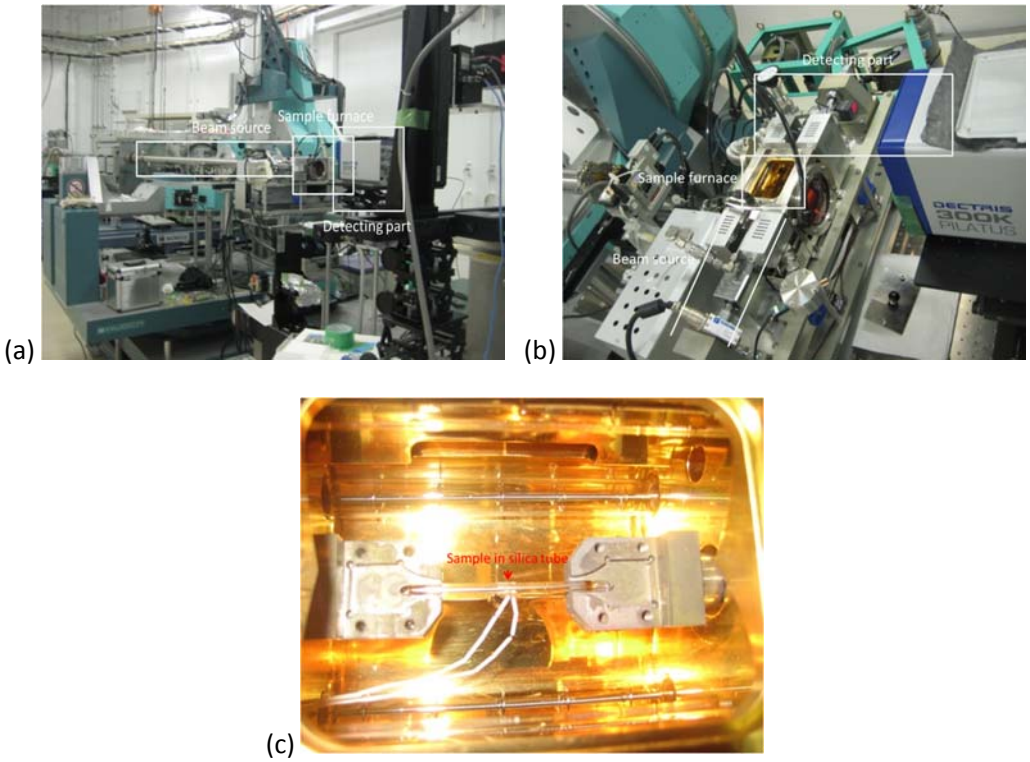

Fig. 7-7 (a) Experimental equipment, (b) magnified image, and (c) wire furnace

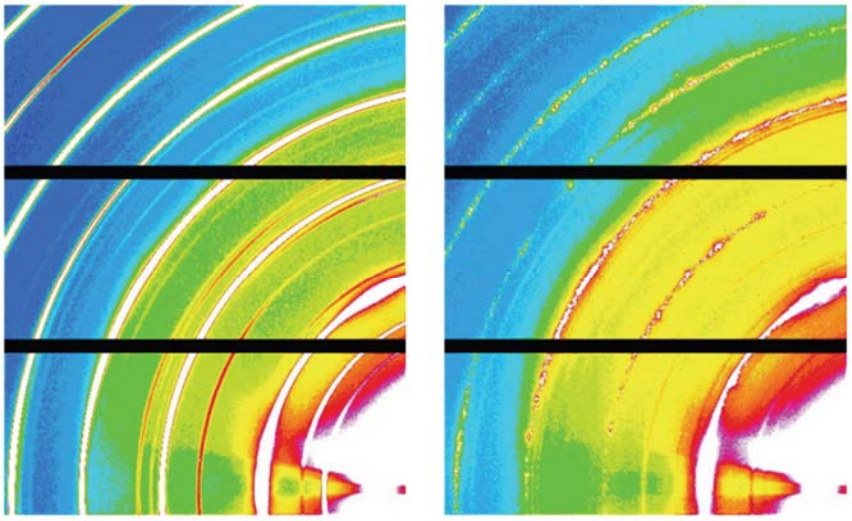

(a)

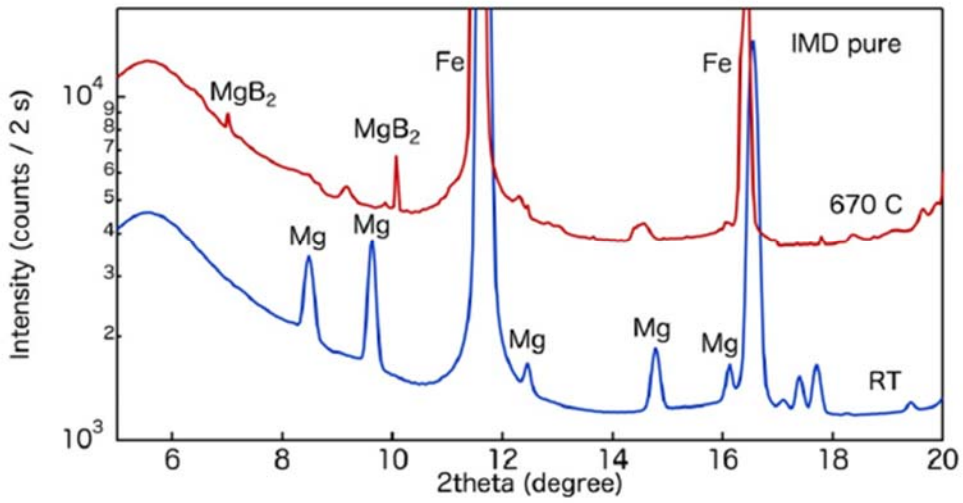

(b)

Fig. 7-8 (a) 2-D data of XRD diffraction, and (b) 1-D data of XRD calculated from (a)

7.3 Prospects

As introduced in Chapter 1, “low cost” is the most important advantage of MgB_2 superconducting wires. PIT-processed MgB_2 wires have been applied to the prototype of MRI. However, both the product cost and the operating cost are still high, which is mainly because the low critical current properties need the high operation conditions (low temperature and/or low field). IMD-processed MgB_2 wires have showed much better critical current properties than PIT-processed wires as introduced in this thesis. We also found that IMD-processed MgB_2 wires have better mechanical properties. However, the critical current properties of IMD MgB_2 wires are still below the practical level. In order to develop high performance IMD-processed MgB_2 wires feasible for large-scale applications, the first task is the enhancement of critical current properties (especially the critical current properties at 20 K and 5 T). Meanwhile, some other properties (such as mechanical properties, AC loss) of the IMD-processed MgB_2 wires should also be considered.

I consider that the future research of IMD-processed MgB_2 wires should focus on the following topics:

1. B and impurity addition

(a) B powder: B powder is crucial for the critical current properties of IMD-processed MgB_2 wires. The main reason for the high J_c in 7- and 19- filamentary wires obtained by our group should be attributed to the high quality B powder. The high J_c and J_e values recently obtained by both Ohio state university [1, 2] and our group are also attributed to the carbon-coated high quality nano-sized B powders (chapter 5). The high J_c properties of both IMD- and PIT-processed MgB_2 wires obtained in chapter 6 are mainly due to the $C_{24}H_{12}$ addition, but it should also be attributed to the high quality B powder. To date, we haven’t understood what kind of B powder is useful for the high J_c properties of MgB_2. Investigation of the influence of B powder on J_c properties is a difficult but very important work.

(b) Carbon-containing impurity addition: carbon-containing impurity addition is widely used for MgB_2 wires. Carbon substitution for B enhances J_c only in high magnetic fields. But J_c in low field decreases because carbon decreases the connectivity of MgB_2 grains. The control of carbon substitution for B to increase J_c in high magnetic fields with less decrease of J_c in low fields needs to be studied.

(c) No carbon addition: there are thousands of reports on impurity additives but no one have good reproducibility except for carbon source addition. However, this doesn’t mean that there is no effective source other than carbon.

2. Study of Mg diffusion mechanism in IMD process

To date, there are no reports on the diffusion mechanism of Mg in IMD-processed MgB_2 wires because the diffusion mechanism is not easy to investigate. The following parameters affecting the Mg diffusion should be considered:

(a) The Mg rod diameter, B layer thickness, B packing density, and the sheath materials.

(b) The B powder quality and B powder size.

(c) Heat treatment conditions (temperature and time).

The understanding of the diffusion mechanism is useful to improve the reaction between Mg and B, to control the microstructure (grain size, and texture) of MgB_2, and to increase the MgB_2 area fraction in the wire.

3. Properties important for large-scale applications

The purpose of MgB_2 wire development is practical applications with low cost. The first task is the enhancement of the critical current properties without the increase of fabrication cost, meanwhile, other properties should also be considered.

(a) Sheath materials: no reaction with Mg and B, good thermal and electric conductivity, easy for the wire fabrication, low cost…

(b) Electrical properties such as AC loss

(c) Mechanical properties: strain and stress effects were measured only at 4.2 K for mono-filamentary wire in 7.2.1. Other temperatures (10-20 K), sheath materials, and the number of filament should be considered.

Sometimes luck is more important than sense, which is just like that superconductivity of MgB_2 was discovered in 2001 [4], 47 years later since its preparation was first reported [5].

References

[1] Li G Z, Sumption M D, Susner M A, Yang Y, Reddy K M, Rindfleisch M A, Tomsic M J, Thong C J and Collings E W 2012 *Supercond. Sci. Technol.* 25 115023
[2] Li G Z, Sumption M D, Zwayer J B, Susner M A, Rindfleisch M A, Thong C J, Tomsic M J and Collings E W 2013 *Supercond. Sci. Technol*. 26 095007
[3] Nishijima G, Ye S J, Matsumoto A, Togano K, Kumakura H, Kitaguchi H and Oguro H 2012 *Supercond. Sci. Technol.* 25 054012
[4] Nagamatsu J, Nakagawa N, Muranaka T, Zenitani Y and Akimitsu J 2001 *Nature* 410 63
[5] Jones M E and Marsh R E 1954 *Journal of the American Chemical Society* 76 1434

Publications

Scientific papers

[1] Ye S J, Matsumoto A, Togano K and Kumakura H 2011 Physica C 471 1133
Enhancement of the critical current density of internal Mg diffusion processed MgB_2 wires by the addition of both SiC and liquid aromatic hydrocarbon

[2] Ye S J, Song M, Matsumoto A, Togano K, Zhang Y, Kumakura H, Takeguchi M, Teranishi R and Kiyoshi T 2012 Supercond. Sci. Technol. 25 125014
Enhancing the critical current properties of internal Mg diffusion-processed MgB_2 wires by Mg addition

[3] Ye S J, Song M, Matsumoto A, Togano K, Takeguchi M, Kumakura H, Teranishi R and Kiyoshi T 2013 Physica C 484 167
Comparison of SiC and/or toluene additives to the critical current density of internal Mg diffusion-processed MgB_2 wires

[4] Nishijima G, Ye S J, Matsumoto A, Togano K, Kumakura H, Kitaguchi H and Oguro H 2012 Supercond. Sci. Technol. 25 054012
Mechanical properties of MgB_2 superconducting wires fabricated by internal Mg diffusion process

[5] Ye S J, Matsumoto A, Togano K, Ohmura T and Kumakura H 2013 Supercond. Sci. Technol. 26 105027
The critical current properties of 37-filament internal Mg diffusion-processed MgB_2 wires

[6] Ye S J, Song M, Matsumoto A, Togano K, Takeguchi M, Ohmura T and Kumakura H 2013 Supercond. Sci. Technol. 26 125003
High-performance MgB_2 superconducting wires for use under liquid-helium-free conditions fabricated using an internal Mg diffusion process

[7] Ye S J, Matsumoto A, Zhang Y, Togano K, Ohmura T and Kumakura H 2014 Supercond. Sci. Technol. *Submitted*
New method for MgB_2 wire fabrication combining internal-Mg-diffusion and powder-in-tube processes

[8] Ye S J *et al*. The content is basing on Chapter 6, *preparation*.

Presentations

(1) 葉 術軍、松本 明善、戸叶 一正、熊倉 浩明、「拡散法 MgB_2 線材における不純物添加効果」、2011 年度春季低温工学・超電導学会、 2011/05/18-2011/05/20、つくば、日本、講演番号： 2P-p20. (**Poster**)

(2) Ye S J, Song M, Matsumoto A, Togano K, Takeguchi M, Kumakura H, Teranishi R, Kiyoshi T, "Comparison of SiC and/or toluene additives to the critical current density of internal Mg diffusion-processed MgB_2 wires", the 24rd International Symposium on Superconductivity (ISS2011), 2011/10/24-2011/10/26, Tokyo, Japan, Program number： WTP-42. (**Poster**)

(3) 葉 術軍、松本 明善、戸叶 一正、熊倉 浩明、寺西 亮、木吉 司、「内部拡散法（IMD）による 19、37 芯 MgB_2 線材の作製」、2011 年度秋季低温工学・超電導学会、2011/11/09-2011/11/11、金沢、日本、講演番号： 2P-p17. (**Poster**)

(4) Ye S J, Matsumoto A, Togano K, Kumakura H, Teranishi R, Kiyoshi T, "The enhancement of critical current properties of internal Mg diffusion (IMD) processed MgB_2 wires by decreasing the un-reacted B", ICEC 24 - ICMC 2012, 2012/5/14-2012/5/18, Fukuoka, Japan, Program number: 15P-P09-08. (**Poster**)

(5) Ye S J, Matsumoto A, Togano K, Zhang Y, Kumakura H, Song M, Teranishi R, Kiyoshi T, "Critical current properties and microstructure of internal Mg diffusion (IMD)-processed 37-filamentary MgB_2 wires", IUMRS-ICEM 2012, 2012/9/23-2012/9/28, Yokohama, Japan, Program number: B-4-O25-012. (**Oral**)

(6) Ye S J, Matsumoto A, Togano K, Zhang Y, Kumakura H, Song M, Teranishi R, Kiyoshi T, "Enhancement of the critical current properties of Internal Mg diffusion-processed MgB_2 wires by Mg powder addition", 2012 Applied Superconductivity Conference (ASC 2012), 2012/10/07-2012/10/12, Portland, USA, Program number: 1MB-01. (**Invited oral**)

(7) 葉 術軍、松本 明善、戸叶 一正、熊倉 浩明、寺西 亮、木吉 司、「内部 Mg 拡散法 MgB_2 線材における MgB_2 の層厚と臨界電流特性」、2012 年度秋季低温工学・超電導学会、2011/11/09-2011/11/11、岩手、日本、講演番号： 2P-p02. (**Poster**)

(8) Ye S J, Zhang Y, Matsumoto A, Togano K, Kumakura H, Teranishi R, Kiyoshi T, "Enhancement of the critical current properties of MgB_2 wires by triphenylamine ($C_{18}H_{15}N$) addition", the 25rd International Symposium on Superconductivity (ISS2012), 2012/12/3-2012/12/5, Tokyo, Japan, Program number： WTP-62. (**Poster**)

(9) 葉 術軍、松本 明善、張　雲超、戸叶 一正、熊倉 浩明、「内部拡散法による MgB_2 線材の臨界電流特性及び微細組織」、2013 年度春季低温工学・超電導学会、2013/5/13-2013/5/15、東京、日本、講演番号：2C-a02. (**Oral**)

(10) Ye S J, Song M, Matsumoto A, Togano K, Zhang Y, Takeguchi M, Teranishi R, Ohmura T, Kumakura H, “Improvement of critical current properties of internal Mg diffusion (IMD)–processed MgB_2 wires”, European Conference on Applied Superconductivity (EUCAS 2013), 2013/09/05-2013/09/19, Genoa, Italy, Program number：1P-WT1-06. (Poster)

(11) Ye S J, Matsumoto A, Togano K, Ohmura T, Kumakura H, “Enhancement of the critical current properties of MgB_2 wires by triphenylamine ($C_{18}H_{15}N$) addition”, the 26rd International Symposium on Superconductivity (ISS2013), 2013/11/18-2013/11/20, Tokyo, Japan, Program number： WTP-40. (**Poster**)

(12) 葉 術軍、松本 明善、戸叶 一正、大村孝仁、熊倉 浩明、「IMD 法と PIT 法をミックスした方法による高臨界電流密度 MgB_2 線材の作製」、2013 年度秋季低温工学・超電導学会、2013/12/4-2013/12/6、東京、日本、講演番号：2B-a04. (**Oral**)

Patent

(1) 熊倉　浩明、松本　明善、葉 術軍、MgB_2 超伝導体の製造方法および MgB_2 超伝導体、日本特許、出願番号：2013-259711